Embedded Radio Frequency Sensor System into The Transceiver Architecture and Enhanced Communication Capability in Adverse Environment

by

Hossein Saghlatoon

A thesis submitted in partial fulfillment of the requirements for the degree of

Doctor of Philosophy

In

Engineering Management

Department of Mechanical Engineering

University of Alberta

Abstract

Sensors are an essential part of Internet-of-Things (IoT) and wireless-sensor-network. They are the main block for sensing and obtaining information about the environmental parameters or materials of concern. From industrial applications for safety improvement to biomedical, health monitoring and smart homes for quality assessment, the sensors play a significant role. The desired parameter alters the characteristics of a sensor which later is converted to digital data for post-processing and decision making.

Amongst different categories and types of sensor, radio frequency (RF) and microwave ones have recently attracted more attention due to the advantages that can be obtained through the frequency response monitoring. Still, there is a long path from what has been proposed in the literature to commercial versions of RF/Microwave sensors.

Most of the studied RF/Microwave sensors lack from the conversion of the frequency domain sensing data to digital values. For this purpose, either expensive frequency monitoring equipment is required or the data should be post-processed to extract the sensing information. This stays as the main obstacle for the commercialization of low-cost, low-power, and fast response sensors. In addition, since the sensing is done by altering the frequency response of the device, no mechanisms have been proposed to compensate for the effect of the parameter under test on the circuit. To the author's knowledge, not many investigations have been done on the conversion of RF/Microwave sensing data to digital values and compensation of frequency-response deviation due to sensing as well as the integration of RF sensors into the

communication system.

In this dissertation, different configurations of sensor system embedded into the conventional communication architectures have been proposed in which the antenna acts as the main radiating elements and passive RF/Microwave sensor. In the first system, the extraction of sensing data is done at the receiver using a simple, low-cost and low power, zero crossing detector. This system is adaptable to communication nodes where the carrier frequency of the system can be in a certain range and does not have to be fixed. The second system comprises a sensing scheme embedded into a fixed frequency digital modulator in which the parameter under test alters the frequency response of the antenna. The antenna loads the modulator causing the error of the feedback loop in the frequency stabilization section to increase depending on the loading strength. The error is a control voltage forcing the local oscillator to operate at the original frequency and can be converted to digital data using an analog-to-digital converter (ADC) and be sent alongside the pilot data. These systems are implemented based on RFID standards and conventional modulation scheme as an example and are not limited to this application at all. The implementation of the RF/Microwave sensing system into the transceiver architectures in the proposed manner does not require any more power consumption; therefore, the power consumption of the system is preserved. In addition, in certain applications such as on-body or metal-proximity, the communication range of the sensing system diminishes significantly due to their adverse effect on electromagnetic waves. It is required to design a system in order to improve the communication range passively. Another aspect of this dissertation is to mitigate this obstacle for magnetically

coupled communication system.

Preface

This is an original work by Hossein Saghlatoon. Chapter 4 of this thesis is under review (Major revision) as, H. Saghlatoon, R. Mirzavand, and P. Mousavi, "Fixed-Frequency Material Sensing Transmitter," IEEE Transactions on Industrial Electronics, Oct 2018. Chapter 5 is published as, H. Saghlatoon, R. Mirzavand, M. M. Honari, and P. Mousavi, "Sensor Antenna Transmitter System for Material Detection in Wireless-Sensor-Node Applications," IEEE Sensors Journal, Vol. 18, No. 21. pp. 8812–8819, November 2018. Chapter 6 is published as, H. Saghlatoon, R. Mirzavand, M. M. Honari, and P. Mousavi, "Investigation on Passive Booster for Improving Magnetic Coupling of Metal Mounted Proximity Range HF RFIDs," IEEE Transactions on Microwave Theory and Techniques, Vol. 65, No. 9, pp. 3401–3408, September 2017 and H. Saghlatoon, R. Mirzavand, M. M. Honari, and P. Mousavi, "Low-cost inkjet printed passive booster for increasing the magnetic coupling in proximity of metal object for NFC systems," IEEE Microwave and Wireless Component Letters, Vol. 26, No. 12, pp. 996–998, December 2016.

Acknowledgment

List of Symbols

ϵ_r Relative permittivity

ϵ Permittivity (Dielectric constant)

ϵ_0 Free space permittivity

ϵ_{eff} Effective permittivity

λ Wave length

β Feedback transfer function

ϕ Phase response

ω Angular frequency

μ Permeability

$\tan\delta$ Dissipation factor

List of Figures

List of Tables

Contents

Chapter 1

Introduction

1.1　Motivation

Sensors are nowadays used in many applications from monitoring the temperature of a room to biomedical sensors for capturing brain signals. Sensors are differentiated based on their reliability, repeatability, accuracy, response time, and cost. Depending on what characteristic of environment they sense, different methods have been used for the realization of sensors.

Amongst different sensing categories, dielectric spectroscopy is one of the desirable ones due to its application for material characterization. Material characterization is useful for the recognition of unknown specimen, water quality monitoring, structural and concrete thermal damage, pollution and toxic hazards, food expiry detection and etc. It can be done using different techniques but the frequency domain spectroscopy is favorable since it provides us with the characteristics of the material versus frequency and can be done using RF/Microwave circuits.

In frequency domain spectroscopy, the desired material for characterization affects the electromagnetic properties of the circuit including the electric and/or magnetic fields distribution or current distribution. This effect can be seen on any combination of RF characteristics ranging from the input reflection coefficient, transmission loss, phase of the signal

to radiation properties and gain of the system. While Designing an RF/Microwave sensor, the sensing range, repeatability, power consumption, resolution, and calibration should be considered. Sensing range and resolution have a trade-off since by increasing the resolution of the sensor which is its sensitivity, the total sensing range decreases due to the limited bandwidth of the system. Also, for reducing the power consumption of the system, high-resolution systems might become more difficult to obtain since an active system provides a high-quality response. Depending on the application, more restrictions might be imposed limiting the quality and simplicity of the system. Most RF sensors are not practically usable because it is required to have a frequency monitoring device such as a VNA or Spectrum analyzer to observe the frequency shift and then post-processing the results in order to characterize the material. This equipment is bulky, expensive, power consuming, and impractical for ordinary users. Another issue with this type of sensor is that the frequency spectrum has been altered and no mechanism has been proposed to compensate for the effect of the material or parameter under test on the circuit. This results in the operation of the system in a different frequency which might not be tolerable in fixed-frequency applications. It should also be noted that the detection of frequency response alteration can be difficult and a subsystem should be added to facilitate the process. When observing the frequency spectrum of an RF sensor, depending on the resolution, sensitivity, and quality of the device, the frequency shift might be visible for a user; however, autonomously converting this change to a digital number or a method compatible with an automated system can be very difficult and expensive. It is desired to have the RF/Microwave sensing and conversion of the frequency domain signal to a number in a cost-effective and low-energy fashion.

In wireless RF/Microwave sensor nodes, the communication range and powering-up the system can be challenging as well. In applications including the RF/Microwave sensors operating in lossy medium such as implantable sensors for biomedical applications or near-metal systems, it is required to improve the communication range passively. In such applications, a passive booster system can act as a separate passive component which concentrates on the electromagnetic fields toward the sensor node resulting in the improved transferred power

2

and total communication range of the whole system.

1.2 Objectives

The objectives of this work are:

1. Integrating of RF sensing into communication block

2. Developing novel communication enabling sensing in one integrated system with capability to compensate for the frequency shift of the RF sensor antenna in fixed-frequency application.

3. Developing novel transmitter/receiver combined system for RF sensing and detection for frequency hovering applications.

4. Removing the necessity of frequency domain monitoring equipment for the extraction of RF sensing signal.

5. Theoretically analyzing of the relative permittivity effect on the operating frequency of RF modulator

6. Enhancing the communication range and applicability of the proposed system in adverse environment

1.3 Outline

In this dissertation, a new method is proposed for the frequency recovery of an RF/Microwave sensor system in an inexpensive, reliable, fast, low-cost, and practical way. This method can be implemented in the modulator or demodulator depending on the application and embedded into the conventional transceiver architecture without adding more power consuming components.

In the first system, the frequency recovery technique is embedded into the modulator (Modulator-based sensor) whereas in the second proposition the technique is implemented at the receiver side (Demodulator-based sensor). In both systems, the sensing of the parameter is done using a sensor antenna which is directly in contact with the specimen. Therefore, the characteristics of the antenna change for different specimens; this can be seen as a change in the frequency response of the antenna. The sensor antenna is connected to the local oscillator (LO) at the transmitter side, which is a Voltage Controlled Oscillator (VCO). Changes in antenna frequency response alter the operating frequency of LO due to the loading influence of antenna on VCO.

In the modulator based sensor, the recovery of the frequency, which is the same as sensing the parameter, is done at the transmitter side by sampling the carrier frequency with a quarter wavelength coupled line coupler and comparing it to a reference frequency using a Phase/Frequency Comparator (PFC). The output of the PFC is a voltage proportional to the instantaneous phase error of the two signals. Therefore, the error voltage is proportional to the characteristics of the sample under test. This signal can be used to re-tune the system back to the original operational frequency as well as being sent to the base station for monitoring the sensing purposes. The proposed system is discussed in details in Chapter 3.

In the demodulator-based sensor, sensing is done in a similar way as in the modulator-based sensor, but the detection (frequency recovery) is done at the receiver using a zero-crossing detector. The output of the zero-crossing detector is the number of times the signal changes sign between positive and negative values, which is proportional to twice the frequency of the signal in a known time interval. So if this number is divided by twice of the time interval the frequency of the signal is obtained. Since the original carrier frequency is also known by comparing the frequency shift with the reference value, the property of the sample can be detected. This can be done at both proposed systems if other parameters are kept constant and only one parameter (relative permittivity of the sample in this project) can alter.
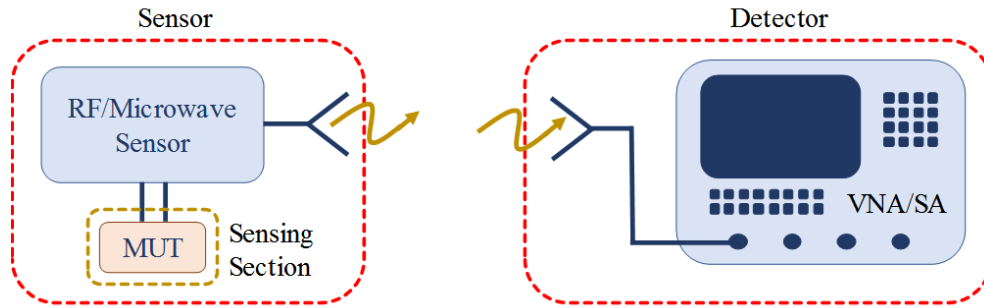
Figure 1.1: The conventional RF/Microwave wireless sensor system

Since the proposed methods are integrated into a conventional communication transmitter where passive sensing was not implemented, they are suitable for wireless sensor network and Radio Frequency Identification (RFID) sensor applications.

A simple dipole antenna for dielectric spectroscopy is used, on which the materials under test (MUTS) are placed on the sensing region. In the modulator-based sensor system, the sensing region is an open loop which loads the antenna parasitically. By changing the relative permittivity of MUTS, the input impedance of the antenna changes and therefore, the resonant frequency of antenna shifts. In the demodulator-based sensor system, the sensor antenna is a dipole but MUTS are placed on the capacitive gap between the radiating arms to gain maximum sensitivity. This system is further studied in Chapter 4.

Fig. 1.1 depicts the block diagram of the conventional wireless RF/Microwave sensor system that requires frequency spectrum monitoring, which is expensive, impractical, and time consuming while Fig. 1.2 and 1.3, on the other hand, present the block diagram of the proposed systems that have the ability of specimen detection as well as data communication.

The proposed systems are compatible with UHF RFID system but for HF version of the RFID system and Near Field Communication (NFC), the communication works based on the magnetic coupling between the receiver and transmitter coils. In industrial applications, it is required to attach the tag to a metal object, such as machinery equipment or tools, which is considered as an adverse medium as shown in Fig. 1.4 (a). The operation of the RFID system
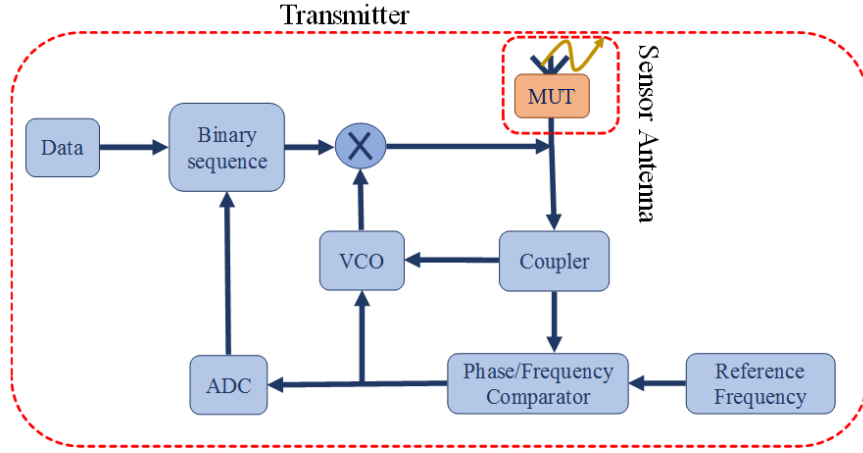
Figure 1.2: The proposed modulator based sensor system.
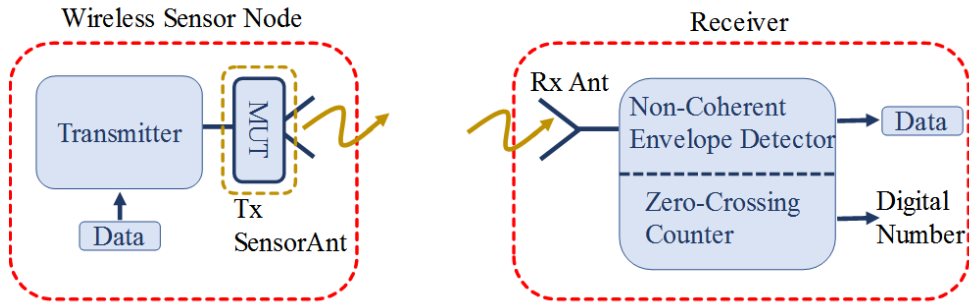
Figure 1.3: The proposed demodulator based sensor system.

in the proximity of the metal objects is very restricted due to the harmful effect of conductors on the propagation of the microwave signals and performance of the circuit. But due to the rapid progression of the Android and smartphone RFID-NFC systems, it is a demand in the industry to read HF RFID tags placed directly on a metallic object using smartphones and tablets. In order to minimize the cost of a tag and reduce the complexity of the installation process, the tags are miniaturized significantly resulting in poor communication when they are placed on metallic objects. In Chapter 5, a passive magnetic power booster is proposed and investigated in order to increase the read range of a tiny footprint class of HF RFID system using a smartphone suitable for sensing as well as communications. The system is based on magnetic field reproduction principle in which the intensity of the magnetic field is
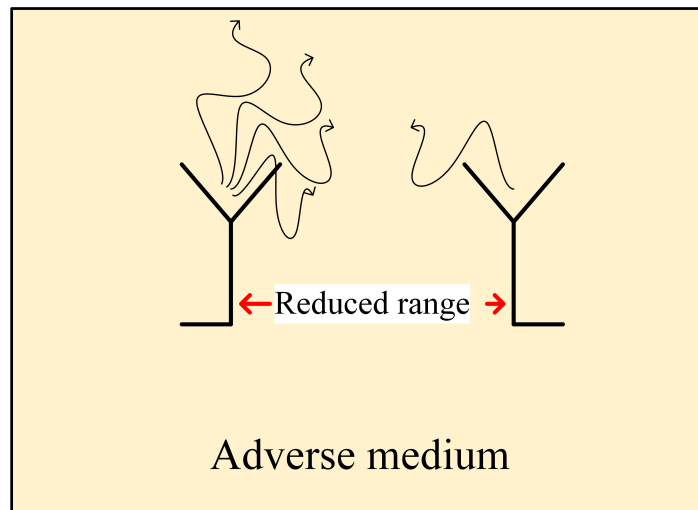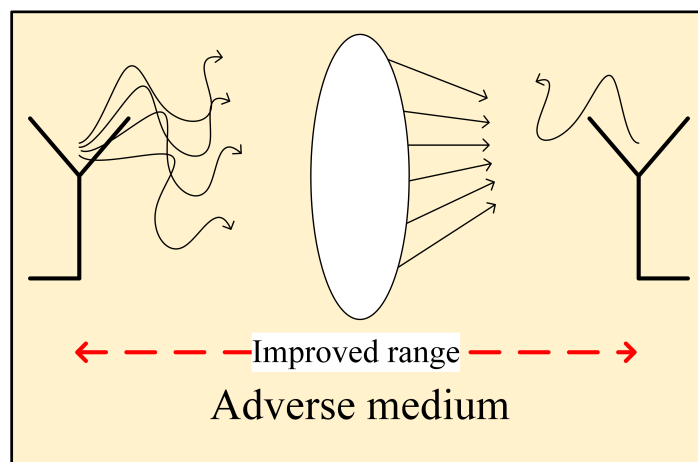
Figure 1.4: The system in adverse medium (a) the reduced range because of the medium and (b) the improved scenario due to the booster.

increased in a small region (proportional to the RFID tag) while the power is provided by the reader (smartphone) in a larger area but with lower intensity, as shown in Fig. 1.4 (b).

Chapter 2

Literature Review

Sensors have been traditionally used in industrial environments for improving safety, stochastic data acquisition, monitoring, and controlling the environment. Nowadays, there is a huge demand for low-cost wireless sensors as a part of Internet-of-Things (IoT) for smart homes, smart cities, cars, and construction as shown in Fig. 2.1 and Fig. 2.2 [1]- [7]. In a wireless sensor node (WSN), the main parts are the sensor section, communication and identification, and power-up. In the current systems available commercially, a battery should be included in the system as the energy reservoir (Fig. 2.3) or there should be a physical electric connection through wiring. This power is required for both sensing and communication. Conventional sensors in the market require a low-frequency circuitry for sensing which requires power for the operation. It can be used in a Wheatstone bridge configuration in which the sensor unbalances the bridge and the output voltage is correlated to parameter under test (PUT). Another configuration is a voltage divider between a fixed component and the sensor with output correlated to PUT. In both of the mentioned systems, there should be an analog to digital converter (ADC) and a microprocessor to convert the voltage to a digital signal and process it. Sensing using RF component in the system does not require any more power consumption since PUT can passively alter the characteristics of the system.

Figure 2.1: How IoT connects different aspects of our lives [8].
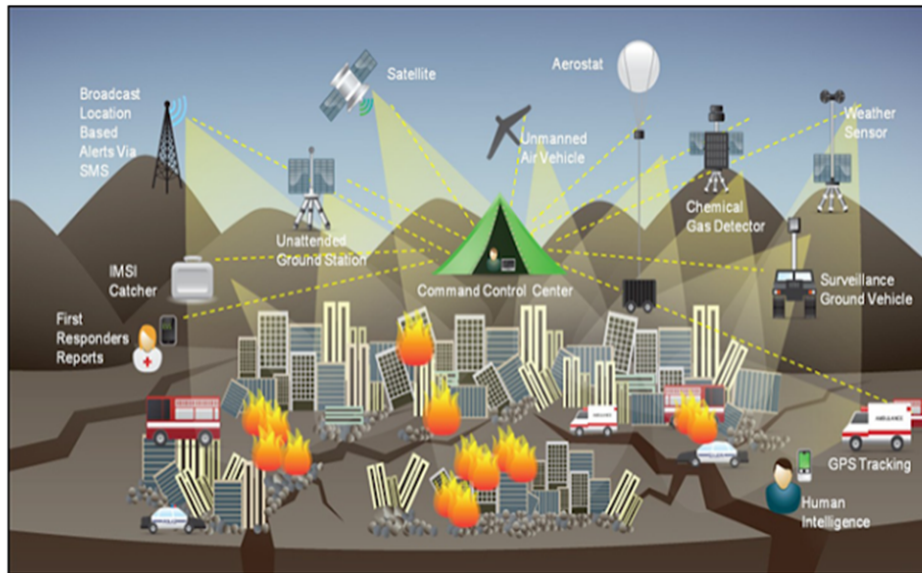
Figure 2.2: Smart city using wireless sensor network [9].

2.1 RF Sensor

The measurement of the relative permittivity of different materials (dielectric constant ϵ_r) has lots of applications such as the soil water content measurement, flow of the material measurement, water impurity, gas sensing, and material characterization [11] - [18].

Dielectric spectroscopy has been done using different techniques such as time domain
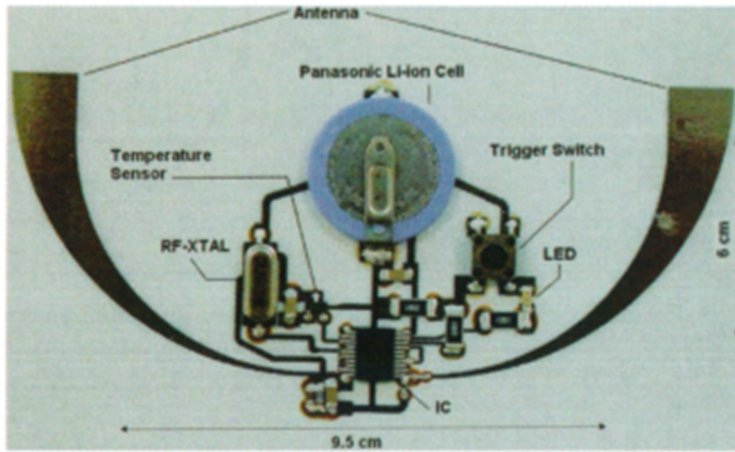
Figure 2.3: An example of a low cost sensor node [10].

reflectometry, impedance spectroscopy, frequency domain spectroscopy, and chemical test strips [19] - [34].

Time domain reflectometry works based on the Fourier analysis of the time domain changes in an incident pulse wave into a specimen and its reflection suitable for fault localization in transmission lines and biological systems [21], [22]. Fig. 2.4 shows an illustration of the basic principles of time domain reflectometry in which the sample terminates a transmission line. In this method, a rapidly increasing voltage step signal is generated and fed to the system. The incident and reflected signals are recorded and compared. Depending on the properties of the sample, which terminates the line, the reflected wave will be influenced. With this method, the complex permittivity can be extracted, but it is time-consuming due to the required time for measurement and post-processing the data, and requires wide bandwidth monitoring equipment like oscilloscope; therefore, it is not suitable for sensor nodes.

Since the permittivity of material generally can be a function of frequency, in some applications it is desired to obtain the values for the real and imaginary part of permittivity at the desired frequency [23]. In the frequency domain method, the relative permittivity of the MUT is obtained by monitoring the changes in the frequency spectrum due to changes of dielectric constant, and post-processing the input reflection coefficient or transmission coeffi-

10
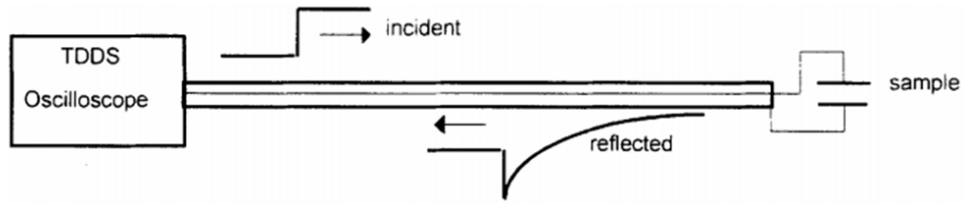
Figure 2.4: An illustration of the time domain reflectometry principle [22].
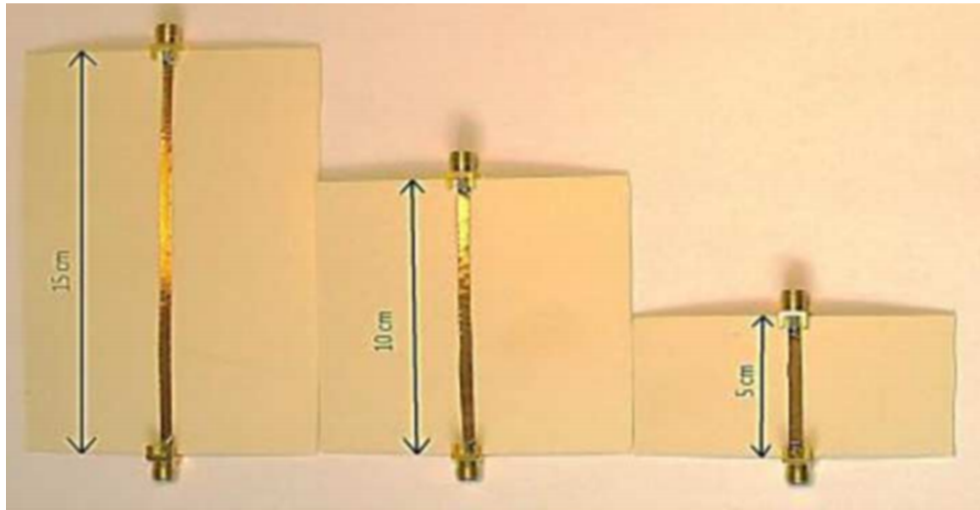
Figure 2.5: Transmission line method for wide band characterization of materials [24].

cient [24]. This method can be divided into resonator based technique in which the parameter can be extracted at resonance frequencies only, and wideband method where a continuous frequency band of the parameter response is analyzed [24]- [27].

Fig. 2.5 shows a microstrip line implemented on cardboard with identical characteristic impedance but different lengths. Since the transmission lines have different lengths, the signal arrives at the output port with different phase delays. The phase delay is correlated to the electrical length of the line which is a function of the physical length and relative permittivity of the substrate. Knowing the physical length, it is possible to extract the relative permittivity by comparing the phase delays. The losses of the substrate are extractable from the transmission loss.
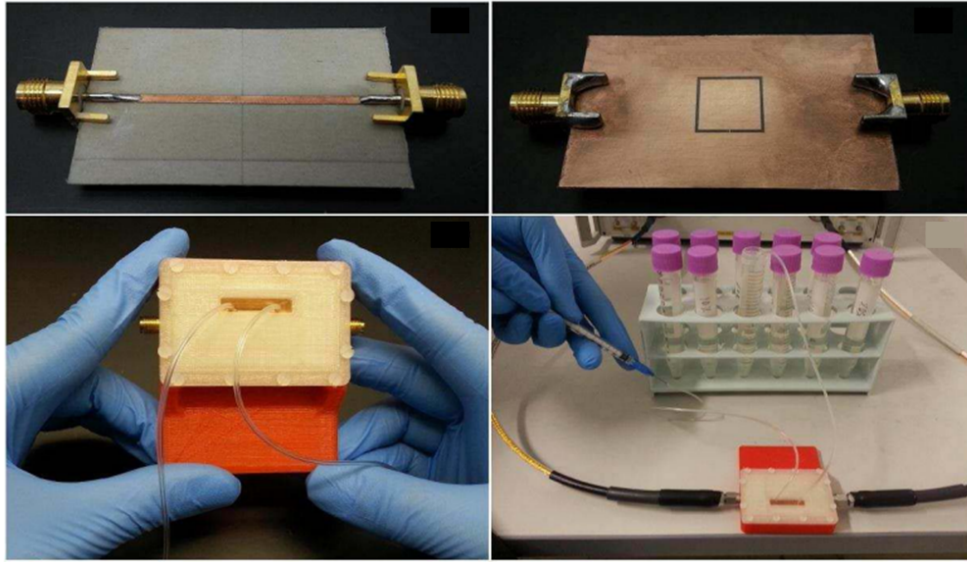
Figure 2.6: Resonator based method for characterization of materials at discrete frequencies [25].
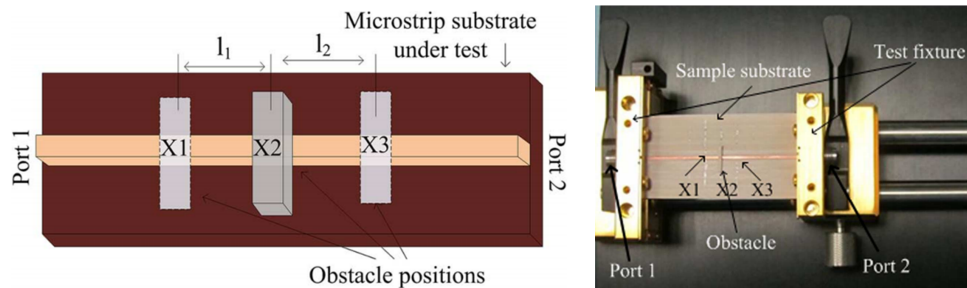
Figure 2.7: Transmission line method using obstacles for material characterization [27].

The resonator-based method is based on the changes in the resonance characteristics of an RF/Microwave resonator. By changing the relative permittivity of the material around the resonator, the resonance frequency and its bandwidth are influenced while the imaginary part affects the losses of the resonator and the quality factor of resonance. In [25] a complementary split-ring resonator (CSRR) is used on the ground plane of a microstrip line to provide larger fringing electric fields for measuring the complex permittivity of fluids depicted in Fig. 2.6.

The system was tested for different water-ethanol mixtures (which have high real permittivity range 9-80) at 1.9 GHz by measuring S-Parameters.

Transmission line method can also be utilized at higher frequencies for the extraction of substrate effective dielectric constant (DK_{eff}). In [26], Microstrip transmission lines and conductor-backed coplanar waveguides are used for the extraction of DK_{eff} up to 110 GHz by measuring S-Parameters.

A new method for substrate permittivity characterization using obstacles on microstrip line is proposed in [27]. As can be seen in Fig. 2.7, the substrate is MUT and an obstacle is placed in three different locations and S-parameters are measured. The propagation constant is extracted utilizing Line Network Network (LNN) calibration. Reasonable results are obtained for permittivity ranging between 2.55 and 9.5.

Ring resonator method and split cylinder resonator are examples of resonance method. Both of these methods have been investigated in [28] for the dielectric measurement of planar materials. The mechanism is the same; however, there are some differences on the accuracy or limitations. A microstrip ring resonator alongside the microstrip feed should be implemented on the desired planar material. Depending on the resonance frequency of system and the quality factor of the resonator, the dielectric constant and loss tangent can be extracted from the measured S-Parameters. The split cylinder resonator is a cylindrical cavity resonator excited in $TE_{01,2q+1}$ mode which is divided into two equal halves. The material which cannot exceed certain thickness compared to the dimensions of the cylinder is placed in between. The changes on the resonance frequency are correlated with the relative permittivity of the material while the losses added to the system affect the quality factor of resonance. Fig. 2.8 depicts both of the structures. In these methods, the obtained values are valid only at the resonance frequencies while the options are also limited to planar thin solid substrates.

A new method for considering the effect of air gap and thickness of the planar samples for RF sensing using a coplanar waveguide line has been proposed in [29] in which artificial neural networks (ANN) have been utilized for a computationally standalone microwave characterization system shown in Fig. 2.9. The system illustrates appropriate accuracy for the

13
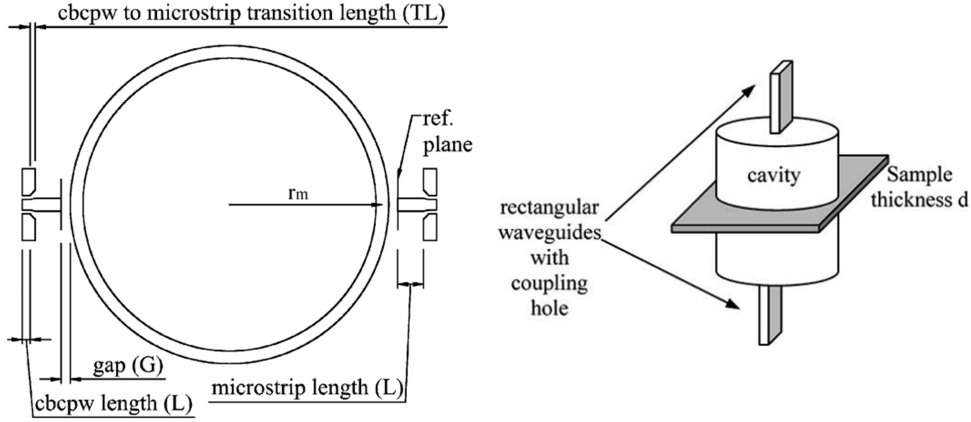
Figure 2.8: Ring resonator and split resonator configurations for material characterization [28].

detection of standard samples with relative permittivity ranging from 2.1 to 4.3 between 1 and 6 GHz. The results show up to 23% error for different thicknesses of air gap and up to 21% error for different thicknesses of samples.

A nonresonant nondestructive dielectric measurement technique using short-ended or open-ended coupled line is proposed in [30]. The complex permittivity of MUTS is determined by measuring the odd-mode effective permittivity. This system has been tested for standard samples with permittivities ranging between 3.38 and 10.35 from 1 to 6 GHz.

An active, nondestructive, contact-less and high-resolution balanced sensor structure is proposed in [31] where a reference sample is utilized to compare the effect of MUT on the circuit for permittivity extraction. The system structure is depicted in Fig. 2.10 and the obtained measured range is 1 to 12.85 for standard samples at 993 MHz.

Another active RF sensor has been proposed in [32] in which an open-loop resonator in conjunction with an injection locked loop oscillator (Fig. 2.11) is utilized to measure standard samples between 1 and 12.85 at 990 MHz.

A wireless RFID based sensor is proposed in [33] in which a substrate integrated waveguide (SIW) cavity is used as the sensor, and a transmission zero occurs in the frequency sweep

14
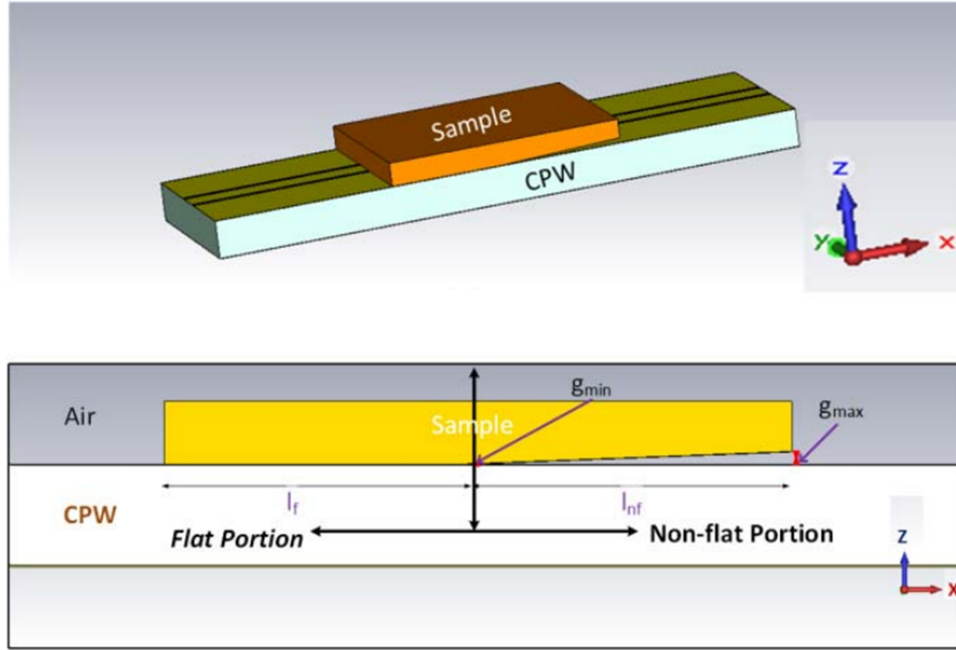
Figure 2.9: Geometry of sample including the air gap effect [29].

interrogation signal sent from the reader with a specific resonant frequency and quality correlated to the sample. This signal is transmitted back to the reader using another antenna with different polarization for minimizing the interference between interrogation and sensing signals. The geometry is shown in Fig. 2.12.

Moreover, all of the above-mentioned techniques require the monitoring and post-processing of the frequency response of the device for the characterization of the material.

Chemical test strips are also widely used in industry since they are easy to use and fast in response, but they are only limited to liquid samples [34].

2.2 Sensor Antenna

It is tempting to use antennas as sensors due to the passive capability of sensing the desired parameter. Different configurations of sensor antennas have been studied before [35] - [39]. For a dielectric sensor antenna, the resonant frequency of the antenna changes depending on

15
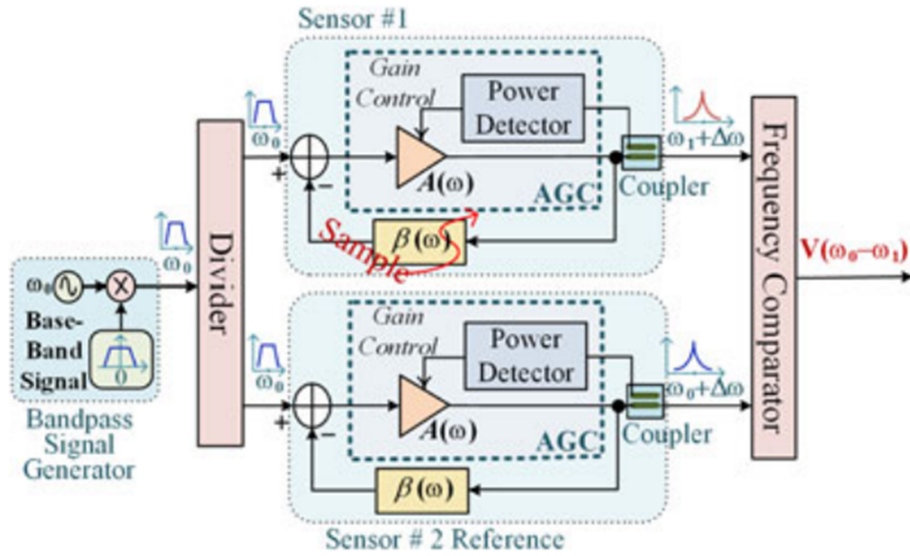
Figure 2.10: The system architecture of the high resolution balanced RF sensor [31].
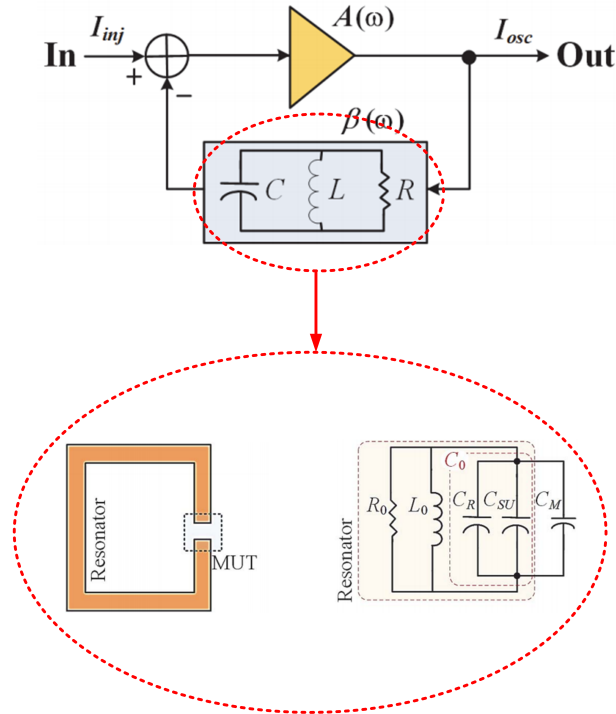
Figure 2.11: The system architecture of the injection locked oscillator RF sensor [32].
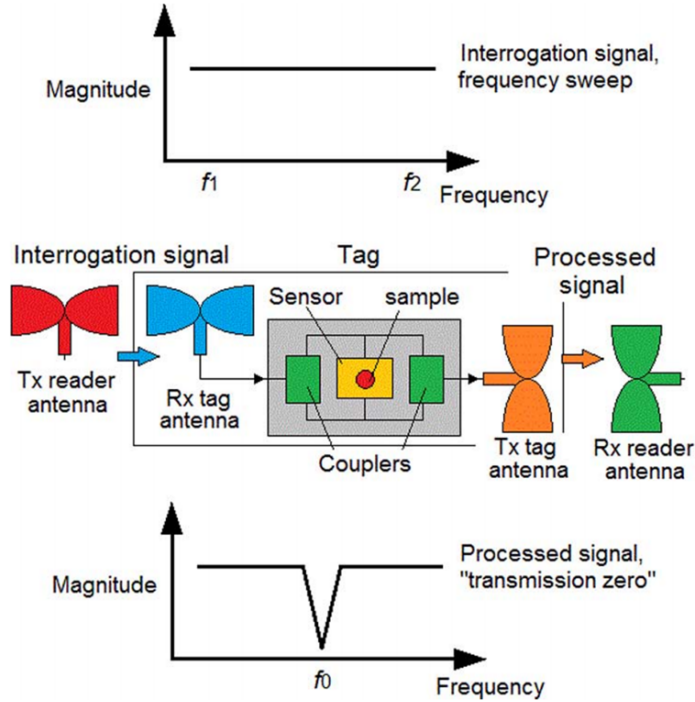
Figure 2.12: The system architecture of the RFID based wireless permittivity sensing [33].

the sample electric characteristics. Therefore, it can be categorized as dielectric resonator based frequency domain spectroscopy. A proper sensor antenna should keep the radiating characteristics (such as gain, radiation pattern, and polarization) intact while the input impedance is the only changing parameter. Since the information about the MUT is in the frequency response of the antenna, this method suffers from the same problem as other frequency domain techniques do.

Fig. 2.13 shows a Graphene-based flexible dipole sensor antenna proposed in [35] in which changing the bending radius of the curve the antenna is attached to results in changes of the antenna parameter. This antenna lacks radiation efficiency due to the poor conductivity of Graphene. In addition, the changes in the radiation pattern are imminent since there is a physical change in the shape of the antenna.

A microfluidic channel SIW based sensor for the detection of liquid chemical is represented
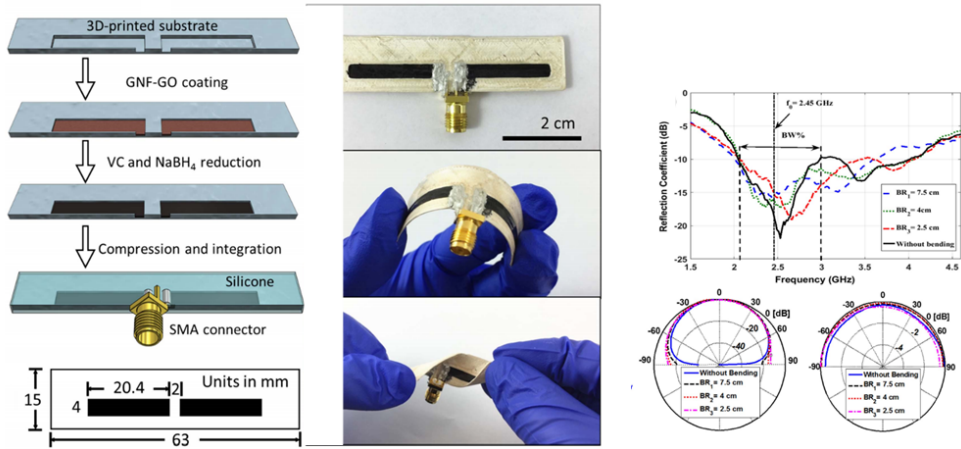
Figure 2.13: A graphene-based flexible dipole sensor antenna [35].
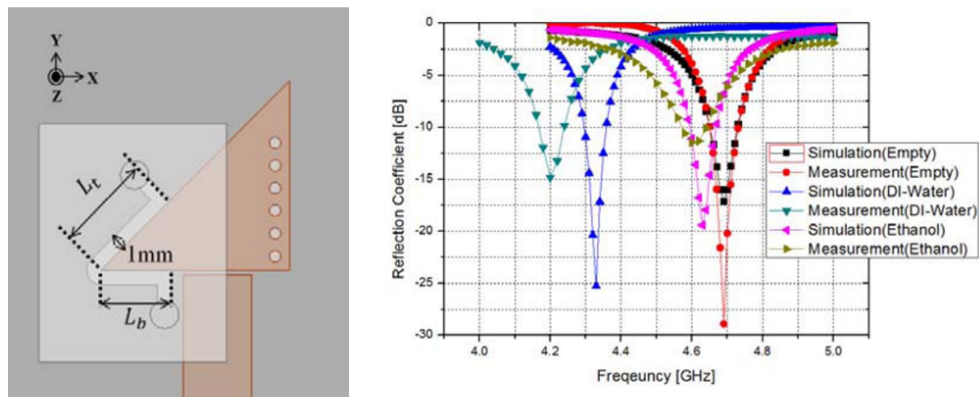
Figure 2.14: A microfluidic channel SIW based sensor antenna [39].

in [39] (Fig. 2.14). The fabrication of the microfluidic channel and placing them on the exact location are challenging and costly.

A passive wireless frequency doubling sensor antenna is depicted in [40] in which the sensing is done by the lower frequency antenna while a nonlinear passive component converts that to twice of the frequency and then send the sensing information using the secondary antenna. The system is shown in Fig. 2.15 lacks efficiency due to the losses of the passive frequency doubling system and significant reduction of the sensing antenna efficiency by increasing the measuring parameter.

18
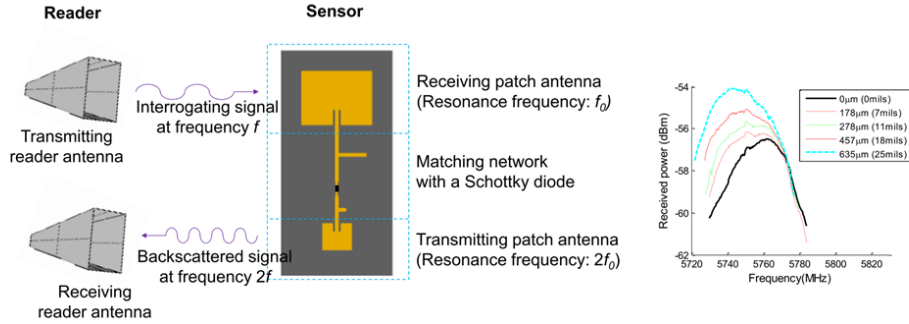
Figure 2.15: A frequency doubling crack detection sensor antenna [40].
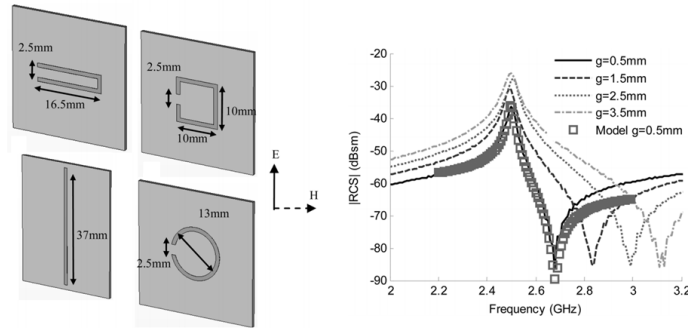
Figure 2.16: A chipless RFID sensor [41].

Fig. 2.16 shows a chipless RFID sensor proposed by [41] in which the RCS of the antenna changes in the frequency domain for different samples.

An active sensor antenna is proposed in [42], where the operating frequency of the system is provided by loading the sensing arm connected to the oscillator of the system at 7 GHz. The system configuration is presented in Fig. 2.17. The obtained permittivity range is from 1 to 10.2.

In all of these methods, the sensing information is extracted by monitoring the frequency response of the system and then post-processing them. Unfortunately, it is a costly, energy-consuming, complex, and impractical method for sensor nodes which require to be simple, low-cost and energy efficient. According to [40], a wireless sensor should convert the analog sensor signal to digital data, where most of the studied RF/Microwave and sensor antennas

19
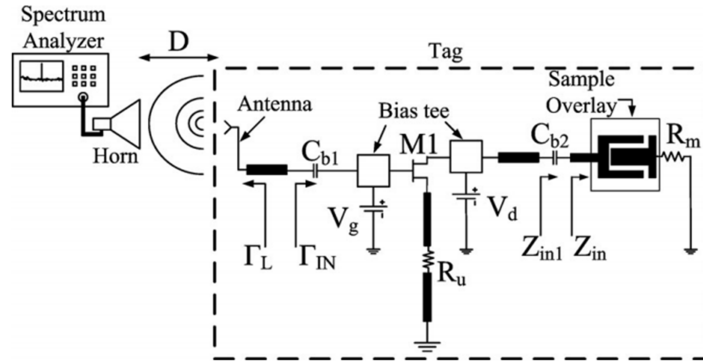
Figure 2.17: Active sensor system [42].

suffer from this aspect. They mostly need a device to measure the frequency spectrum (which is expensive and complicated in most cases) and then post-process the frequency spectrum in order to extract the sensing data. This method cannot be used as a real-time technique nor as a cost-effective method. In the past, not many attempts have been made toward an inexpensive and simple solution for the conversion of the frequency spectrum sensing signal to digital data. In this work, a practical solution for the frequency recovery of a sensor antenna system, embedded into the conventional transceiver architecture, is proposed and its feasibility is investigated.

Chapter 3

Background Theory

In this chapter, the background theory of RF sensing and circuit analysis will be discussed in detail. Firstly, the effect of permittivity on a capacitive gap will be discussed. Secondly, the VCO circuit will be studied in detail and the effect of different loadings will be investigated. Finally, it will be shown how different samples can alter the operating frequency of VCO and the relations between them.

3.1 Capacitive Permittivity Sensing

Fig. 3.1 illustrates the equivalent circuit of a one-port RF circuit. The resonant frequency of such circuit is a function of the equivalent capacitance and inductance (Eq. 3.1) that can be seen from the input port.
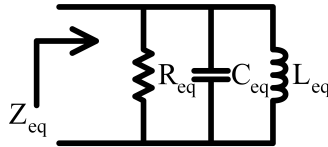
Figure 3.1: The equivalent circuit of a one-port RF circuit.

$$f_0 = \frac{1}{2\pi \sqrt{L_{eq} \times C_{eq}}} \tag{3.1}$$

where f_0 is the resonance frequency an L_{eq} and C_{eq} are the equivalent inductance and capacitance of the circuit, respectively. R_{eq} is the equivalent resistance of the circuit that represents the losses or gains in the circuit.

In an RF/Microwave sensor system, PUT alters one or more than one of these parameters resulting in a change in the frequency response of the system. If PUT alters L_{eq} and/or C_{eq}, the resonance frequency of the system will be influenced (Except for a rare case that the changes in inductance cancel out the changes in capacitance). The capacitance of an RF/Microwave circuit can be altered by changing the relative permittivity of the material as long as the other physical parameters are kept constant. Depending on the physical configuration, the equivalent capacitance can be calculated. The simplest configuration is the parallel plate capacitor shown in Fig. 3.2 where positive charges form in one conductor and negative charges on the other plate due to the voltage difference between the plates. The equivalent capacitance of such capacitor, considering the dimensions of the plates, is way larger than the distance between the plates; hence, neglecting the fringing fields effect at the edges of the conductors can be calculated as 3.2 considering the homogeneous and isotropic dielectric constant [43], [44]
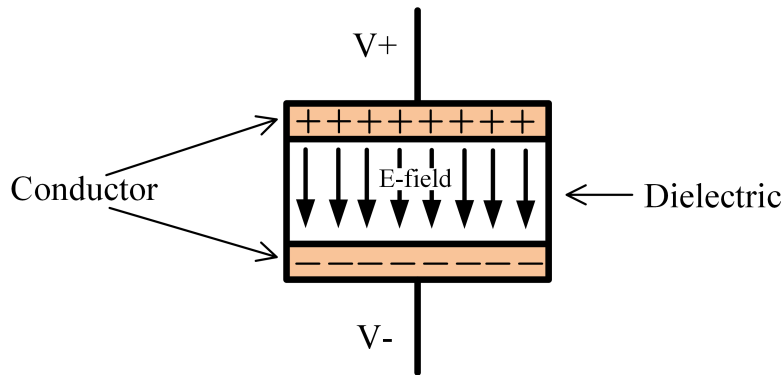
Figure 3.2: The charge and electric field distributions in a parallel plate capacitor.

$$C_{parallelplate} = \frac{\epsilon A}{d} \tag{3.2}$$

where ϵ is the dielectric constant of the dielectric materials between the plates, A is the area

of plates, and d is the distance between them. If the area of the plates is not significantly larger than the distance between the plates, then the fringing fields affect the capacitance.

Since the capacitance is a function of the relative permittivity of the medium, it can be a good candidate for sensing the dielectric constant of unknown materials. For adaptability to the electronic circuit, it is more desirable to have a planar printed sensor rather than 3-Dimensional structures.

The simplest form of a planar capacitor is made of two parallel metal sheets on the same side of a PCB without any ground plane. Fig. 3.3 shows an example of such capacitor including the electric fields around the gap between the metal traces. As can be seen, due to the small thickness of the conductors, the fringing fields become influential on the total capacitance of the gap. The fields in the gap E_g are the same as the fields between the two parallel plates although the material between them is air in the case of PCB circuit. There are four sets of fringing fields around the gap from which three are forming in air E_{air}. Two sets of fields are forming on the two sides of the gap and one is above the system. The fields forming in the substrate E_{sub} below the gap are influenced by the dielectric constant of the substrate. Since the thickness of the conductors is small, these fringing fields become comparable to E_g; therefore, they should be considered in the equivalent capacitance which is defined in 3.3. The capacitance of the gap (C_g) is defined by 3.4 and can be calculated like the parallel plate capacitor in 3.2.
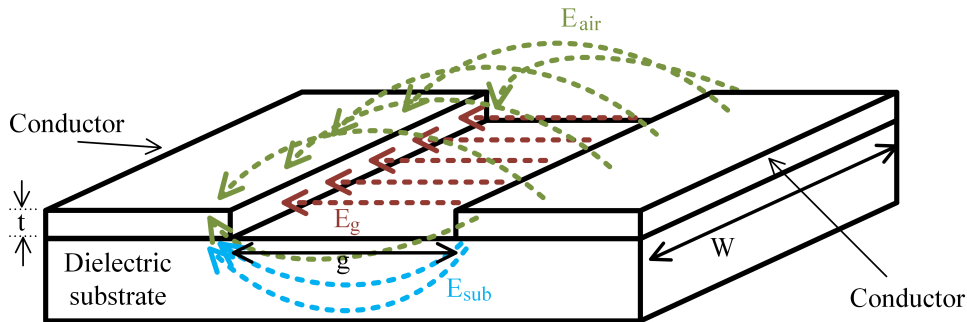
Figure 3.3: The planar capacitor on a PCB.

23

$$C_{equivalent} = C_g + C_{air} + C_{sub} \qquad (3.3)$$

$$C_g = \frac{\epsilon_0 W t}{g} \qquad (3.4)$$

where ϵ_0 is the permittivity of air which is the material between the conductors, W and t are width and thickness of the conductor traces, respectively, and g is the gap distance between the conductors. The configuration becomes more complicated when a sample with a specific dielectric constant is placed on top of the planar capacitor. As can be seen in Fig. 3.4, if the thickness of the sample on top and substrate at the bottom (h_1 and h_2, respectively) is high enough and the length of conductors in X direction is long enough so that all the fringing fields form inside the sample and substrate and do not leak into the air, it can be possible to calculate the total capacitance using 3.5. It is worth mentioning that there will be some fringing fields in the air in X-Z plane, but all the fields in the X-Y plane are inside the sample or substrate [45], [47].
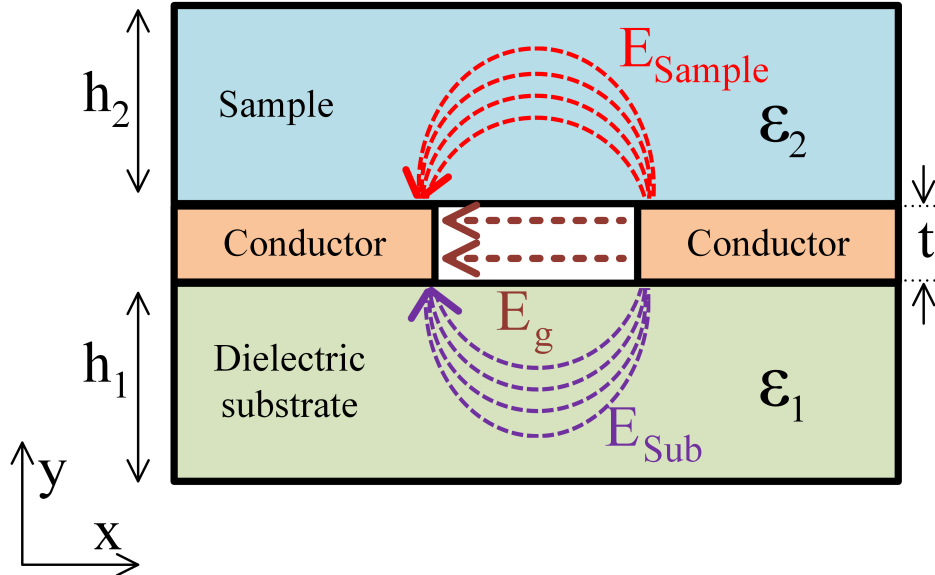
Figure 3.4: The planar capacitor on a PCB and the fringing fields with a sample.

$$C_{equivalent} = C_g + C_{sub} + C_{sample} \tag{3.5}$$

$$C_{sub} = \frac{\epsilon_1 W}{2}[\frac{K(k_1')}{K(k_1)}] \tag{3.6}$$

where $K(k_1')$ and $K(k_1)$ are the complete elliptic integrals of the first kind with

$$k_1 = tanh(\frac{\pi g}{4h_1}) \tag{3.7}$$

$$k_1' = \sqrt{1 - (k_1)^2} \tag{3.8}$$

$$C_{sample} = \frac{\epsilon_2 W}{2}[\frac{K(k_2')}{K(k_2)}] \tag{3.9}$$

where $K(k_2')$ and $K(k_2)$ are the complete elliptic integrals of the first kind with

$$k_2 = tanh(\frac{\pi g}{4h_2}) \tag{3.10}$$

$$k_2' = \sqrt{1 - (k_2)^2} \tag{3.11}$$

The portion of the fringing fields forming in air on the sides of the circuit can be compensated using Maxwell approximation by extending the width of the conductors to $g/2$ on each side, resulting in new equivalent width $W + g$ [44]. Therefore, the revised C_g which includes the fringing field on the sides can be re-written as 3.12.

$$C_g = \frac{\epsilon_0(W + g)t}{g} \tag{3.12}$$

For the cases where there might be an air gap between the sample and circuit (Fig. 3.5) and the fields might not be confined inside the samples and substrate, the following conversion

for C_{sample} and C_{sub} can be used to include the effect of air gap in which effective permittivity ϵ_{eff} with effective thickness h_{eff} replaces the initial sample and air gap. The conversion is coming from a conformal mapping of a slotline structure by substituting the materials with the equivalent effective permittivity value with a virtual equivalent thickness [46], [47].
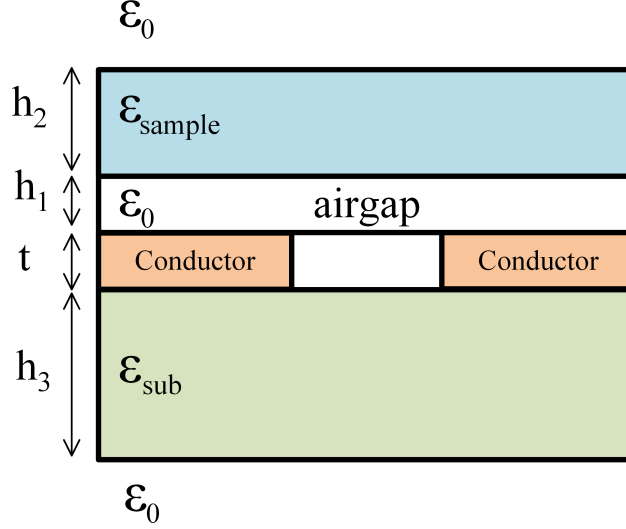
Figure 3.5: The effect of air gap between sample and circuit.

$$C'_{sample} = C_{sample} + C_{air-gap} = \frac{\epsilon'_{sample} A'_{sample}}{g} \tag{3.13}$$

$$C'_{sub} = \frac{\epsilon'_{sub} A'_{sub}}{g} \tag{3.14}$$

$$\epsilon'_{sample} = 1 + \frac{1 - \epsilon_{sample}}{2} + \frac{\epsilon_{sample} - 1}{2} \cdot [\frac{K'(k_{sample})}{K(k_{sample})}] \cdot [\frac{K(k_0)}{K'(k_0)}] \tag{3.15}$$

$$h'_{sample} = (h_1 + h_2)[1 + \frac{0.0133}{\epsilon_{sample} + (1 - \epsilon_{sample}) \cdot \frac{h_1}{h_1 + h_2} + 2} (\frac{\lambda}{h_1 + h_2})^2] \tag{3.16}$$

$$A'_{sample} = h'_{sample}.W \tag{3.17}$$

$$A'_{sub} = h'_{sub}.W \tag{3.18}$$

$$h'_{sub} = h_3[1 + \frac{0.0133}{\epsilon_{sub} + 2}.(\frac{\lambda}{h_3})^2] \tag{3.19}$$

$$\epsilon'_{sub} = 1 + \frac{\epsilon_{sub} - 1}{2}.\frac{K(k'_{sub})}{K(k_{sub})}.\frac{K(k_0)}{K(k'_0)} \tag{3.20}$$

where λ is the free space wavelength, h_1, h_2, and h_3 are the thickness of air gap between sample and circuit, sample and substrate, respectively. ϵ_{sample}, ϵ_{sub}, ϵ'_{sample}, and ϵ'_{sub} are the relative permittivity of the sample, substrate, and the equivalent effective permittivities considering the effect of air around sample and substrate, respectively. This method is valid for $0.01 \leq \frac{\lambda}{h}$. 3.16 and 3.19 show that by increasing the permittivity of the sample and/or substrate, the equivalent effective height decreases, meaning that the electric fields become more concentrated around the slot area. The same effect can be seen by increasing the operating frequency (decreasing the wavelength).

If the RLC tank in Fig. 3.1 is used as a sensor in which C_{eq} is the only variable component with respect to PUT, the deviation of the resonance frequency with changes of the capacitance can be explained as 3.21.

$$\frac{\partial f_0}{\partial C_{eq}} = \frac{-2\pi^2 L_{eq}}{\sqrt{(4\pi^2 L_{eq} C_{eq})^3}} \tag{3.21}$$

In planar capacitor configuration depicted in Fig. 3.3, the only capacitor that changes with MUTS is C_{sample}, which is a function of MUT's relative permittivity. The dependency of C_{sample} to the permittivity of samples can be obtained by finding the derivative with respect to ϵ_{sample}. For the case where there is no air gap and the sample and substrate are thick enough to confine the fields inside, 3.22 shows the dependency.

$$\frac{\partial C_{sample}}{\partial \epsilon_{sample}} = \frac{W}{2}[\frac{K(k_2')}{K(k_2)}] \tag{3.22}$$

3.23 presents the dependency for the case where there is an air gap and the materials are not thick enough to confine the fields inside.

$$\frac{\partial C'_{sample}}{\partial \epsilon_{sample}} = (W((K(k_0)K'(k_s))/(2K'(k_0)K(k_0)) - 1/2)(h1 + h2))$$

$$\times \frac{((0.0133\lambda^2)/((h_1 + h_2)^2(\epsilon_{sample} - (h_1(\epsilon_{sample} - 1))/(h_1 + h_2) + 2)) + 1)}{g}$$

$$+ \frac{(0.0133\lambda^2 W(h_1/(h_1 + h_2) - 1)((K(k_0)K'(k_s)(\epsilon_{sample}/2 - 1/2))/(K'(k_0)K(k_s)) - \epsilon_{sample}/2 + 3/2))}{(g(h_1 + h_2)(\epsilon_{sample} - (h_1(\epsilon_{sample} - 1))/(h_1 + h_2) + 2)^2)} \tag{3.23}$$

3.2 VCO Circuit Analysis

VCO is one of the fundamental parts in communication circuits providing the carrier RF frequency for signal transmission in the upconversion process or providing a baseband signal at the receiver in the downconversion process. The operating frequency of a VCO can be accurately controlled using a control voltage. Fig. 3.6 (a) to (c) illustrate a general block diagram of a VCO, the ideal frequency-, and time-domain output, respectively. The nature of oscillation is based on the back and forth flow of energy between two energy storage modes. In the ideal case where there is no dissipation, the oscillation lasts forever while in reality due to the losses of components the magnitude of oscillation degrades in each cycle [48]. Fig. 3.7 shows an ideal, realistic, and negative-resistance compensated LC resonator and its outputs. In order to maintain the oscillation and its magnitude, there should be a negative resistance to compensate for the losses.

If oscillation occurs in the circuit shown in Fig. 3.7 (e), then the following conditions are
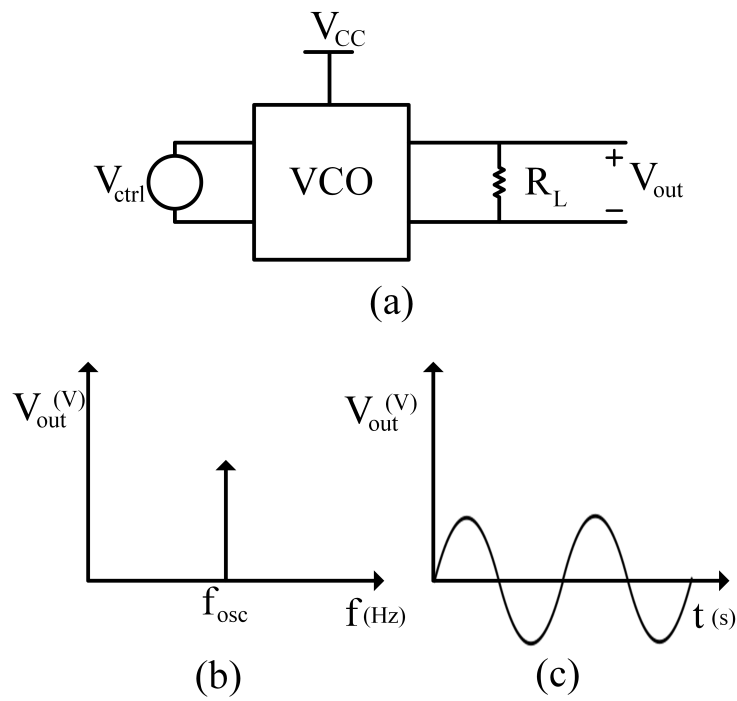
Figure 3.6: VCO (a) general block diagram, (b) ideal frequency-domain output and (c) ideal time-domain output.
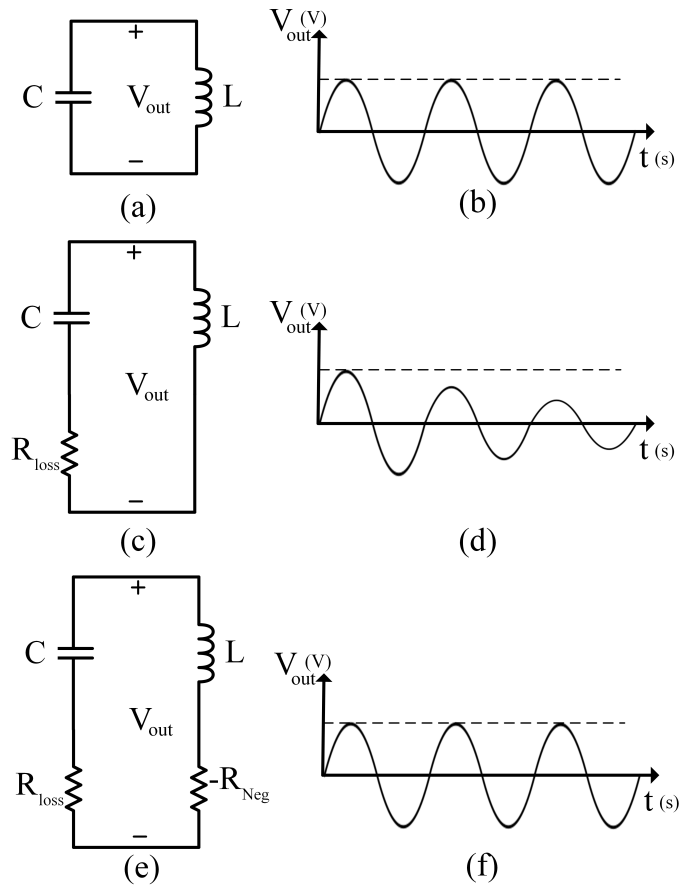
Figure 3.7: LC resonator (a) ideal circuit, (b) ideal time-domain output, (c) realistic circuit, (d) realistic output, (e) with negative resistance, and (f) the compensated output.
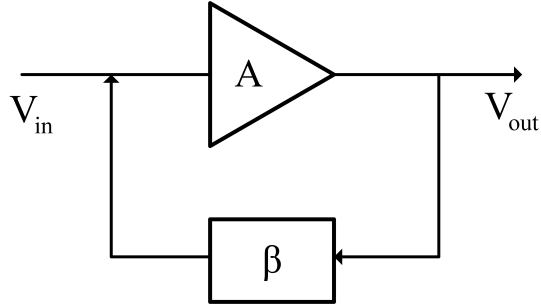
Figure 3.8: Block diagram of a feedback oscillator.

applied.

$$R_{loss} - R_{Neg} = 0 \tag{3.24}$$

$$j\omega L + \frac{1}{j\omega C} = 0 \tag{3.25}$$

where R_{loss} represents the losses in the system, $-R_{Neg}$ which is the negative resistance represents sources of energy as an active component, and L and C are the reactances in the system.

It is very common to use a feedback mechanism to obtain stable RF oscillation. In a feedback system depicted in Fig. 3.8, if the phase shift around the loop is multiple of 360° and the open loop gain is one, then stable oscillation is provided [49]. These conditions are applied to the steady-state operation and are called Barkhausen Criterion presented in 3.27 and 3.28.

$$\frac{V_{out}}{V_{in}} = \frac{A}{1 - A\beta} \tag{3.26}$$

$$A\beta = 1 \tag{3.27}$$

$$\Phi_A + \Phi_\beta = 0, 2\pi, 4\pi, ... \tag{3.28}$$

where A is the forward transfer function, β is the feedback transfer function, and Φ_A and Φ_β are the phase response of forward and feedback passes, respectively. If 3.27 and 3.28 both
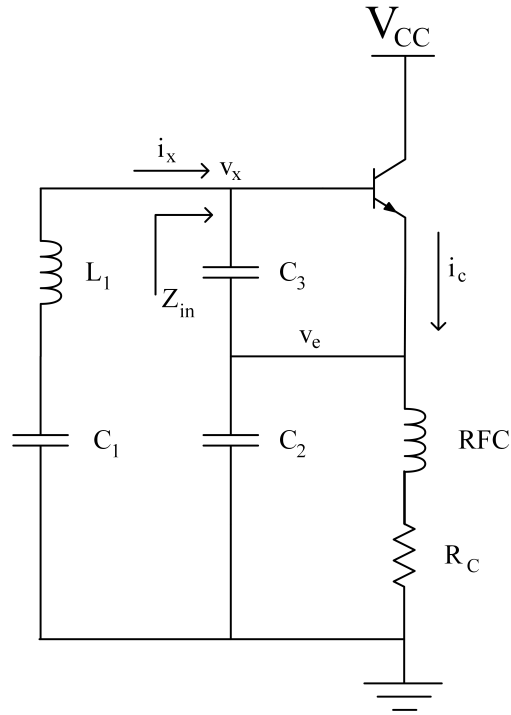
Figure 3.9: General configuration of a Colpitts oscillator.

satisfy at the same time, the voltage gain of the system 3.26 is infinite which means the system resonates.

The start-up condition (3.29 and 3.30) for a feedback oscillator is slightly different and requires higher voltage gain to ensure the oscillation starts even using the available noise in the system and not an external impulse or signal.

$$A\beta > 1 \tag{3.29}$$

$$\Phi_A + \Phi_\beta = 0, 2\pi, 4\pi, ... \tag{3.30}$$

Gain A in Fig. 3.8 can be provided by active circuit. A common configuration of such system is Colpitts oscillator illustrated in Fig. 3.9. By using KVL and KCL, it is possible to find the input impedance of the circuit Z_{in} using 3.31 to 3.34.

32

$$i_x Z_{c_1} \approx V_{be} = v_x - v_e \tag{3.31}$$

$$v_x = V_{be} + (i_c + i_x)Z_{c_2} \tag{3.32}$$

$$v_x = i_x Z_{C_1} + (i_c + i_x)Z_{C_2} = i_x(Z_{C_1} + Z_{C_2}) + g_m i_x Z_{C_1} Z_{C_2} \tag{3.33}$$

$$Z_{in} = \frac{v_x}{i_x} = \frac{C_1 + C_2}{j\omega C_1 C_2} - \frac{g_m}{\omega^2 C_1 C_2} \tag{3.34}$$

As can be seen, the term $-\frac{g_m}{\omega^2 C_1 C_2}$ is the negative resistance or, in other words, the gain of the system to compensate for the losses of the components. The operating frequency of Colpitts oscillator in Fig. 3.9 can be calculated as

$$f_0 = \frac{1}{2\pi\sqrt{L_1(C_1|C_2|C_3)}} \tag{3.35}$$

where | is the series configuration symbol.

If a tunable component is used instead of the fixed capacitor C_1 in the tank circuit at the base of the transistor, the operating frequency of the oscillator can be controlled and if this component is a varactor in which the capacitance is controlled by a bias voltage, then a VCO is obtained.

3.3   Capacitive Loading of VCO

Traditionally, VCOs are designed to have a fixed conventional 50 Ω load. In this section, the effect of each component on the operating frequency and the output power of the system are investigated. It is assumed that the tank, load of the system, and the feedback circuits are general impedances Z_1, Z_L, Z_2 and Z_3, respectively (Fig. 3.10). The input impedance Z_{in} from the base of the transistor can be re-written as
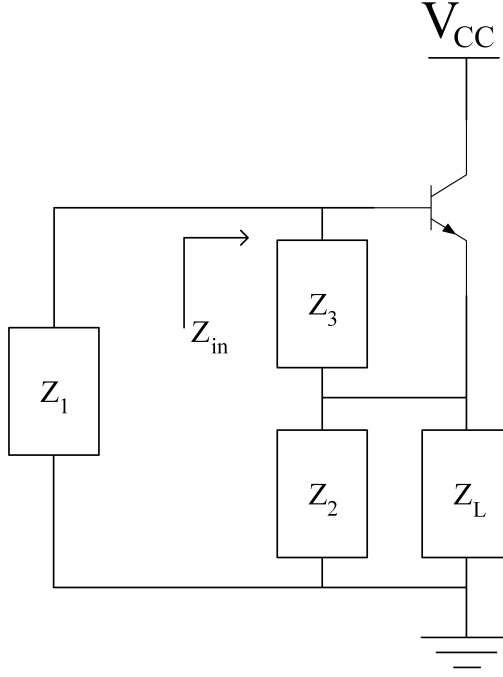
Figure 3.10: Colpitts oscillator with general impedances.

$$Z_{in} = Z_3 + (Z_2||Z_L) + g_m Z_3 (Z_2||Z_L) = R_{in} + jX_{in} \tag{3.36}$$

where

$$Z_2||Z_L = Z_2' = R_2' + jX_2' = \frac{R_2 R_L (R_2 + R_L) + R_2 X_L^2 + R_L X_2^2}{(R_2 + R_L)^2 + (X_2 + X_L)^2}$$

$$+j \frac{(R_2 X_L + R_L X_2)(R_2 + R_L) - (X_2 + X_L)(R_2 R_L - X_2 X_L)}{(R_2 + R_L)^2 + (X_2 + X_L)^2} \tag{3.37}$$

For obtaining the resonance frequency of the circuit, the imaginary parts of Z_1 and Z_{in} should cancel each other out.

$$X_{in} = X_3 + X_2' + g_m (R_3 X_2' + R_2' X_3) = -X_1 \tag{3.38}$$

where $X_1 = \omega L_1 - \frac{1}{\omega C_1}$ is the reactance of the series tank at the base and X_L is the reactance of the RLC tank as the load. If Z_2 and Z_3 are capacitance but Z_1 and Z_L are RLC tanks,

34

then R_2 and R_3 are zero and $X_2 = -\frac{1}{\omega C_2}$ and $X_3 = -\frac{1}{\omega C_3}$,

$$R'_2 = \frac{R_L X_L^2}{R_L^2 + (X_2 + X_L)^2} \tag{3.39}$$

$$X'_2 = \frac{X_2(R_L^2 + X_2 X_L + X_L^2)}{R_L^2 + (X_2 + X_L)^2} \tag{3.40}$$

$$X_{in} = X_3 + X'_2 + g_m(R'_2 X_3) \tag{3.41}$$

$$X_{in} = (-1 - C_2 C_L^2 L_L^2 R_L^2 (C_2 + C_3)\omega^6 - 2(((\frac{R_L g_m}{1} + \frac{1}{2})C_2^2 + (\frac{C_3}{2} - C_L)C_2$$

$$-\frac{C_L(C_3 - C_L)}{2})L_L + C_2 C_L R_L^2 (C_2 + C_3)L_L\omega^4 + ((2C_2 + C_3 - 2C_L)L_L - C_2 R_L^2(C_2 + C_3)\omega^2)))$$

$$/((1 + C_2^2 C_L^2 L^2 L R_L^2 \omega^6 + 2((\frac{(C_2 - C_L)^2 L_L}{2}) + C_2^2 C_L R_L^2)L_L\omega^4 + ((-2C_2 + 2C_L)L_L + C_2^2 R_L^2)\omega^2)\omega C_3)$$
$$\tag{3.42}$$

Unfortunately, this equation does not have an algebraic solution for the roots; therefore, it is impossible to find the roots and a general description of how the operating frequency is a function of each element. Therefore, in the next section, the circuit will be analyzed for the elements affecting its operating frequency and how the RLC tank on the output affects it. This RLC circuit represents the sensor element in the system.

If a parallel RLC tank similar to Fig. 3.1 is utilized as the load of VCO and a varactor as the tuning component at the base, the circuit illustrated in Fig. 3.11 is obtained. Assuming the circuit has the capability to operate from 700 MHz to 1.5 GHz, the effect of R_L, C_L, C_{var}, C_2 and C_3 on operating frequency and output power are analyzed, and the results are

35
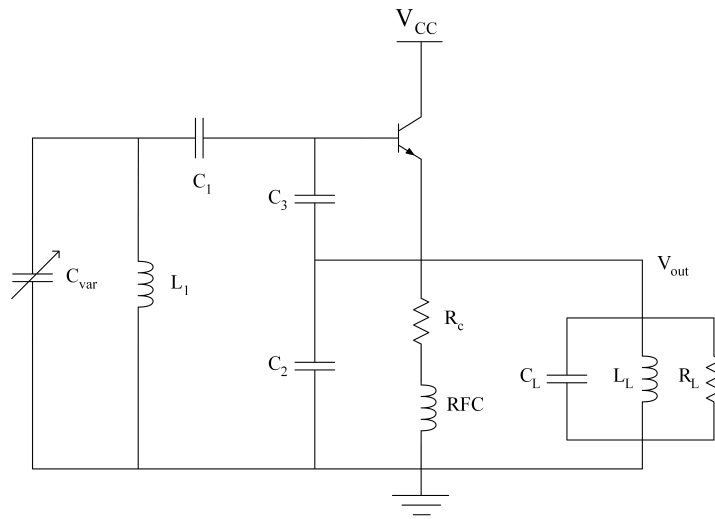
Figure 3.11: Colpitts oscillator with an RLC tank as a load.

shown in Fig. 3.12 to Fig. 3.16. As can be seen in Fig. 3.12, at small values of R_L the VCO does not have much output power since the circuit is loaded with small resistance resulting in the gain reduction of the open loop amplifier. The maximum operating frequency occurs at 150 Ω while the maximum output power occurs at 60 Ω and 100 to 150 Ω. The operating frequency increases from lower resistances up to 150 Ω and decreases after 250 Ω while the output power increases to 10 dBm at 60 Ω, fluctuates a little bit up to 150 Ω and then decreases for higher values.

Fig. 3.13 shows that for C_L, 13 pF to 30 pF is the operating range for the circuit in which the operating frequency reduces with increasing the capacitance. Since the circuit is optimized for the initial state ($C_L = 13$ pF), increasing the capacitance causes output power degradation by influencing the open loop gain. Values higher than 30 pF do not alter the operating frequency due to the huge difference between the resonant frequency of tank and circuit. It can be deduced that for values of the capacitance resulting in resonant frequency of the output tank, which later will be replaced with the sensor, close to the operating frequency of VCO, it is possible to alter the frequency of system: however, when the resonant frequency

36
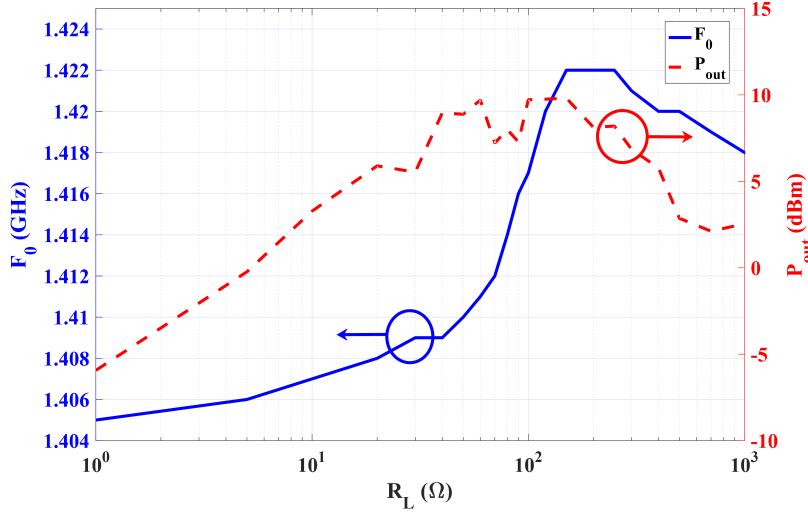
Figure 3.12: The simulation results for the operating frequency and output power of VCO versus different load resistance.

of the tank is far from the operating frequency of VCO, the influence diminishes. Due to the open-loop gain reduction, the output power decreases significantly by increasing the capacitance.

The effect of C_{var} is also depicted in Fig. 3.14 in which by increasing the capacitance, the operating frequency decreases. It is worth mentioning that the tuning range obtained by C_{var} (0.7-1.4 GHz for 0.7 to 4.15 pF) is much more than that of C_L (1.405-1.413 GHz for 13 to 30 pF). The output power of the system also decreases due to having a tank as a load with the resonant frequency of 1.4 GHz. When C_{var} increases, the circuit tends to have lower operating frequency; however, the load has different characteristics at frequencies other than the resonant frequency; therefore, the practical operating range decreases.

The effect of feedback capacitors C_2 and C_3 on the operating frequency is also presented in Fig. 3.15. The effect is very similar to C_{var} but again the tuning range is smaller.

As it was mentioned before, the RLC tank, as the load of the VCO, is the RF sensor whose capacitance changes for different MUTS. Therefore, having 3.23 and Fig. 3.13, it is possible to obtain the influence of a certain permittivity on the operating frequency of the
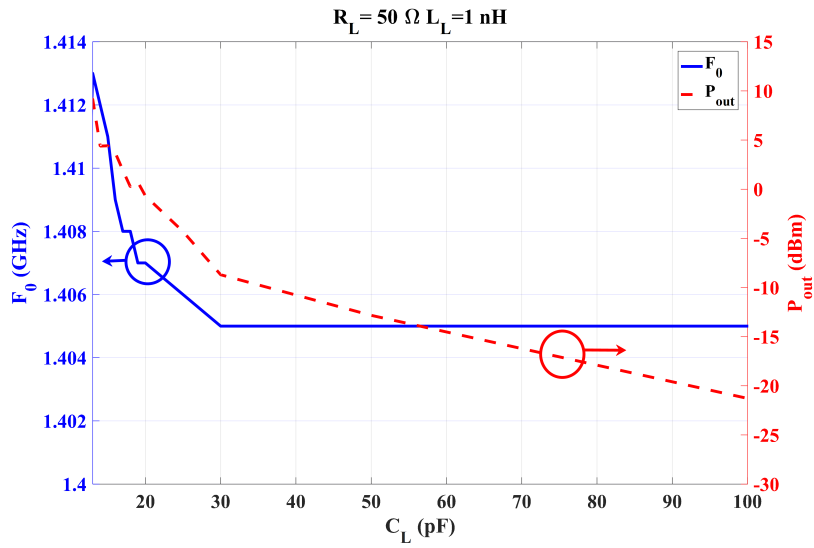
Figure 3.13: The simulation results for the operating frequency and output power of VCO versus different load capacitance.
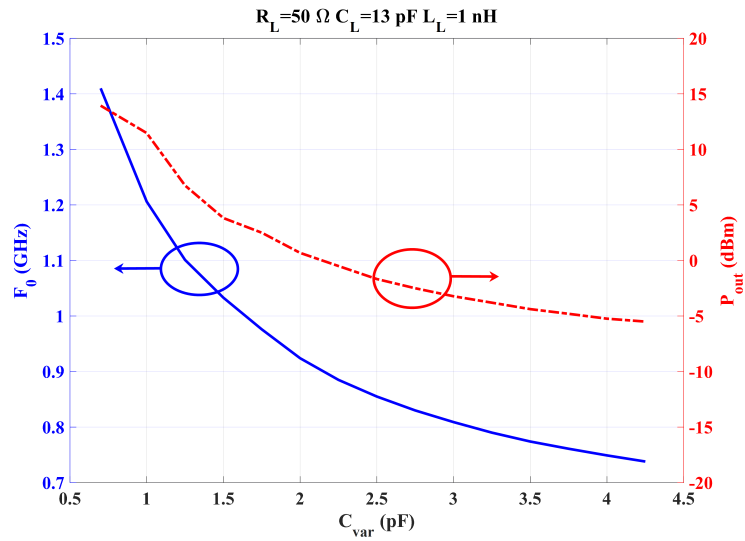
Figure 3.14: The simulation results for the operating frequency and output power of VCO versus different varactor capacitance.
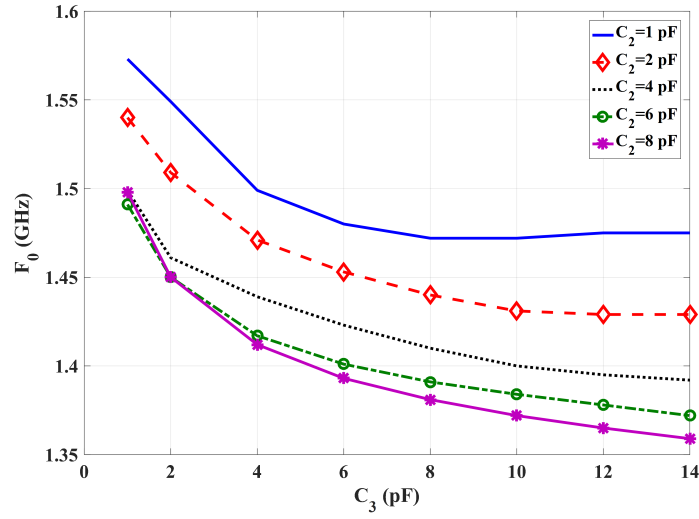
Figure 3.15: The simulation results for the operating frequency of VCO versus different C_2 and C_3.
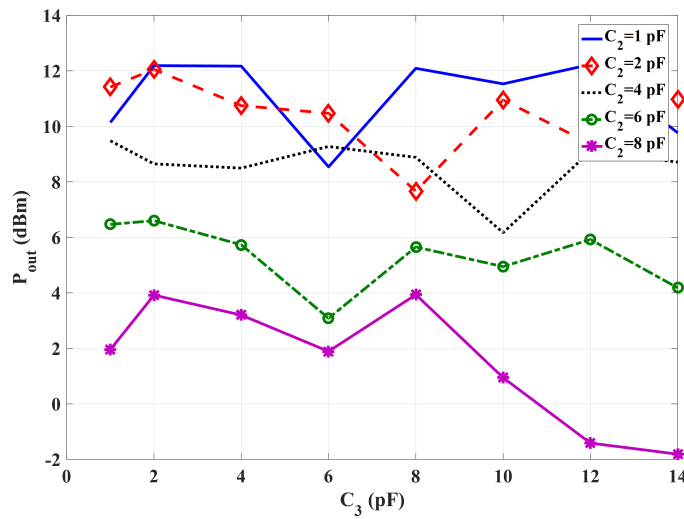
Figure 3.16: The simulation results for the output power of VCO versus different C_2 and C_3.

Figure 3.17: The equivalent circuit of the VCO and load.

VCO.

3.4   Oscillator Load Pulling

The load pulling effect on an oscillator is defined as the frequency change produced by alteration in load impedance. Considering the simple case shown in Fig. 3.19 in which R_L, C_L, and L_L are the equivalent resistance, capacitance, and inductance of load, respectively while, on the other hand, R_{osc}, C_{osc} and L_{osc} are the oscillator equivalent resistance, capacitance, and inductances, respectively. Assuming that the load is tuned to the operating frequency of oscillator, it is possible to have [49]- [51]

$$\omega_l = \omega_0 = \frac{1}{\sqrt{(L_{osc}C_{osc})}} = \frac{1}{\sqrt{(L_L C_L)}} = \frac{1}{\sqrt{\frac{L_L L_{osc}(C_L + C_{osc})}{L_L + L_{osc}}}} \tag{3.43}$$

$$Q_l = \omega_0 C_L R_L \tag{3.44}$$

$$Q_L = \omega_0 C_{osc} R_L \tag{3.45}$$

An increment in C_L which is equivalent to change in PUT for the sensor loading the oscillator, the frequency shift can be given by

$$\frac{d\omega}{\omega_0} = -\frac{dC_L}{2(C_L + C_{osc})} = -\frac{Q_l}{2(Q_l + Q_L)}\frac{dC_L}{C_L} \qquad (3.46)$$

3.46 shows how much the operating frequency of oscillator can be altered if the load capacitance which is the sensor capacitance (C_L) changes [49]- [51].

If the nonlinearity of the oscillator impedance (α) is taken into account, at the stead-state we have

$$\alpha = \frac{\partial B}{\partial V} \Big/ \frac{\partial G}{\partial V} \qquad (3.47)$$

$$Y = Y_{osc} + Y_L = 0 \qquad (3.48)$$

For a load perturbation of $\Delta Y_L = \Delta G_L + j\Delta B_L$, where G_L is the load conductance, and B_L is the load susceptance, the oscillation condition can be rewritten as 3.49

$$Y + \Delta Y_L + \frac{\partial Y}{\partial \omega}\Delta\omega + \frac{\partial Y}{\partial V}\Delta V = 0 \qquad (3.49)$$

where V is the voltage amplitude across the load [49]- [51].

The maximum total frequency deviation for the case when $\frac{\partial G}{\partial \omega} = 0$ and $|\Gamma_L|^2 \ll 1$ can be calculated as

$$\Delta\omega_{max} = \frac{2\omega_0}{Q_L}\frac{S-1}{S+1}\sqrt{\alpha^2 + 1} \qquad (3.50)$$

where

$$Q_L = \frac{\omega_0}{2Y_0}\frac{\partial B}{\partial \omega} \qquad (3.51)$$

is the loaded quality factor of the oscillator resonant circuit and

$$S = \frac{1 + |\Gamma_L|}{1 - |\Gamma_L|} \qquad (3.52)$$

41

As can be see, The maximum frequency deviation due to the load pulling is limited by the loaded quality factor, and has an inverse relationship.

3.5   Magnetic Coupling in Metal Proximity

In this section, firstly, the equivalent circuits of the system consisting of the NFC and RFID are investigated. Then, the circuit model is modified in order to include the effect of the booster. The performances of these two systems are analytically compared to the transferred power point of view. Finally, the effect of the metal asset is added to this model. This section explains how the system performs and how each element affects the total performance of a passive booster for the enhancement of the communication range.

The Z-Parameters of the two coupled coils shown in Fig. 3.18 can be defined by (3.53) and (3.54). In this model, V_i, I_i, and L_i are the phasor of voltage, phasor of current, and inductance of each coil, respectively while M_i is the coupling between them.
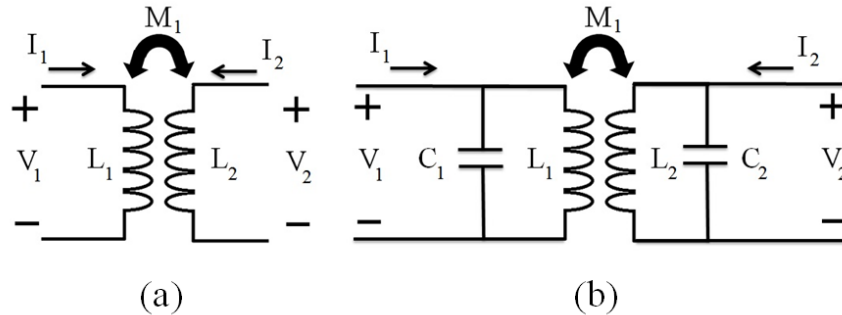
Figure 3.18: The equivalent circuit of (a) two coupled coils and (b) the resonating system.

$$V_1 = j\omega L_1 I_1 + j\omega M_1 I_2 \tag{3.53}$$

$$V_2 = j\omega M_1 I_1 + j\omega L_2 I_2 \tag{3.54}$$

where ω is the angular frequency. For increasing the transferred power between these two coils the resonance condition is provided by adding a shunt capacitor at each side represented

in Fig. 3.18 (b). Assuming perfect matching at each port, the transferred power from the input port to the output port will be equal to $|S_{21}|^2$. The $ABCD$ matrix of the whole resonating system is calculated utilizing the $ABCD$ matrix of C_1, $L_1 - M_1 - L_2$, and C_2 in order to find the transferred power. Then S_{21} can be easily found as (3.58) by an $ABCD$-to-S transformation.

$$ABCD_{L_1-M_1-L_2} = \frac{1}{j\omega M_1} \begin{bmatrix} j\omega L_1 & \omega^2(M_1^2 - L_1 L_2) \\ 1 & j\omega L_2 \end{bmatrix} \tag{3.55}$$

$$ABCD_{C_i} = \begin{bmatrix} 1 & 0 \\ j\omega C_i & 1 \end{bmatrix} \tag{3.56}$$

$$ABCD_{total} = ABCD_{C_2} \times ABCD_{L1-M_1-L2} \times ABCD_{C_2}$$

$$= \frac{1}{j\omega M_1} \begin{bmatrix} j\omega(L_1 + \omega^2 C_2(M_1^2 - L_1 L_2)) & \omega^2(M_1^2 - L_1 L_2) \\ 1 - \omega^2(C_1 L_1 + C_2 L_2) - \omega^4 C_1 C_2(M_1^2 - L_1 L_2) & j\omega(L_2 + \omega^2 C_1(M_1^2 - L_1 L_2)) \end{bmatrix} \tag{3.57}$$

$$S_{21} = \frac{2}{A + \frac{B}{Z_0} + Z_0 C + D}$$

$$= \frac{j2\omega Z_0 M_1}{a + jb}$$

$$a = Z_0^2(1 - \omega^2(C_1 L_1 + C_2 L_2) - \omega^4 C_1 C_2(M_1^2 - L_1 L_2)) + \omega^2(M_1^2 - L_1 L_2)$$

$$b = \omega Z_0(\omega^2(M_1^2 - L_1 L_2)(C_1 + C_2) + L_1 + L_2) \tag{3.58}$$

where Z_0 is the characteristic impedance of the system. As it is expected the amount of transferred power can be altered by L_1, L_2 and M_1 at a certain frequency. The amount of coupling M_1 between two concentric single-turn circular coils is a function of physical

dimensions and the distance between them and can be calculated by (3.59) according to [52].

$$M_1 = \frac{2\mu\sqrt{R_1 R_2}}{m}[(1 - \frac{m^2}{2})k(m) - E(m)] \tag{3.59}$$

$$m = \sqrt{\frac{4R_1 R_2}{(R_1 + R_2)^2 + d^2}} \tag{3.60}$$

where R_1 and R_2 are the radii of the coils L_1 and L_2, respectively while μ is the permeability of the medium, and d is the distance between the coils centers. $K(m)$ and $E(m)$ are the Elliptic integrals of the first and second kind, respectively [52]. The solution of these Elliptical integrals can be approximated by (3.61) and (3.62) for small values of m [53], [54].

$$K(m) = \frac{\pi}{2} + \frac{\pi}{8}\frac{m^2}{1 - m^2} \tag{3.61}$$

$$E(m) = \frac{\pi}{2} + \frac{\pi}{8}m^2 \tag{3.62}$$

Equation (3.59) can be expanded for multi-turn coils with different windings radius as (3.63).

$$M_1 = \sum_{i=1}^{N_1}\sum_{j=1}^{N_2} \frac{2\mu\sqrt{R_{1i} R_{2j}}}{m_{ij}}[(1 - \frac{m_{ij}^2}{2})k(m_{ij}) - E(m_{ij})] \tag{3.63}$$

$$m_{ij} = \sqrt{\frac{4R_{1i} R_{2j}}{(R_{1i} + R_{2j})^2 + d^2}} \tag{3.64}$$

$$R_{1i} = R_1 + ia_1 \tag{3.65}$$

$$R_{2j} = R_2 + ja_2 \tag{3.66}$$

where N represents the coil winding number, R the smallest radius and a the spacing between the winding. The indices 1 and 2 represent coil 1 and 2, respectively. The effect of misalign-

ment between the two coils is investigated in [55], but for simplicity, it is assumed that the coils are perfectly aligned. When there is a significant size difference between coils (similar to the NFC and DuraPlug6 scenario), the amount of coupling M and the corresponding S_{21} is small. The issue is more severe when there is a large conductive asset in the system due to negative coupling and induced eddy currents. Following this, it will be proved that by using the proposed configuration in Fig. 3.19 (a) the amount of coupling and transferred power can be increased significantly under certain circumstances. The $ABCD$-matrix and S_{21} for the circuit shown in Fig. 3.19 (a) are obtained in (3.67) and (3.68) by assuming that this circuit is a series combination of circuit in Fig. 3.18 (b).

$$ABCD = ABCD_1 \times ABCD_2$$

$$= \frac{1}{j\omega M_1} \begin{bmatrix} j\omega(L_1 + \omega^2 C_3(M_1^2 - L_1 L_3)) & \omega^2(M_1^2 - L_1 L_3) \\ 1 - \omega^2(C_1 L_1 + C_3 L_3) - \omega^4 C_1 C_3(M_1^2 - L_1 L_3) & j\omega(L_3 + \omega^2 C_1(M_1^2 - L_1 L_3)) \end{bmatrix} \times$$

$$\frac{1}{j\omega M_2} \begin{bmatrix} j\omega(L_4 + \omega^2 C_2(M_2^2 - L_4 L_2)) & \omega^2(M_2^2 - L_4 L_2) \\ 1 - \omega^2(C_4 L_4 + C_2 L_2) - \omega^4 C_4 C_2(M_2^2 - L_4 L_2) & j\omega(L_2 + \omega^2 C_4(M_2^2 - L_4 L_2)) \end{bmatrix}$$

$$(3.67)$$

$$S_{21} = \frac{2}{A + \frac{B}{Z_0} + Z_0 C + D} = -\frac{2 M_1 M_2 Z_0}{Z_0(A_1 + j Z_0 B_1)} \qquad (3.68)$$

$$A_1 = \omega^4 [M_1^2 M_2^2 (-(C_1 + C_2)(C_3 + C4)) + M_1^2 L_2 L_4 (C_3 + C_4)(C_2 + C_1)$$

$$+ M_2^2 L_1 L_3 (C_3 + C_4)(C_2 + C_1) - L_2 L_4 (L_1 L_3 (C_2 C_4 + C_2 C_3 + C_1 C_3))]$$

$$+ \omega^2 [M_1^2 (-(C_3 L_4 + C_1 L2)) + M_2^2 (-(C_1 L_1 + C_2 L_2 + C_3 L_3 + C_4 L_4))$$

$$+ L_3 L_4 (C_4 L_1 + C_3 L_1 + C_3 L_2 + C_4 L_2) + C_1 L_4 + C_1 L_3]$$

45

$$+\omega[M_1^2(-(C_2L_2 + C_4L_4))] + (M_1^2 + M_2^2 - (L_1 + L_2)(L_3 + L_4)) \tag{3.69}$$

$$B_1 = \omega^5[(C_3 + C_4)C_1C_2(-M_1^2M_2^2 + M_1^2L_2L_4 + M_2^2L_1L_3 - L_1L_2L_3L_4)]$$

$$+\omega^3[M_1^2M_2^2(\frac{C_3 + C_4}{Z_0^2}) + M_1^2(-L_4(C_3 + C_4)(C_1 + \frac{2L_2}{Z_0^2}) - C_1C_2L_2)$$

$$+M_2^2(-L_3(C_3 + C_4)(C_2 + \frac{2L_1}{Z_0^2}) - C_1C_2L_1) + C_1L_1L_3(C_2L_2 + C_4L_4)$$

$$+C_2L_3L_4(C_1L_1 + C_2L_2) + C_2L_2L_4(C_1L_1 + C_3L_3) + \frac{L_1L_2L_3L_4}{Z_0^2}(C_3 + C_4)]$$

$$+\omega[M_1^2(C_1 + \frac{L_2}{Z_0^2}) + M_2^2(C_2 + \frac{L_1}{Z_0^2}) - L_4(C_1L_1 + C_2L_2 + C_3L_3) + \frac{L_1L_2}{Z_0^2}]$$

$$-L_3[C_1L_1 + C_2L_2 + C_4L_4 + \frac{L_1L_2}{Z_0^2}] + \omega^{-1}[L_3 + L_4] \tag{3.70}$$

Here, the NFC antenna is replaced by input port coil L_1 in both circuits while the HF RFID tag is replaced by the output port coil L_2 in Fig. 3.18 and Fig. 3.19. The idea is to show that the amount of transferred power is boosted significantly by applying the booster circuit that is replaced by the parallel combination of L_3, L_4, C_3, and C_4 in Fig. 3.19 (a). The block diagram of the proposed system is depicted in Fig. 3.19 (b).

Again this equation does not have an algebraic solution for the roots to obtain the sensitivity of the power transfer to each element.
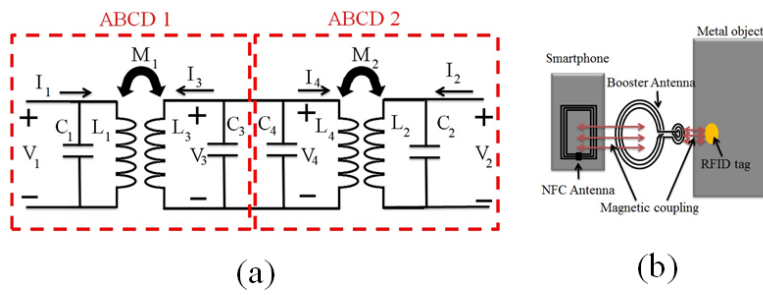
Figure 3.19: The proposed booster system (a) equivalent circuit and (b) block diagram.

Chapter 4

Modulator Based Sensor System

In this chapter, the modulator based sensor system is studied. In the proposed system, the antenna acts as the sensor and the main mechanism for communication. Different MUTS influence the antenna differently, resulting in different operational frequencies of LO that is loaded by the sensor antenna. The shift in frequency is then detected by a PFC in a simple, low cost and fast method. This chapter is organized as follows. The sensor antenna structure is investigated in the first section. Then the configuration of the modulator is discussed. The extraction of the sensing signal is studied further, and, finally, the experimental results are presented.

4.1 Sensor Structure

Recent investigations have shown that most RF/Microwave sensors require devices and equipment to monitor the frequency response of the sensor. The equipment required for frequency spectrum monitoring, such as vector network analyzer (VNA), spectrum analyzer (SA), and RF oscilloscope, are usually expensive, bulky and power consuming. In addition, the recorded responses should be post-processed for further detection and characterization of the material.

In this report, the conversion of the frequency response deviation around the free running

state in an RF/Microwave sensor system for sensing relative permittivity of materials in contact with the transmitter antenna is studied using a cost- and energy-effective way. The system is embedded into a conventional OOK modulator, which is compatible with UHF RFID systems. The sensing signal is directly converted to a voltage level correlated with the dielectric constant of material which can be used for re-tuning the circuit for operation at the specific frequency band, conversion to digital data, and transmission to a base station alongside to the communication data stream.

The architecture of the proposed frequency recovery RF/Microwave sensor system is depicted in Fig. 4.1. Sensing is provided by adding a sensitive region to the antenna structure. When the samples are placed on the sensing region, the input impedance characteristics of the antenna change. Since the sensor antenna loads a VCO via through-port of a coupler, the operating frequency alters accordingly. The through connection in a coupler transfers most of the power while some small portion of the signal is coupled to the coupled-port. This small portion is utilized to extract the sensing signal by comparing it to a fixed reference frequency. A PFC detects the instantaneous phase error between the sampled signal and reference where the output is voltage proportional to the error. The error-signal which is also the sensing signal can be converted to a digital data using an ADC and added to the communication data as well as being used to bring back the circuit to the initial operating state. As can be seen with this method, not only can the RF/Microwave sensing information be detected without using any expensive and high power consuming equipment such as VNA, but also no further post processing is required to extract the sensing information.

4.1.1 Sensor Antenna

The sensing part of the system is a parasitically loaded dipole antenna with unbalanced port as illustrated in Fig. 4.2 . An open loop resonator is placed in the proximity of the balanced feeding line where the samples are placed on top. The loop loads the antenna differently for different materials since the capacitance of the loop alters. Accordingly, the
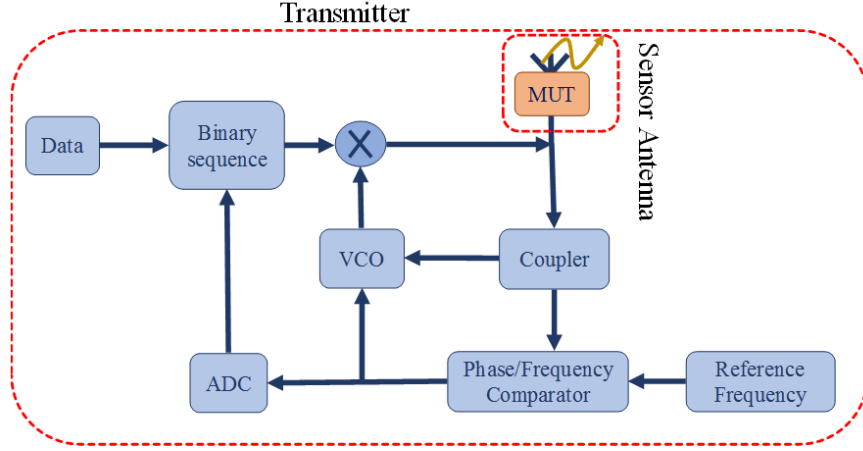
Figure 4.1: The system architecture of the proposed RF/Microwave sensor system.

resonant frequency and input impedance characteristics of the antenna changes. The samples are placed on the sensing region marked in Fig. 4.2. A balun for conversion of the balance-unbalance signals is directly connected to the balance twin-line feeding of sensor antenna. The balun structure consists of a 3 dB power divider in which one path, compared tp the other, has a 180° phase shift. Therefore, the signals arrive at the balance twin-line feeding with equal amplitude but 180° phase difference, which is desirable for feeding a dipole antenna. A quarter wave length microstrip transformer is also used for matching the input impedance to 50 Ω since the whole system works with this characteristic impedance.

The physical dimensions of the sensor antenna are presented in Table. 4.1. The power coupler is directly connected in between the sensor antenna and the rest of the circuit to sample a portion of the signal for extracting the sensing signal while the rest of the power is delivered to the sensor antenna for radiation. As can be seen in Fig. 4.2, the power coupler is a quarter wavelength meandered coupled where the VCO is connected to the input port, sensor antenna is connected to the through port, the coupled port is connected to the circuit for extracting the sensing signal, and the isolated port is matched to a 50 Ω. The simulation results of the input reflection coefficient and input impedance for the proposed sensor antenna with different samples between 850 MHz and 1 GHz are illustrated in Fig. 4.3. The dielectric
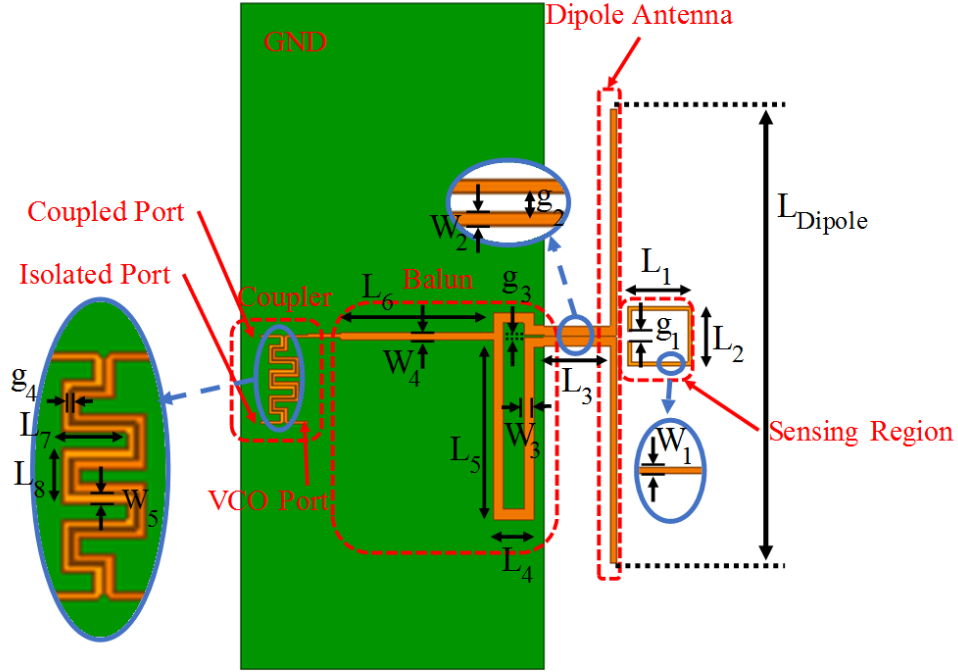
Figure 4.2: The proposed sensor antenna structure.

constant of samples varies between 1 and 12.85. As can be seen, by increasing the dielectric constant of MUTS, both real and imaginary parts of the input impedance shift toward lower frequencies due to the loading effect of samples and parasitically loaded open-loop section on the antenna. This results in lowering the resonant frequency of the antenna by increasing the dielectric constant. The current distribution of the proposed sensor antenna is depicted in Fig. 4.4. It can be seen that the current is properly distributed on the dipole arms where they should be 180° out of phase.

4.1.2 Modulator

The modulation technique utilized for communication is a special form of Amplitude Shift Keying (ASK) in which the amplitude of the output signal is either maximum or zero for 1 and 0 in the data stream. This is called On-Off Keying (OOK) and is widely used in

Table 4.1: Physical dimensions of the sensor antenna

Parameter	Length (mm)	Parameter	Length (mm)
L_1	19.3	L_2	18
L_3	20	L_4	12
L_5	54	L_6	46
L_7	7	L_8	5.7
L_{Dipole}	136.2	W_1	1.13
W_2	3	W_3	3
W_4	2.1	W_5	0.85
g_1	0.5	g_2	0.2
g_3	0.5	g_4	0.25

digital communications such as RFIDs and NFCs. For the realization of this modulation, the supply voltage of a local oscillator is switched on and off with correlation to the 1 and 0 in the data stream. The local oscillator is designed by a common base bipolar junction transistor (BJT) and a feedback circuit from the emitter to the base to provide the oscillation stability, as shown in Fig. 4.5. A general purpose BFP420 transistor is used with the bias point of V_{be}=0.87 V, I_C=21 mA and V_{ce}=2.23 V.The frequency of oscillation is tuned by using a variable capacitor which is connected to the base. A conventional varactor (SMV1232) biased by a control voltage (V_{ctrl}) provides this variable capacitor. For the tuning range of the varactor (0.7 pF to 4.15 pF), the designed VCO operates between 785 MHz and 1.285 GHz while V_{ctrl} is between 0 and 15 V. The simulation results for the operating states of the VCO for minimum, maximum, and desired values of the varactor capacitances are depicted in Fig. 4.6. The desired free running state of the circuit is at 915 MHz which is in the middle of the North American UHF RFID band.
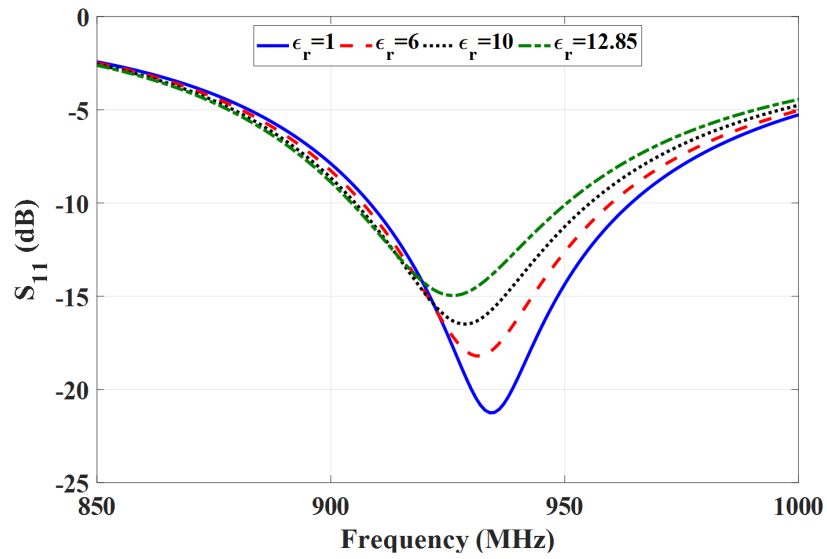
(a)
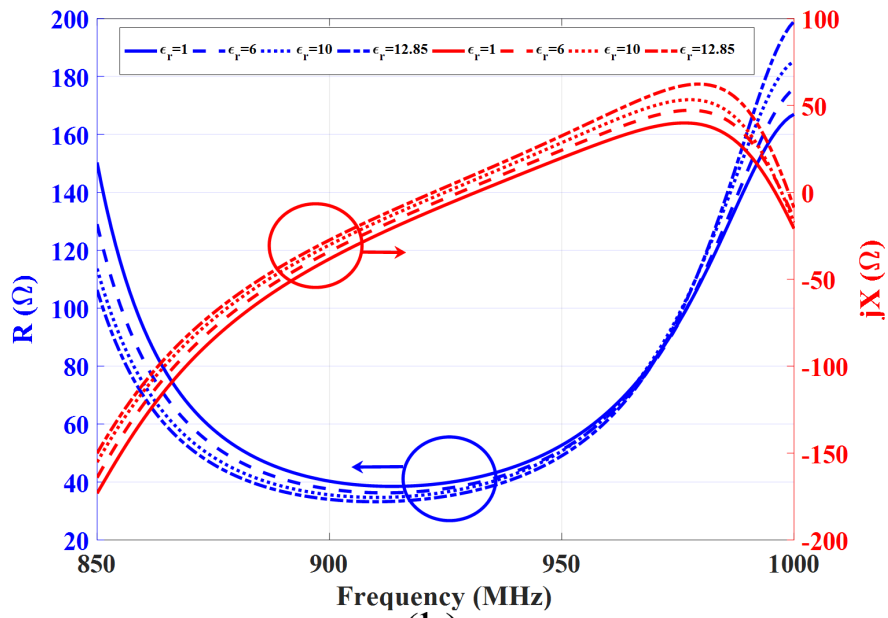
(b)

Figure 4.3: The simulation results for (a) input reflection coefficient and (b) the input impedance of the sensor antenna with different dielectric constants.
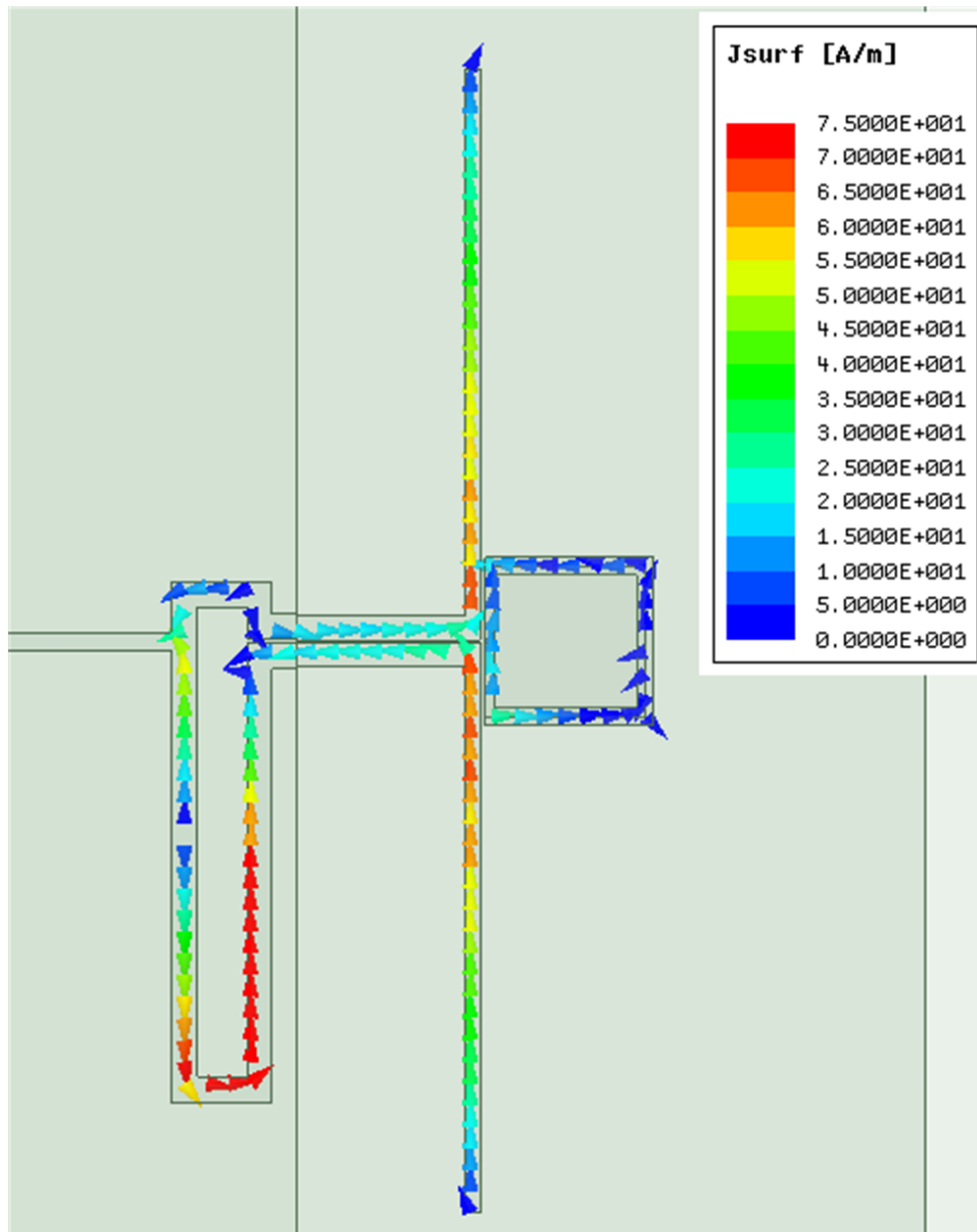
Figure 4.4: simulation results for the current distribution of the sensor antenna.
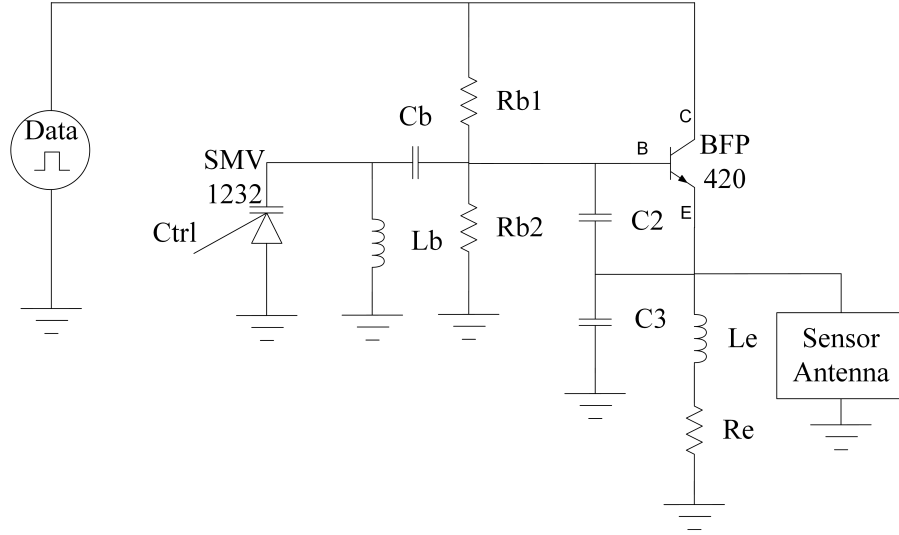
Figure 4.5: The circuitry of the local oscillator.
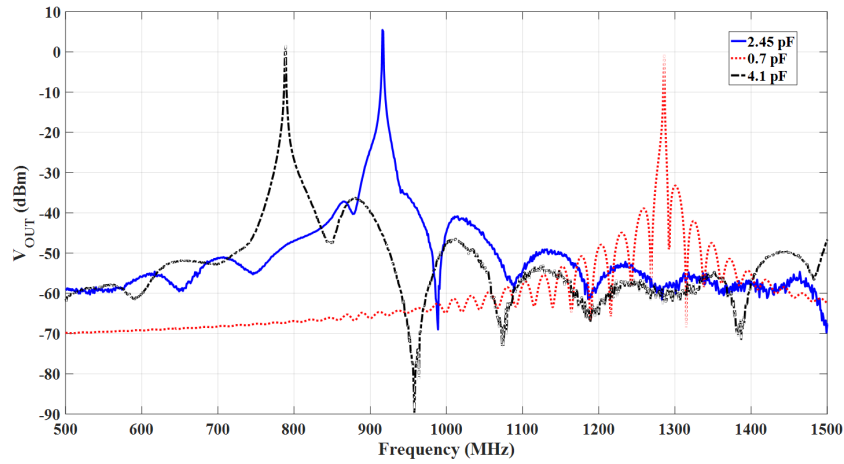
Figure 4.6: The simulation results of the free running state of the VCO and the tuning range.

4.1.3 Extraction of Sensing Signal

Different materials in contact with the sensor antenna affect its input impedance which directly loads the local oscillator, resulting in changes in the operating frequency of the system. Most of the conventional RF/Microwave systems use the changes in frequency for

detection but not many investigations have been done for recovering this frequency shift. Therefore, bulky, expensive, high power consuming equipment is required for the detection of frequency at the receiver and extraction of the sensing data. In this paper, for the extraction of the sensing data a separate path for the signal is considered in which a small portion of the signal feeding to the antenna by the modulator is sampled through a power coupler and then compared to a reference signal using a PFC. The output of PFC that is the error between the simultaneous phase of the sampled signal and the reference signal is proportional to the dielectric constant of MUT. This error signal can be utilized for recovering the frequency back to its original state as well as being recorded or even modulated alongside the communication data. The proposed system is shown in Fig. 4.7. The coupling factor should be small enough so as not to reduce the delivered power from the VCO to the sensor antenna. This is the power that should be radiated by the antenna as the communication signal. On the other hand, if the signal is too small, then it cannot be used for comparison since there is a threshold for power level at the PFC input port. The coupling factor is selected to be -14 dB so the output power is still high enough for the detection part and small enough not to influence the transmission. Fig. 4.8 shows the parameters of the utilized directional coupler for sampling the power and extraction of the sensing data. Considering the values for Isolation and Directivity of the coupler assures no unwanted reflected signal due to mismatches affects the performance of the system.

4.2 Experimental Results

As an evaluation of the proposed idea, a version of the modulator-based frequency recovery sensor system is fabricated on a 0.508 mm thick Rogers RO4003 substrate with $\epsilon_r = 3.55$ and $\tan \delta = 0.0027$ [57] operating at UHF RFID frequency band (902MHz-928 MHz). The samples used for the measurements are 20 mm $\times$ 20 mm $\times$ 0.75 mm solid low loss flat substrates made by Rogers Inc with dielectric constants ranging up to 12.85. The measurement results for the input reflection coefficient of the sensor antenna for different MUTS are presented in
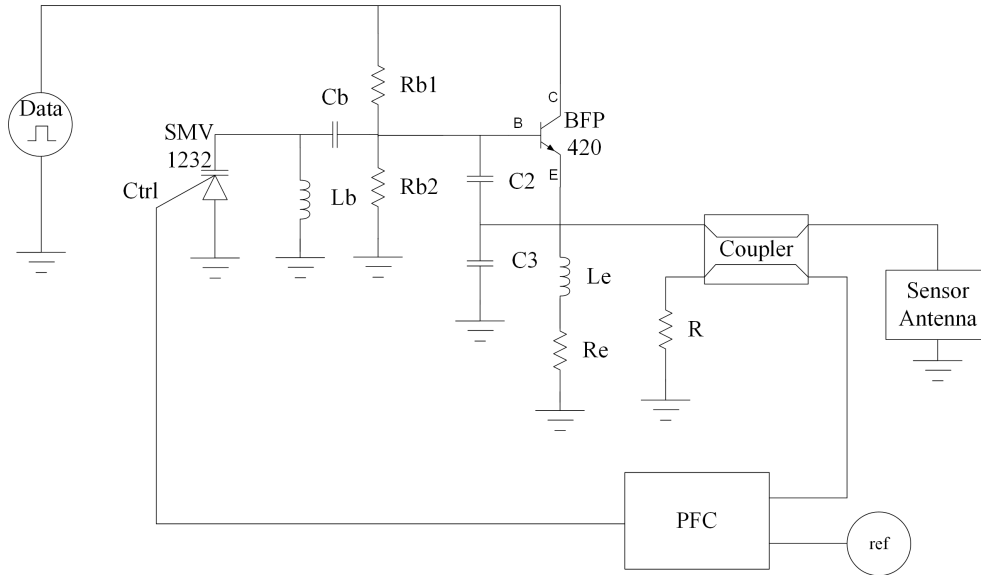
Figure 4.7: The proposed sensing data extraction system.
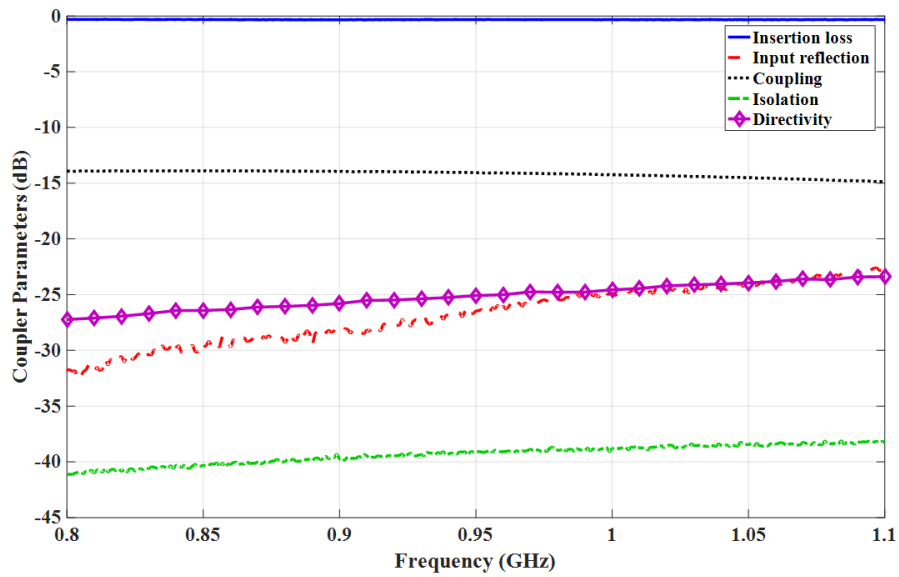
Figure 4.8: The parameters of the directional coupler.

Fig. 4.9. The results are obtained using an R&S©ZVA13 VNA after a full one-port calibration. As can be seen, by increasing the dielectric constant of the samples the deviation of the operating frequency from the free air running state increases.

57

In order to extract the frequency deviation caused by the sample's relative permittivity, an HMC439 PFC is used to find the error between the sampled signal from the modulator and the reference signal provided by an ADF4153 oscillator. The frequency of ADF4153 is set to the free running frequency of VCO when the sensor antenna is in free air (No sample). The proposed system that is under test inside a 60 cm × 60 cm × 60 cm chamber made of electromagnetic absorbers is depicted in Fig. 4.10. This chamber is used to suppress the noises and undesired signal at this frequency band.

As it was discussed before, the radiation characteristics of a sensor antenna are desired to be kept intact. Fig. 4.11 shows the radiation patterns of the sensor antenna while different samples are located on the sensing region. As can be seen, the patterns are very similar with negligible differences while all of them are very similar to ideal dipole radiation patterns.
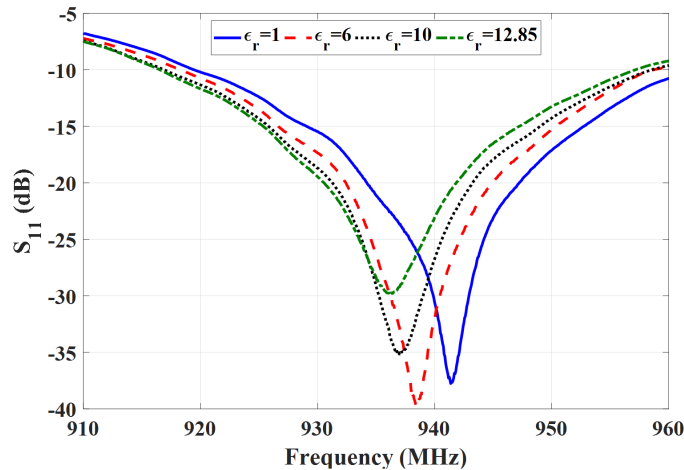
Figure 4.9: The Measurement results for the input reflection coefficient of the sensor antenna for different MUTS.

The parameter that describes the quality of the VCO output signal, is phase noise. Phase noise is the single sideband power within one Hertz bandwidth at a frequency f away from the carrier referenced to the carrier frequency power. The measurement results for the phase noise of the system for different MUTS are presented in Fig. 4.12. As can be seen, even for the worst phase noise, which is -70 dBc/Hz, the quality factor of the system is high and the
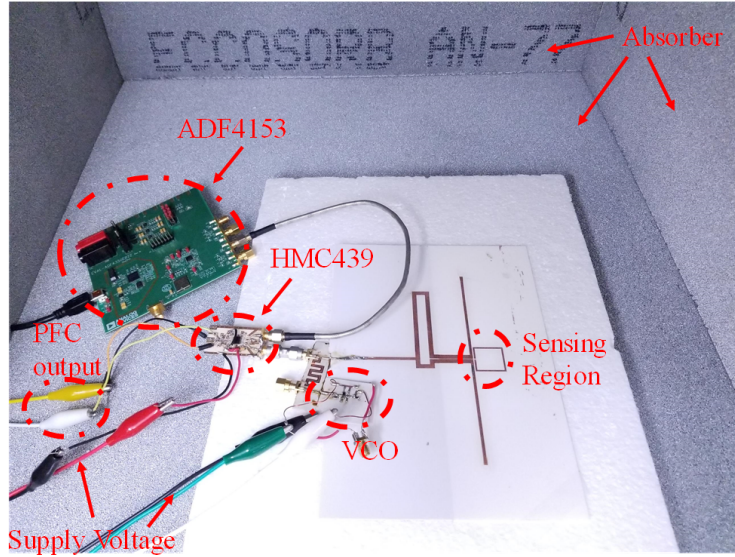
Figure 4.10: The proposed sensing data extraction system.

peak of the signal is distinguishable even with a few KHz shift.

The measurement results for the sensing performance of the modulator-based sensor system are presented in Table. 4.2. The frequency deviation of the system for dielectric constant ranging between 1 and 12.85 is 5.2 MHz at 930 MHz which is equivalent to 0.4 MHz shift per unit dielectric constant. The corresponding voltage change at the output of PFC and V_{ctrl} are 82 mV (6.4 mV change per unit dielectric constant) and 120 mV (9.3 mV change per unit dielectric constant), respectively. Although these numbers are not large, they are comparable to the results reported in the state-of-the-art RF sensor systems. These results are compared in detail in Table. 4.3.

The output voltage of PFC is measured for different samples and the control voltage is adjusted accordingly in order to compensate for the changes in the operating frequency. The summary of the system performance is provided in Table. 4.3. As can be seen, by increasing the dielectric constant from 1 to 12.85, the operating frequency of modulator reduces from 932.137 MHz to 926.932 MHz. Since the reference frequency is constant, the error between the reference and sampled signal increases; hence, the output voltage of PFC increases. This
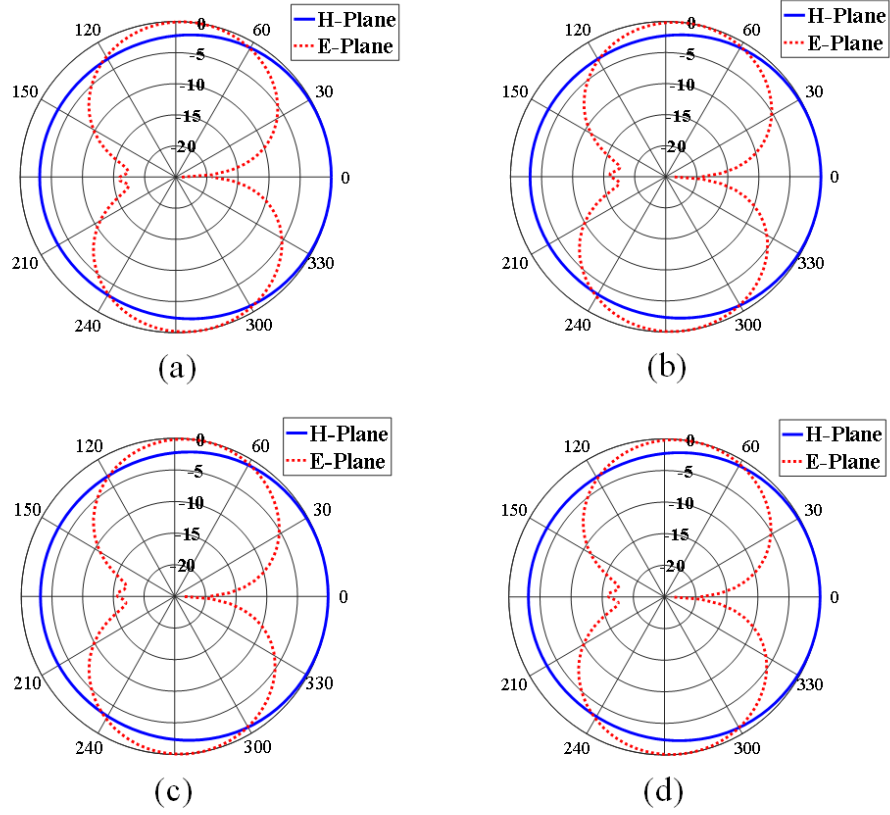
Figure 4.11: The Measurement results of the radiation patterns for (a) $\epsilon_r = 1$, (b) $\epsilon_r = 6$,(c) $\epsilon_r = 10$ and (d) $\epsilon_r = 12.85$.

Table 4.2: Summary of the circuit performance.

Sample ϵ_r	Resonance Frequency (MHz)	PFC Output Voltage (V)	Control Voltage (V)
1	932.137	0.996	2.57
6	928.582	1.076	2.63
10	927.467	1.077	2.66
12.85	926.932	1.078	2.69

signal is then used to obtain the required control voltage to re-tune the system for operating at the initial frequency. By increasing the control voltage, which is directly applied to the
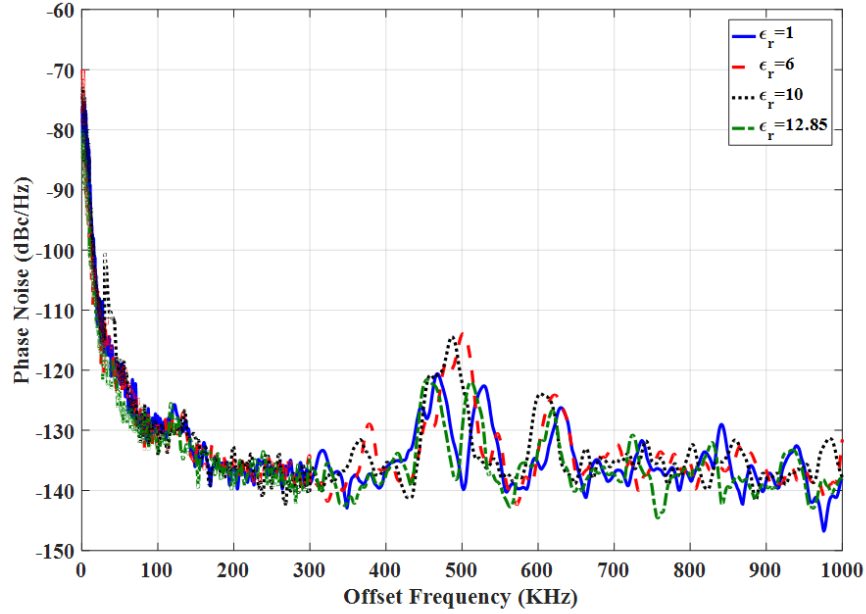
Figure 4.12: The measurement results for the phase noise of the system for different samples.

varactor controlling the operating frequency of LO, its capacitance decreases resulting in increasing the frequency of LO. The control voltage is proportional to the dielectric constant of MUTS as shown in Fig. 4.14.

A sensor node should be capable of sending data as well as sensing the desired parameter. As mentioned before, the proposed sensor system is capable of making OOK modulation by applying the data sequence to the bias voltage of VCO. Fig. 4.13 (a) shows the modulated signal (40 Kbps, 1011010001 stream as an example) in the time domain at the receiver antenna. The demodulated signal at the receiver and the detected bits from a conventional non-coherent envelope detector is illustrated in Fig. 4.13 (b), which is matched with the transmitted data. There is no error in the demodulated bits as the communication channel is isolated in a chamber and the link length is small (about 60 cm). The average error of the system which is $\pm 6.42\%$ can be defined as the average of the error between a linear approximation of ϵ_r versus V_{ctrl} and its actual value.

61
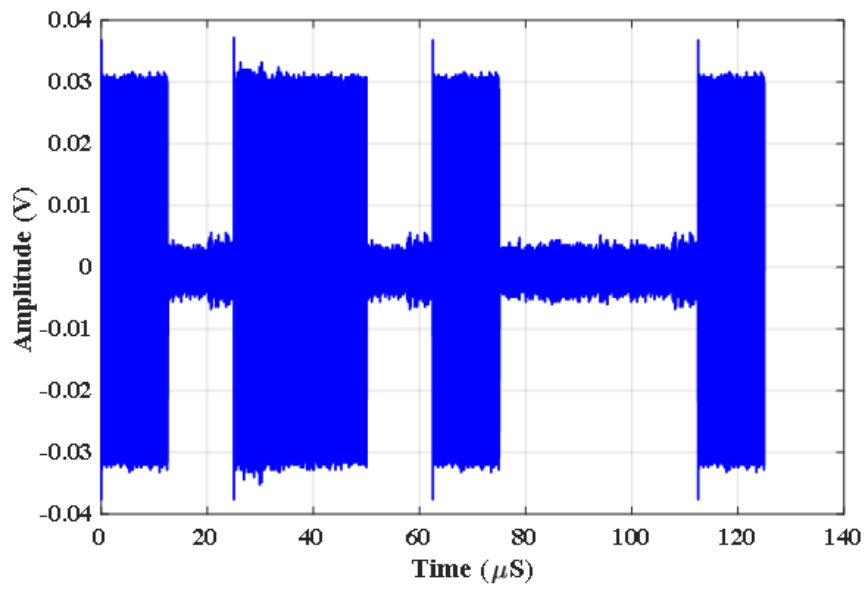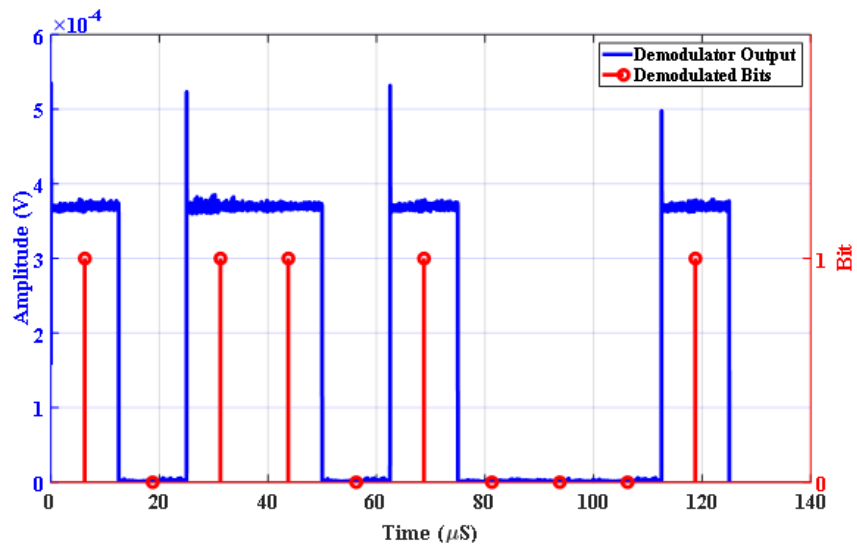
Figure 4.13: (a) Modulated signal in time domain and (b) demodulated signal and bits at the receiver.
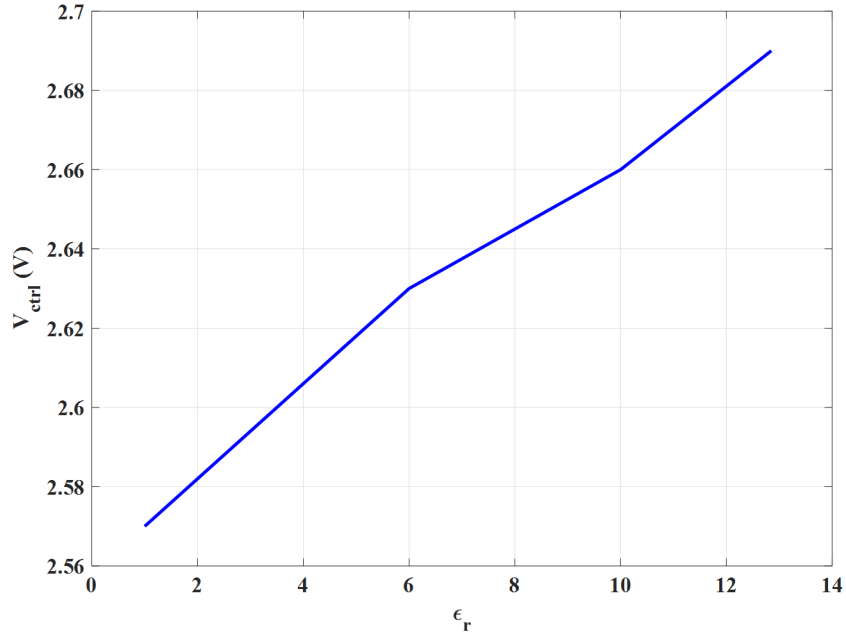
Figure 4.14: The relation between the measured V_{ctrl} and ϵ_r.

Table. 4.3 compares this work with the state-of-the-art RF dielectric sensors. As can be seen, this work has the highest sensing ratio (1:12.85) alongside [31], [32] and [58], while it is the only system capable of frequency recovery and data communication. It is worth mentioning that the error of the system is still comparable to other works.

Table 4.3: comparison with state of the art dielectric sensors

Reference	Range of Permittivity	Percent error	Sensitivity per unit Dielectric constant	Data Communication	Frequency Recovery
[29]	2.1-4.3	5%	NA	×	×
[30]	3.38-10.35	±2.5%	0.13 pF/m at 6 GHz	×	×
[31]	1-12.85	6.24%	0.42 MHz at 1 GHz	×	×
[32]	1-12.85	4%	0.46 MHz at 1 GHz	×	×
[33]	2.2-12.94	4.5%	0.001 ΔS_{21}	×	×
[42]	1-10.2	±3.6%	10 to 45 MHz at 7 GHz	×	×
[58]	1-12.85	±3.75%	2.5 MHz at 2.45 GHz	yes	×
[59]	2.55-9.5	16%	NA	×	×
[60]	5-16	±3.72%	1 MHz at 4 GHz	×	×
This Work	1-12.85	±6.42%	0.4 MHz at 930 MHz	yes	yes

In this Chapter, a practical and low-cost solution for extracting the sensing data in the

RF spectrum of RF/Microwave sensors is proposed. The system can convert the frequency shift in the frequency response of an RF/Microwave sensor (in this case a sensor antenna) to a voltage proportional to the frequency deviation. This signal can be further utilized to re-tune the circuit back to its original state as well as transmitting it to the receiver. It is also shown that the radiation characteristics of the sensor antenna for this application are not prone to the samples since it is parasitically loaded. Only the input impedance of the sensor antenna, which loads the local RF oscillator, alters for different dielectric constants. The proposed system is compatible with the convention modulators; therefore, the number of the components in the circuit does not change to support data modulation. Moreover, the power consumption of the system for sensing data detection does not increase. All in all, it can be a practical, low-cost, and fast solution as a product for RF/Microwave sensing systems.

Chapter 5

Demodulator Based Sensor System

In this chapter, the demodulator based sensor system is studied. In the proposed system, the antenna acts as the sensor and the main mechanism for communication. Different MUTS influence the antenna differently, resulting in different operational frequencies of LO that is loaded by the sensor antenna. The shift in the frequency is then detected by a zero-crossing detector at the receiver. This chapter is organized as follows. The sensor antenna structure is investigated in the first section. Then the configuration of the modulator is discussed. The extraction of the sensing signal is studied further, and, finally, the experimental results are presented.

5.1   Sensor Structure

Fig. 5.1 illustrates the system architecture of the proposed sensor system. In the transmitter, the MUT affects the resonance frequency of the sensor antenna which sets the carrier frequency by loading the VCO. The data are also mixed with the carrier and are transmitted by the sensor antenna. At the receiver, the received signal goes through two independent paths. One is a non-coherent envelope detector for data extraction. The other one is a zero-crossing counter for the purpose of carrier frequency recovery. The non-coherent envelope detector

consists of a squared section, a lowpass filter (LPF,) and a sampler for the demodulation of the data. This type of demodulation is suitable for amplitude modulations (AM) such as amplitude shift keying (ASK). A lot of communication systems, such as radio frequency identification (RFID) and near field communication (NFC), operate based on ASK.
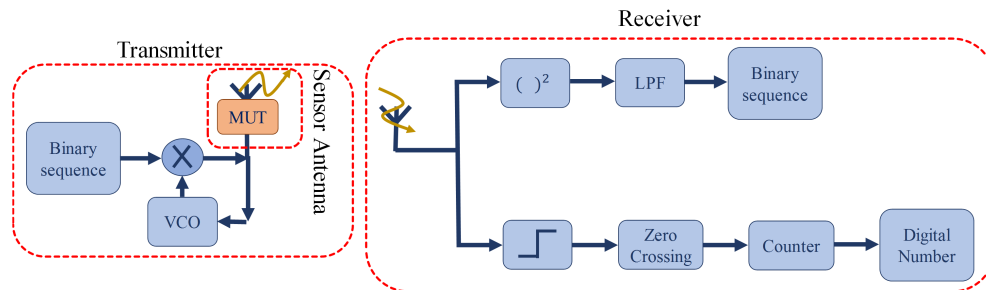
Figure 5.1: The architecture of the proposed wireless sensor system.
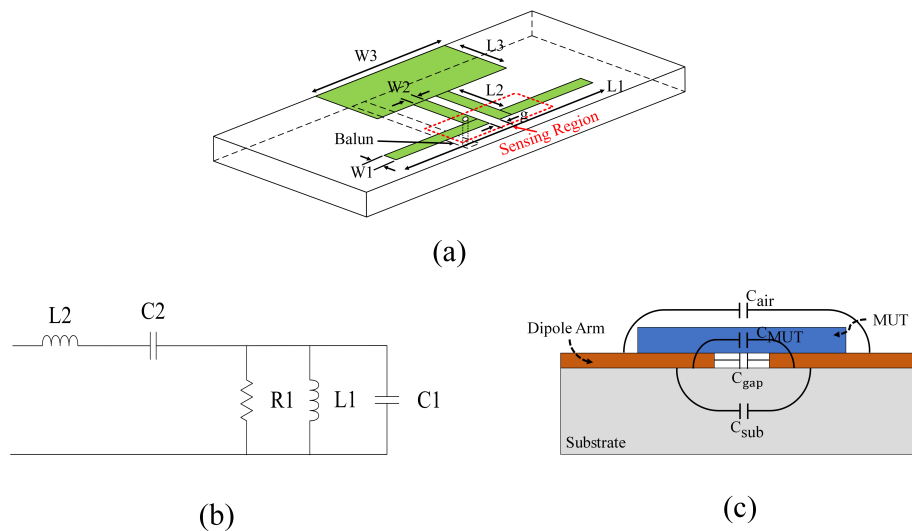
Figure 5.2: The dipole sensor antenna (a) the 3D structure, (b) equivalent circuit, and (c) side view and fringing capacitances.

Table 5.1: Physical dimensions of the dipole antenna

Parameter	Length (mm)	Parameter	Length (mm)
L_{dipole}	46.3	W_1	1
L_{feed}	11	W_2	1.1
L_{gnd}	10	W_3	25
g	0.3		

5.1.1 Sensor Antenna

The sensing part in the proposed sensor node is a dipole antenna which is used for the communication as well as detection of the material. Dipole antennas are usually chosen for different applications due to their desirable characteristics such as omnidirectional radiation pattern in E-Plane and less complexity for design and tuning. The MUTS are placed on the sensing region on top of the dipole antenna, as shown in Fig. 5.2 (a). This region is the most sensitive part of the dipole antenna for sensing the relative permittivity of a specimen since there are positive charges in one arm while the negative charges are accumulated in the other and the distance between them is minimum at this point. These are very critical in defining how capacitive the dipole antenna is [61]. A balun is also embedded in this antenna for appropriate adaptation between the balanced and unbalanced currents. The physical dimensions of the dipole antenna for the mentioned 2.45 GHz frequency band fabricated on RO4003 substrate with 0.508 mm thickness and $\epsilon_r = 3.55$ are presented in Table. 5.1.

The equivalent circuit of the dipole antenna is presented in Fig. 5.2 (b). The R_1, C_1, and L_1 elements form an RLC tank which characterizes the dipole around its resonance frequency while C_2 and L_2 are for very low frequency characterization and can be neglected for simplicity without affecting the accuracy around the resonance, as is the case in our application [56].

The Capacitor C_1 is a combination of all the capacitances formed around the dipole antenna due to the fringing and near fields of antenna defined in (5.1).

$$C_1 = C_{sub} + C_{gap} + C_{air} + C_{MUT} \tag{5.1}$$

where C_{sub}, C_{gap}, and C_{air} are constant capacitances due to the fringing fields in the substrate, in the gap between dipole arms, and in the air, respectively. C_{MUT} is the additional capacitance due to placing the MUT on the sensing region. Fig. 5.2 (c) shows the side view of the dipole antenna and MUT on top of it as well as capacitances. When an MUT is placed on the sensing region, C_{MUT} and the above-mentioned equivalent capacitance of the dipole antenna change; therefore, the resonant frequency of the antenna (f_0) changes as follow:

$$f_0 = \frac{1}{2\pi\sqrt{L_1 \times (C_{sub} + C_{gap} + C_{air} + C_{MUT})}} \tag{5.2}$$

where only C_{MUT} varies for different materials. The simulation results for the changes in the resonance frequency of sensor antenna and normalized values of C_1 with respect to the capacitance of antenna for air (C_0) are simulated and shown in Fig. 5.3. As it was expected, by increasing the dielectric constant of samples, C_1 increases; hence, the resonant frequency decreases.

C_{MUT} is also a function of the size and shape of MUTS. The effect of the thickness of the specimen is similar to the effect of relative permittivity on the resonance of the sensor antenna. As the sample becomes thicker, the capacitance of the antenna increases and, therefore, the resonance of the antenna is lowered. The simulation results of the resonance frequency of the sensor antenna versus the thickness of the samples from 0.2 mm to 1.5 mm for ϵ_r equal to 6 and 10.2 are presented in Fig. 5.4. The electric fields distribution inside the substrate and specimen for different values of dielectric constant are depicted in Fig. 5.5. It can be seen that by increasing the relative permittivity, the electric field is squeezed more into the region between the dipole arms. Having more field concentration in a higher dielectric constant can be seen as a higher capacitance for the antenna and results in a lower operating frequency as it can also be seen in Fig. 5.3.
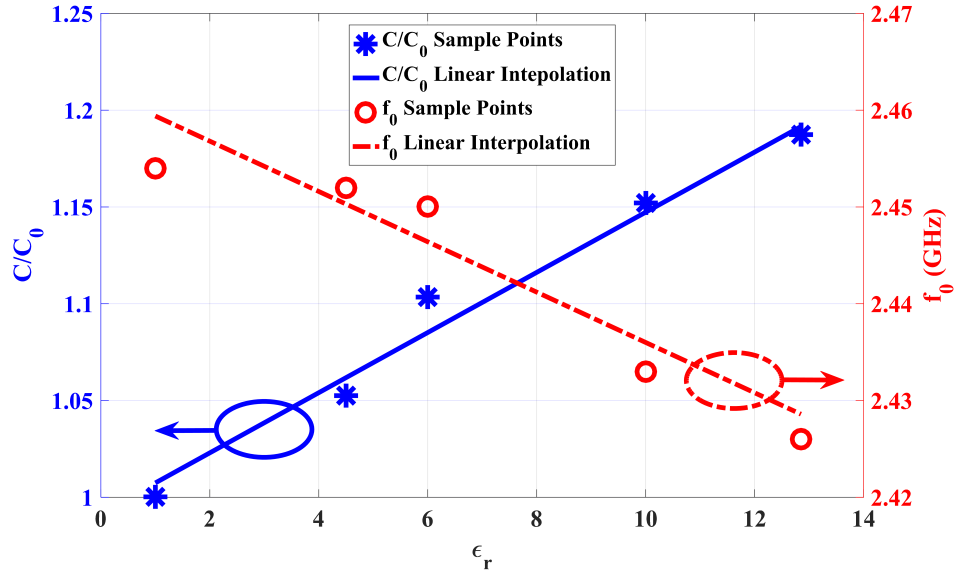
Figure 5.3: The Simulation results for the changes in the normalized capacitance of the antenna and its resonance frequency versus relative permittivity of specimen.

5.1.2 Voltage-Controlled-Oscillator

The input impedance of the sensor antenna changes with various MUTS due to the capacitance variations. This sensor antenna is connected to a VCO as a load where changes in the impedance of the load alter the frequency of VCO. The VCO provides the carrier frequency for data transmission. A common base BJT (BFP420 low noise transistor) architecture with a feedback path from the emitter to the base is selected for the stabilization of the oscillation criteria. The bias point of the transistor is V_{be}= 0.87 V, I_C= 8 mA, and V_{ce}= 1.4 V. The circuit configuration can be seen in Fig. 5.6. It is obvious that there are two sets of resonance tanks in this circuit. The first one is a fixed tank at the base of the transistor for providing a dominant resonance at the desired frequency and the other one is the antenna at the collector. Using the basic circuit theory, it is possible to bring the RLC equivalent circuit of the antenna from the collector into the base and analyze the effect of antenna parameters'

69
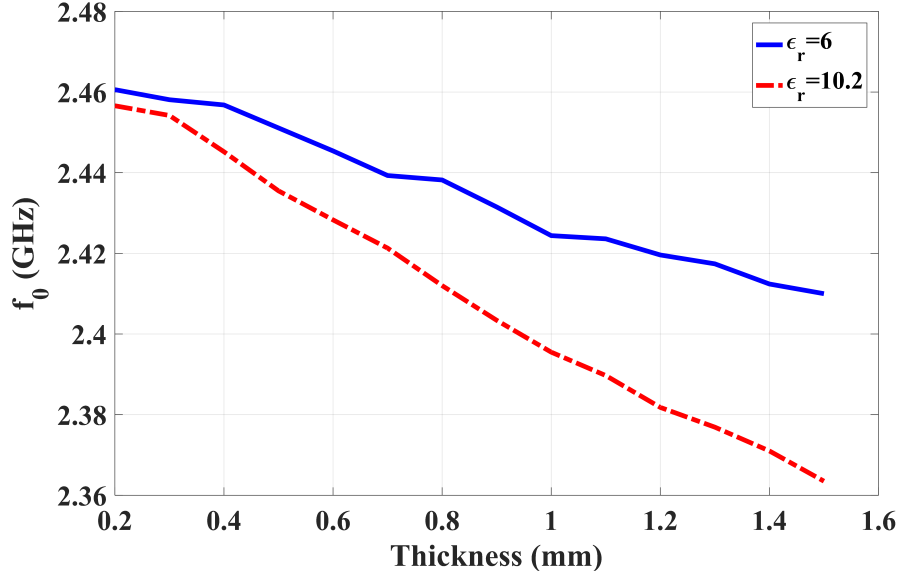
Figure 5.4: The simulation results for the changes in resonance frequency of sensor antenna versus thickness of the MUTS $\epsilon_r = 6$ and $\epsilon_r = 10.2$.

alteration, due to different MUTS, on the operation frequency of VCO. The circuit block diagram of Fig. 5.6 is presented in Fig. 5.7. If the Z-parameters of the transistor are presented by (5.3) [48] Chapter 4

$$Z_T = \begin{bmatrix} Z_{11} & Z_{12} \\ Z_{21} & Z_{22} \end{bmatrix} \tag{5.3}$$

the resonance condition of the circuit, shown in Fig. 5.7, can be explained by (5.4) [48] Chapter 6,

$$Imag\{Z_{in}||Z_B\} = 0 \tag{5.4}$$

in which Z_B is the impedance at base (the combination of LC tank and the Miller equivalent of the feedback capacitor both at the base) and Z_{in} is the input impedance seen from the

70
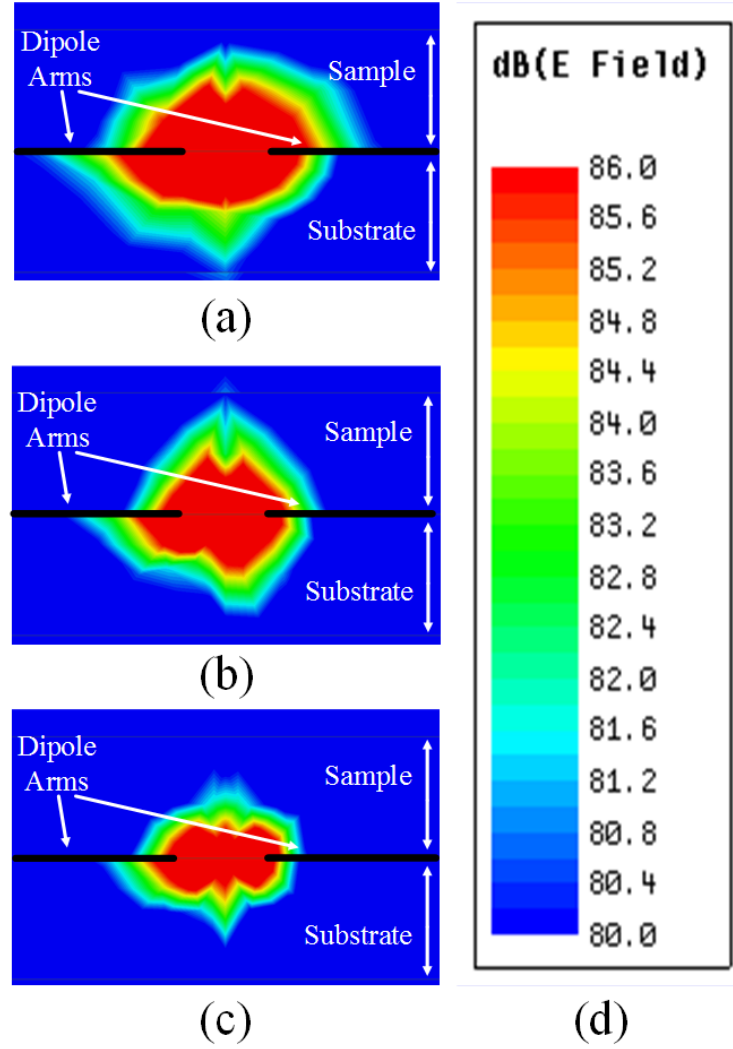
Figure 5.5: The side view of the electric field distribution in the system for different MUTS. (a) ϵ_r=1, (b) ϵ_r=6, (c) ϵ_r=12.85 and (d) the scale.

base (including the effect of transistor, antenna, and feedback capacitors at the emitter) and can be written as

$$Z_{in} = \frac{Z_{11}Z_{22} + Z_{11}Z_A - Z_{12}Z_{21} + Z_E(Z_{11} + Z_{22} - Z_{12} - Z_{21} + Z_A)}{Z_{22} + Z_A + Z_E} \tag{5.5}$$

where Z_A and Z_E are the impedances of antenna and emitter elements, respectively. It can be seen that for various MUTS, the capacitance of Z_A changes significantly.
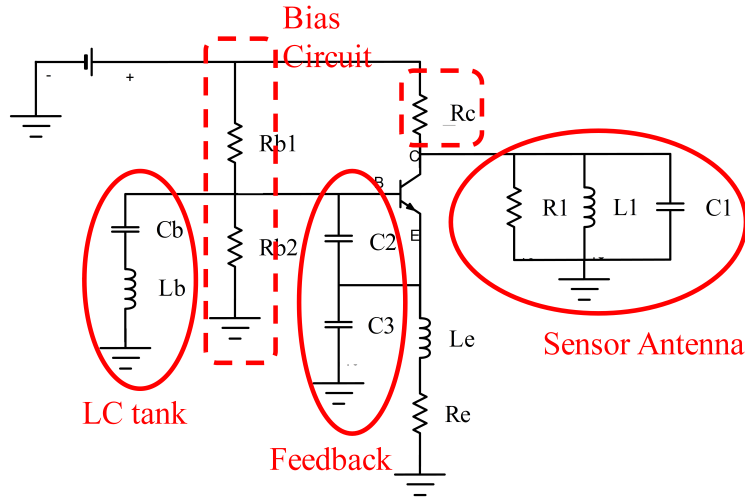
Figure 5.6: The VCO circuit schematic.

The OOK is selected for data transmission as a special case of ASK modulation, which is compatible with RFID and NFC standards. Hence, the time domain signal can be explained as

$$s(t) = \sum_{m=1}^{M} A_m rect(t/m - mT)cos(\omega t + \phi) \tag{5.6}$$

$$A_m \in [0, 1] \; for \; m \leq 1, 2, ...$$

where $rect$ is the rectangular pulse shape, T is the duration of bit pulses, M is the length
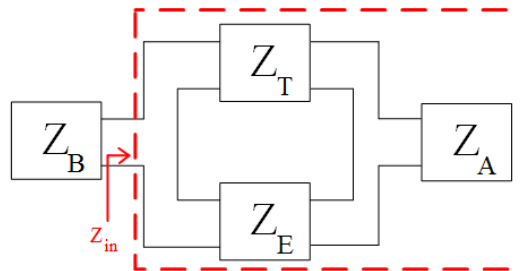
Figure 5.7: The block diagram of the system.

72

of bit stream, ω is the radial frequency of the carrier, and ϕ is the instant phase of the transmitted signal [62].

5.1.3 Receiver

In the receiver section for the carrier frequency recovery, the received signal is passed through a limiter block in which the signal is divided into three levels. If the signal is higher than the positive threshold, the output is +1; and if the signal is lower than the negative threshold, the output is -1 and the output is 0 for others. Then, a zero crossing detector sends a pulse to a counter whenever the signal changes its sign. The counter counts the number of crossings, which is proportional to twice the carrier frequency; therefore, the frequency of the carrier can be extracted from a specified counting time. This digital number, which is proportional to the frequency of the carrier, is proportional to the dielectric constant of MUT, as shown in Fig. 5.3. Besides, a non-coherent envelope detector is used for data demodulation. A second-order circuit asynchronously down-converts the received signal to the baseband domain, and an LPF omits the noise and undesired signals. Proper sampling can extract the data stream for further digital processing.

5.2 Experimental Results

As an evaluation of the proposed WSN node, the dipole sensor antenna and VCO are fabricated on a 0.508 mm thick Rogers RO4003 substrate with $\epsilon_r = 3.55$ and $\tan\delta = 0.0027$ [57]. The fabricated sensor node is shown in Fig. 5.8. The whole node can be fabricated on the same board. However, the VCO and antenna were implemented separately for initial test and calibration and then connected together by a male-to-male SMA Adapter.

The measurement results of the input reflection coefficient (S_{11}) of the dipole sensor antenna are illustrated in Fig. 5.9. The MUTS are selected from a wide range of dielectric constants. In addition to the initial state of air, we have four 20 mm $\times$ 20 mm samples of
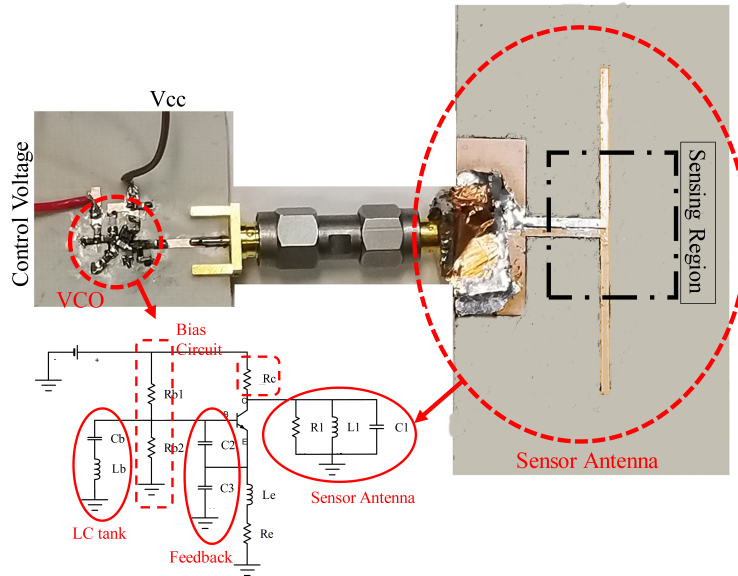
Figure 5.8: The fabricated WSN on RO4003 laminate substrate.
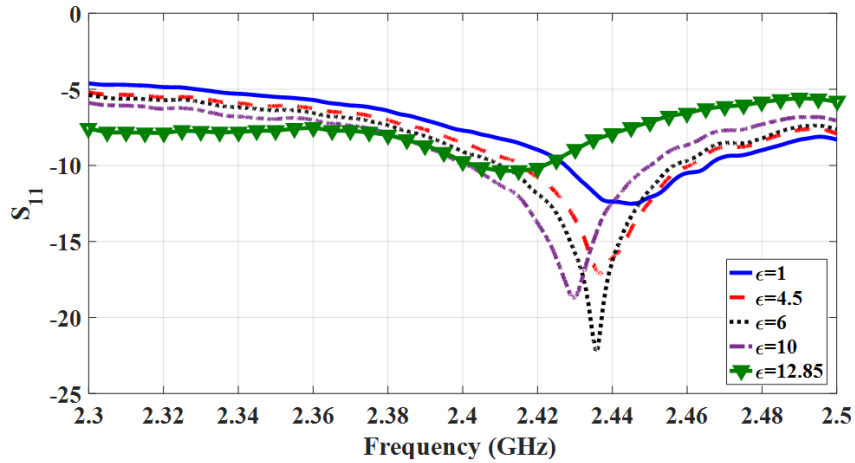
Figure 5.9: The measurement results of the sensor antenna input reflection coefficient versus frequency for different MUTS.

Rogers' substrates with relative permittivities of 4.5, 6, 10.2, and 12.85 (all samples are 0.51 mm thick except the last one which is 1.27 mm thick). The size and shape of samples are kept the same; therefore, the only parameter that can affect the results is the permittivity

of MUTS. As can be seen in Fig. 5.9, increasing the permittivity of the sample shifts the resonance of the antenna toward lower frequencies. For the utilized antenna and MUTS, the capacitance of antenna increases up to 20% for $\epsilon_r = 12.85$ compared to air and the resonance frequency decreases from 2.447 GHz to 2.415 GHz, as can be seen in Fig. 5.10. The advantage of selecting the sensing region (between arms of the dipole) is to have a minimum effect on the radiation characteristic of the antenna by changing the MUT. In this case, the gain of the dipole varies only between 2.1 and 2.2 dBi by varying the MUT dielectric constant between 1 and 12.85.
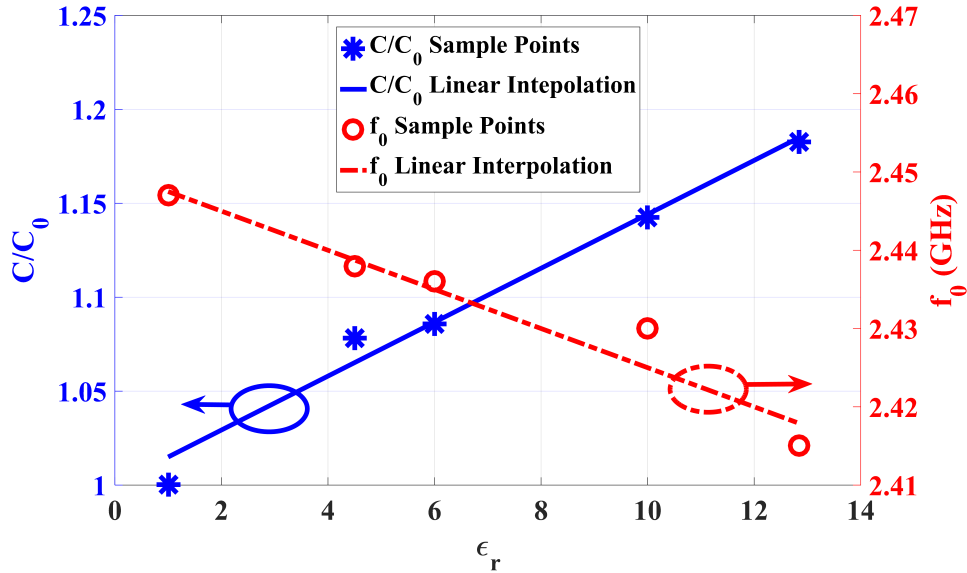
Figure 5.10: The measurement results for the changes in the normalized capacitance of the antenna and its resonance frequency versus relative permittivity of specimen.

Fig. 5.11 shows the measurement setup. The dipole sensor antenna is connected to the transmitter VCO as the load while different MUTS are placed on it. The OOK modulation is realized by connecting the DC supply voltage of the VCO to the bit sequence generator. The Digital signal source in Fig.5.11 generates a rectangular pulse shape with 30 KHz frequency and 0 to 3.3 V peak to peak voltage as a simple 0101 stream for data communication
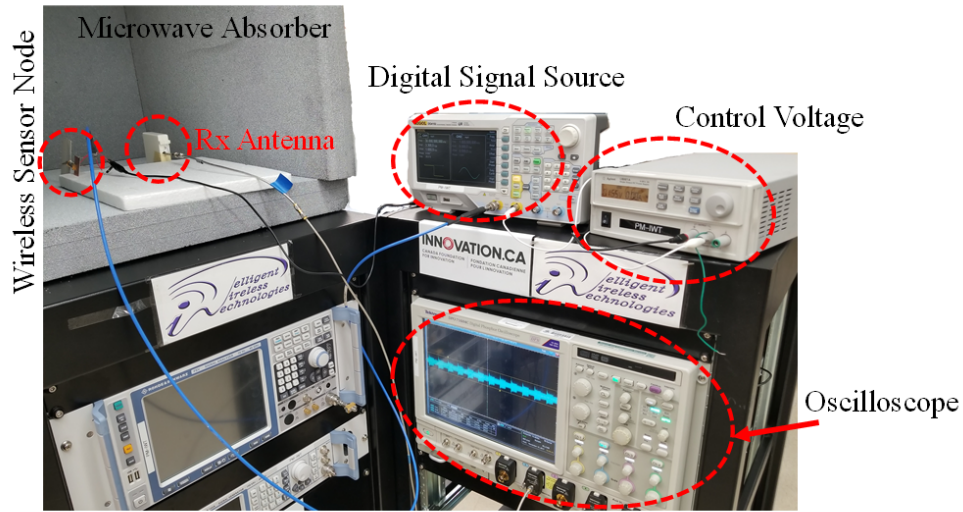
Figure 5.11: The measurement setup.
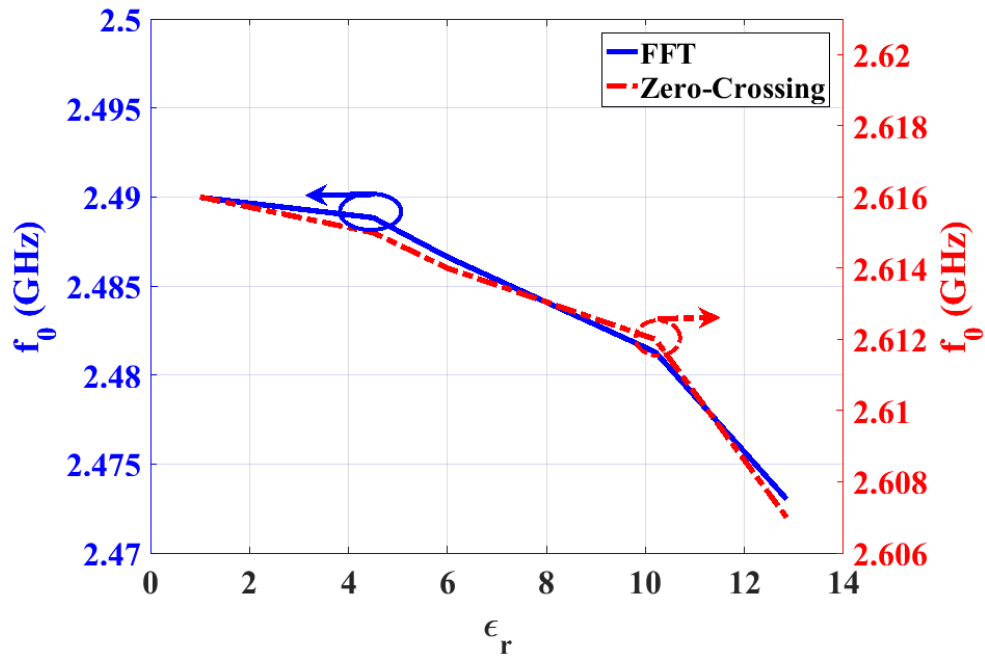
Figure 5.12: The comparison of the received carrier frequency versus relative permittivity of MUTS using FFT and Zero-Crossing methods
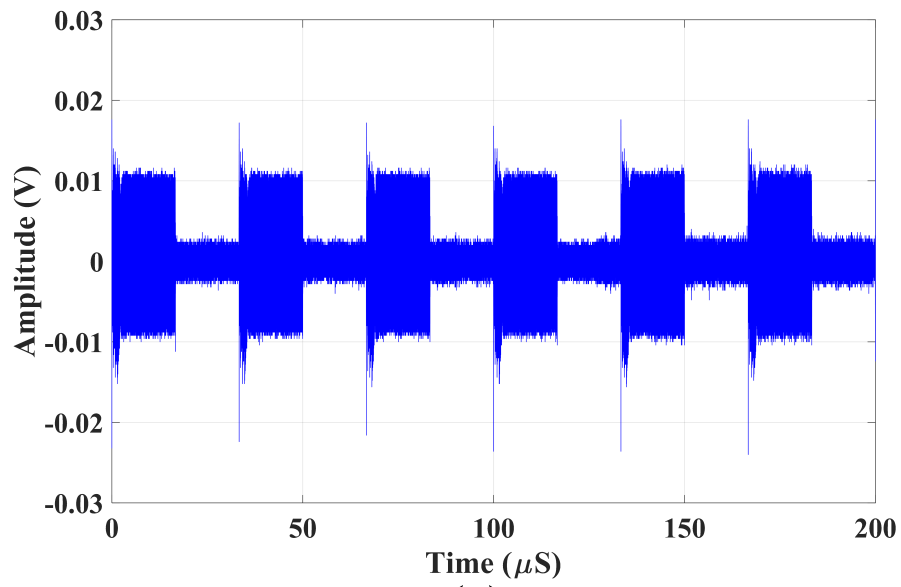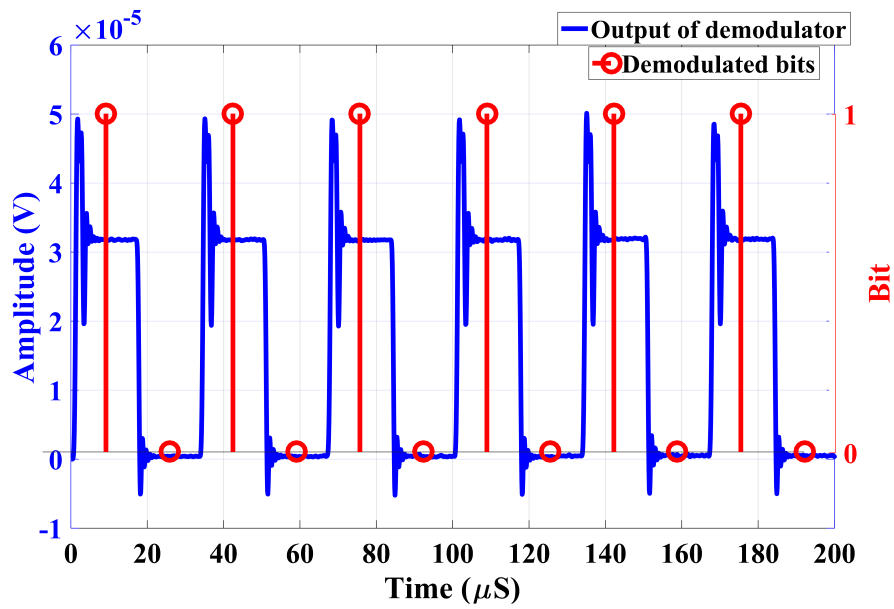
Figure 5.13: The (a) time domain and (b) demodulated waveform of the received signal for $\epsilon_r=1$ using non-coherent envelope detector and the recovered bit stream

evaluation. The distance between the transmitter and the receiver is 50 cm.

The transmitted signal is received by a standard patch antenna at 2.45 GHz which is connected to a Tektronix DPO71604C digital oscilloscopes and a direct-conversion receiver at 100Gs/S sampling rate. These digitized signals are then processed by the mentioned receiver architecture which is implemented in Simulink/Matlab. The outputs of the receiver are digital numbers proportional to the dielectric constant of MUT.

The frequency of the received signal can be determined by fast Fourier transformation (FFT) or zero-crossing detection. Using a zero-crossing detector, the number of times the signal changes its sign is counted; this is proportional to the frequency of the signal over a time unit. For different MUTS, this number is different since the frequency of the carrier and, hence, the number of zero-crossings depend on the relative permittivity of the samples. The calculated results from the measurements using zero-crossing detection and FFT for different dielectric constant MUTS are presented in Fig. 5.12. It is expected that FFT provides more accurate results, but it needs more resources for implementation and has more power consumption compared to the zero-crossing. As can be seen in Fig. 5.12, the trends of the two curves perfectly match but there is an offset error (almost 100 MHz) between the two methods.

The received signal is also demodulated using the non-coherent envelope detector. The received down-converted signals and the demodulated bits for MUT_{air}, as an example, are depicted in Fig. 5.13. (a) and (b), respectively. As can be seen, the transmitted 0101 stream is demodulated correctly at the receiver. It is obvious that the communication system based on OOK modulation, which is compatible with the RFID system, is now capable of sensing materials at RF frequencies while keeping the number of components, complexity, and power consumption unchanged. Being able to correlate each material with a digital number at the receiver without using a spectrum monitoring technique is another advantage over conventional RF material sensing. Table. 5.2 compares the experimental results of this work to the state of the art dielectric sensors from sensitivity range, error, ability to sense remotely, and capability to transmit independent digital data aspects. As can be seen, this work, [31], and [32] have the highest dielectric constant measurement range (1 to 12.85)

Table 5.2: comparison with state of the art dielectric sensors

Reference	Range of Permittivity	Percent error	Sensitivity per unit Dielectric constant	Remote	Data Communication
[29]	2.1-4.3	5%	NA	×	×
[30]	3.38-10.35	±2.5%	0.13 pF/m at 6 GHz	×	×
[31]	1-12.85	6.24%	0.42 MHz at 1 GHz	×	×
[32]	1-12.85	4%	0.46 MHz at 1 GHz	×	×
[33]	2.2-12.94	4.5%	0.001 ΔS_{21}	×	×
[42]	1-10.2	±3.6%	10 to 45 MHz at 7 GHz	yes	×
[59]	2.55-9.5	16%	NA	×	×
[60]	5-16	±3.72%	1 MHz at 4 GHz	yes	×
This Work	1-12.85	±3.75%	2.5 MHz at 2.45 GHz	yes	yes

although this work has the lowest error amongst them. Moreover, only this work, [42] and [60] can remotely sense and measure the dielectric constant although only this work is capable of digital communications amongst all these studies.

In this Chapter, a novel wireless sensor node is proposed. It is able to characterize the relative permittivity of a material under test by its antenna, in addition to the conventional communication duties of a WSN. By using a proper antenna and selection of a suitable sensing region, the antenna performance does not significantly change while the frequency of transmitted signal changes in accordance with the MUTS. Material detection is done at the receiver without influence on the demodulated data, using a combination of the noncoherent demodulator and zero-cross counting. The resulted digital number is correlated to the monitored MUT. This type of material characterization is very desirable and more practical compared to the other RF/Microwave methods in which the frequency spectrum of a signal is monitored with additional equipment. It should be noted that the proposed material detection and data communication system keeps the complexity and power consumption the same as the conventional wireless communication nodes. Adding the sensing capability to the communication system, without increasing the number of components and equipment, keeps the size, price and power consumption intact. Moreover, it is compatible with RFID and NFC communication standards and can be used in RFID- or NFC- sensor systems.

Chapter 6

Metal Proximity Near-Field-Communication System

Near-Field Communication (NFC) can be defined as a set of protocols for enabling an electronic device to communicate in short range [63], [64]. NFC-enabled equipment employs electromagnetic induction between coils or loop antennas at the globally available unlicensed ISM band of 13.56 MHz [65], [66]. The various applications for NFC can be categorized into three main fields: I) Service Initiation, II) Peer-to-Peer, and III) Payment and Ticketing according to [64]. Reading high-frequency radio frequency identification technology (HF RFID) tags is one of the most important applications provided by NFC-enabled devices since the operational frequency and mechanism (magnetic coupling) are similar [67], [68]. Nowadays, NFC enabled devices cover RFID standards including ISO/IEC 14443 and FeliCa [69], [70]. Reading an HF RFID tag embedded in a metal object is really challenging using NFC readers. It is due to the fact that the NFC reader, especially those used in smartphones, are relatively low power compared to the conventional RFID readers (50 mW compared to 4 W) [71]. The scenario is more severe when the size of the RFID tag is significantly smaller than the NFC coil. It is due to the lower coupling and induced current (eddy current) in the metal objects. Ideally, the magnitude of this current is equal to the source current but with

the opposite direction if the source current is aligned with the metal surface. If the source is in the proximity of the metal surface, the image current is also closer to the surface resulting in lower coupling or radiation efficiency [72]. The image current would also diminish the inductance of a coil close to metal object because of the negative mutual inductance [73]. Nowadays, lots of physically small metal mountable RFID tags are commercially available. In this paper, a DuraPlug 6 that is a metal-embeddable HF RFID tag made by InfoChip Company is utilized. This RFID tag operates under ISO/IEC 15693 standard. The read range of this tag is up to 2 mm with commercial RFID readers while its diameter is 6 mm. It can be inserted into a metal cavity while its top surface is 0.2 mm lower than the metal top surface and used for oil and gas industries. Fig. 6.1 shows the physical dimensions of this tag and in-metal implemented versions. Considering this, it is impossible to read this type of RFID tags with NFC-enabled smartphones because of the low output power and huge difference between the RFID and reader antenna size. Thus, having a passive device that increases the read range and enables smartphones to read metal mounted HF RFIDs is tempting. In this chapter, a passive booster circuit for Near-Field Communication (NFC) enabled smartphone is designed in order to increase the read range of metal mounted HF RFID. The same concept can be utilized to communicate with in-body implemented sensor tags, chipless RFIDs, and proximity range read/write sensor devices [74]- [77]. Firstly, the mathematical proof of concept is discussed. Then, the simulation and measurement results are studied and the properties of the proposed booster circuit are presented.

6.1   Design of the Passive Booster

As explained in Background Theory, the power transfer function does not have an algebraic solution for the roots and it is not possible to find a general expression for the effect of each element on the total transferred power. For the proof of concept, certain values are assumed for the elements substituted in for NFC antenna and RFID tag. The dimension of each coil is proportional to the size of the device it represents. Therefore, L_1 and L_2 are chosen to be
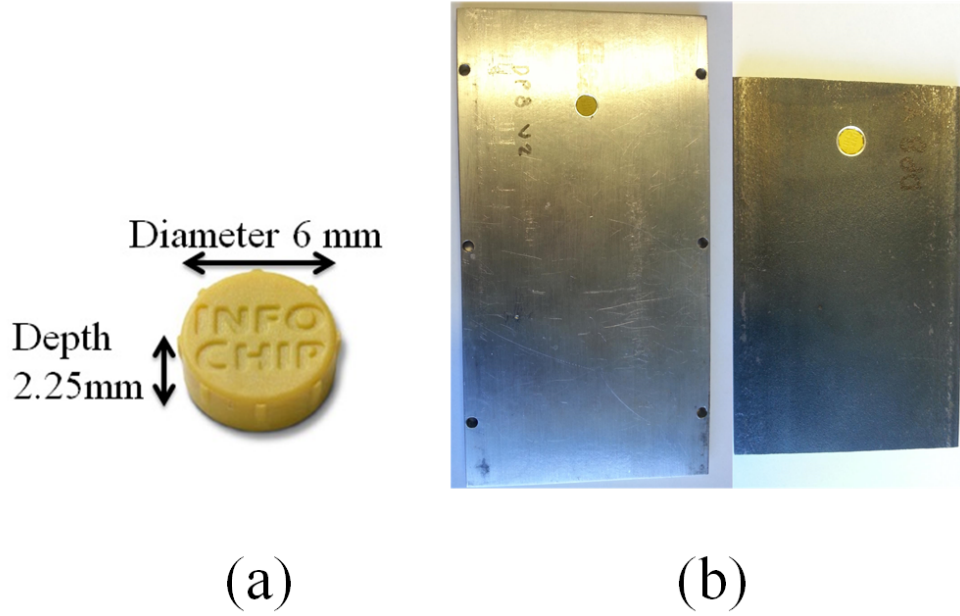
Figure 6.1: (a) The Physical dimensions of DuraPlug 6 HF RFID tag. (b) DuraPlug 6 embedded in metal plates.

35 mm and 3 mm in diameter, respectively. Equation (6.1) is an alternative for calculating the inductance of a circular planar spiral coil [78].

$$L = \frac{(0.5Nd_{avg})^2}{4d_{avg} + 11(R_o - R_i)} \tag{6.1}$$

where N is the number of turns, and d_{avg} is the average of the inner (R_i) and outer radius (R_o) of the coil [78]. The summary of the utilized parameters for L_1 and L_2 designed based on the latter method is represented in Table 6.1. The calculations show -50 dB for S_{21} when the parameters in Table 6.1 are used for circuit in Fig. 3.18 (b) at the resonance frequency. As it was discussed before, the more physical dimensions of the two coils are similar, the more is the coupling between them. Hence, for boosting the transferred power, which is proportional to $|S_{21}|^2$, the discussed circuit in Fig. 3.19 (a) is designed with physical parameters close to L_1 and L_2. The physical parameters of L_3 and L_4 are gathered in Table 6.2. By adding

82

the booster with these values into the system, the amount of the transferred power increases to -20 dB at the resonance frequency. The analytical results of S_{21} for both cases with and without booster are illustrated in Fig. 6.2. In both cases, C_i is chosen to have a resonance condition at 13.56 MHz. There is a 30-dB boost in all frequency by utilizing the booster. The problem is more challenging for transferred power when the system operates in the proximity of a finite size metal object. The equivalent circuit of the system operating near a metal asset is depicted in Fig. 6.3 (a) and (b) for both cases without and with the booster, respectively. The effect of the metal asset can be replaced by adding capacitance into the circuit. Therefore, a zero is added to the transfer function of the system between input and output ports. Depending on the value of this capacitance (the series combination of C_{M1} and C_{M2} in Fig. 6.3 (a)), the amount of transferred power can be altered. The analytical results for the transferred power of the circuits, shown in Fig. 6.3 (a) and (b) for different values of series capacitance, are illustrated in Fig. 6.4 (a) and (b), respectively.

Table 6.1: The summary of the physical properties for the utilized coil representing the NFC and HF RFID tag.

Inductor	L_1	L_2
Value (μH)	10	1
Winding thickness (mm)	0.6	0.16
Gap between windings	0.6	0.14
Number of turns	10	8
Outer radius (mm)	35	3

As can be seen for the same value of zero appearing in the transfer function due to the metal effect, the amount of transferred power still has a 30-dB-boost when the booster is utilized. These results show the most severe cases when the zero appears around the operational frequency. This zero is strongly related to the parasitic capacitance between coils and the metal object. The value of this capacitance is dependent to the physical dimensions of the system such as the area of coils and the distance between coils and metallic asset.

Table 6.2: The summary of the physical properties for the utilized L_3 and L_4.

Inductor	L_3	L_4
Value (μH)	25	1
Winding thickness (mm)	0.25	0.2
Gap between windings	0.25	0.15
Number of turns	20	16
Outer radius (mm)	19.3	3.1
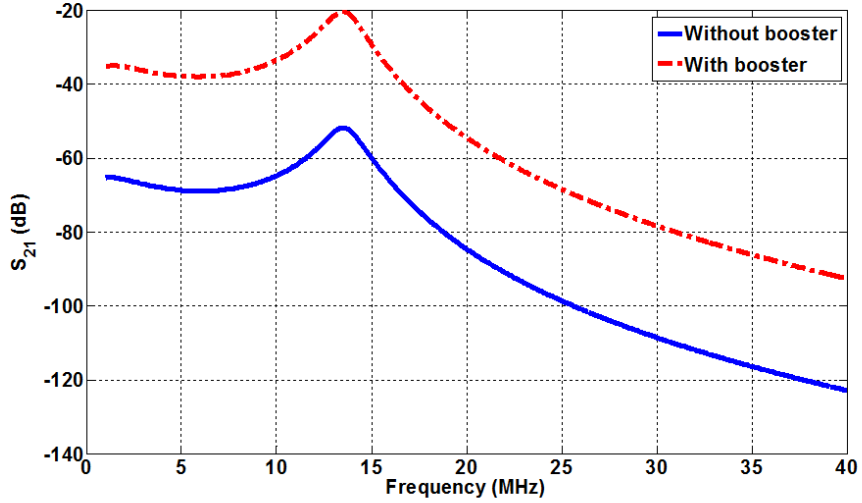
Figure 6.2: The analytical results of S_{21} for circuits with and without booster.

Since all dimensions are fixed after fabrication except for the distances to the metal object, it can be claimed that the value of zero is altered by these distances. For designing the booster circuit, a 25 μm thick Kapton is chosen as the substrate which is a plastic based flexible substrate with high mechanical and thermal durability. Kapton is a proper option for flexible electronic applications because of low dielectric loss ($\tan\delta$=0.02), appropriate relative permittivity (ϵ_r=3.5) and compatibility with printing technology. The greater coil is a 10-turn two-layer planar spiral inductor with a 6.4 mm radius while the smaller coil is an 8-turn two-layer spiral inductor with a 3.2 mm radius. These two coils are connected to each other
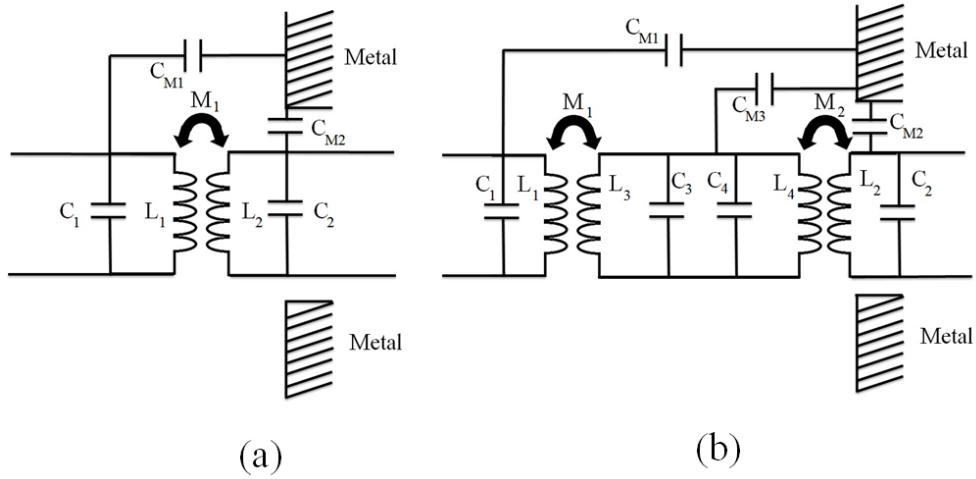
Figure 6.3: The equivalent circuits of the system operating in proximity of metal (a) without the booster and (b) with the booster.

in parallel using a 46.85 mm long twin-lead transmission line. The proposed structure and the fabricated sample by etching process are illustrated in Fig. 6.5 (a) and (b), respectively. The circuit is appropriate for application in which the user wants to read the tag with the corner of the smartphone. It is more convenient for the user since by approaching the corner of the smartphone (where the tip of booster located) to the tag, there is less uncertainty for the proper alignment between the tag and tip of the booster. The other realization is by making two coils concentric but the alignment is harder because the smaller coil that should be placed exactly on top of the tag is under the smartphone and hard to see.

6.2 The Simulation and Measurement Results

The performance of the proposed booster circuit is simulated by Ansys HFSS 15 which is a 3D full-wave electromagnetic simulator. In order to evaluate the operation of the booster, the real case scenario in which an NFC reader communicates with an HF RFID tag is simulated. As can be seen in Fig. 6.6 in which the whole system is simulated, the magnitude of magnetic
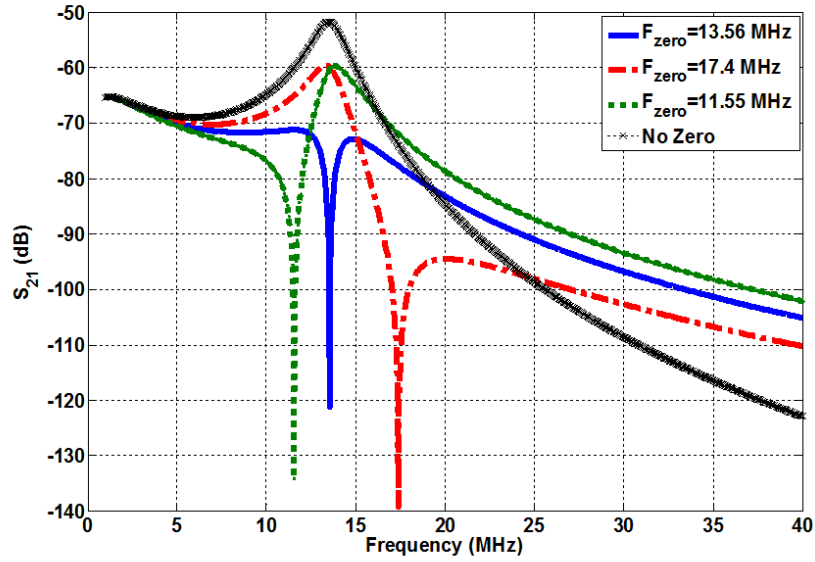
(a)
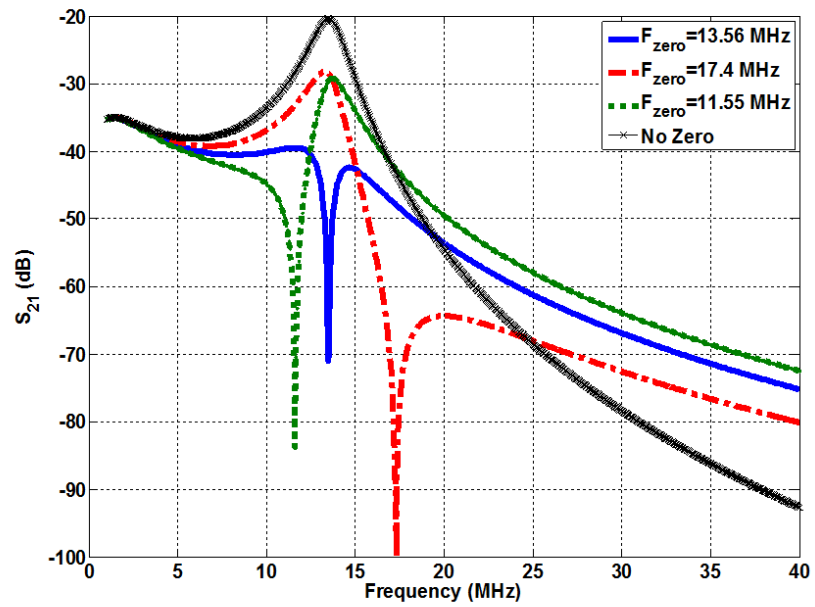
(b)

Figure 6.4: The analytical results for the transferred power considering the effect of metal asset for circuits (a) without the booster and (b) with the booster.
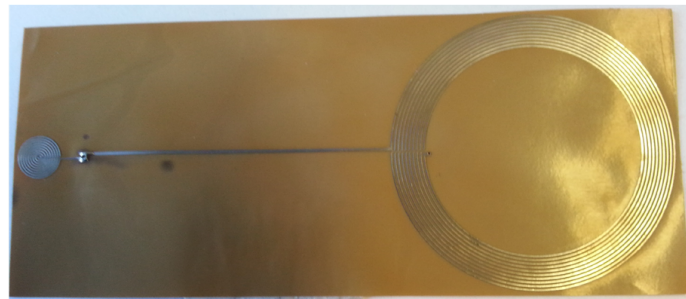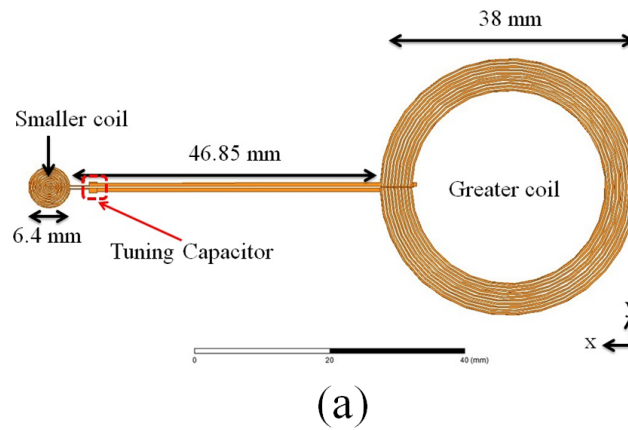
Figure 6.5: (a) Proposed geometry for the booster and (b) the fabricated sample.

field reproduced by the smaller coil is much higher than that of the field made by NFC reader. It is worth mentioning that this high magnitude magnetic field exists in a small region close to the smaller coil; thus, the induced current in the metal asset is minimized because this region is filled with RFID tag. It can be deduced that the circuit behaves the way the predicted properties do. In this simulation scenario, a 180 mm×140 mm×40 mm stainless steel box is placed at 2 mm distance from the booster while the HF RFID tag is implemented 0.2 mm from the surface of steel box inside the hole. The physical dimensions of the hole are 3.2 mm (radius) by 4 mm (height). The NFC antenna is placed in 5 mm distance from the booster with the outer radius of 34.5 mm. The first port is connected to the NFC reader and the second one to the RFID tag. Fig. 6.7 represents the simulation results of the transferred power

versus frequency from 5 MHz to 30 MHz for different distances between the booster and the metal asset. By increasing the distance, the effect of the eddy current reduces but because of the longer path, the transferred power decreases. As can be seen, the best performance in terms of the absolute boost level is achieved at 3 mm far from the metal around 13.56 MHz although any transferred power level above the -30 dB line can wake the IC up and communicate properly. The simulation results of the transferred power for different distances between the booster and the NFC antenna are illustrated in Fig. 6.8. The variation over this gap is between 4 mm and 6 mm which are close to the smartphone case thickness. The results show that small changes in the distance do not influence the transferred power drastically; this is really desirable due to the practical accuracy limitations for the end user.
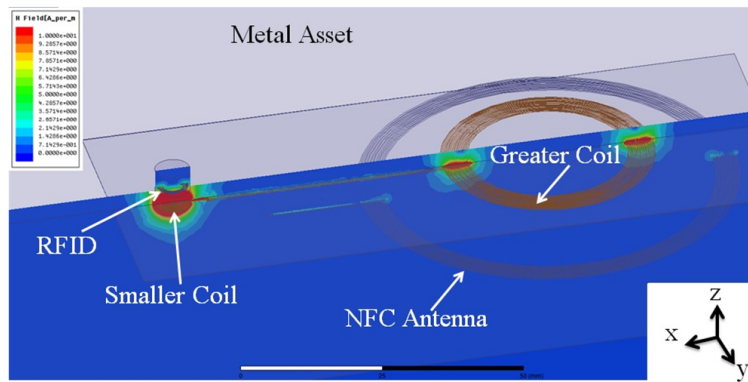
Figure 6.6: The simulation results for H-Field.

The fabricated booster circuit has been measured using a ZVL 13 vector network analyzer (VNA) after full two-port TOSM calibration between 5 MHz and 30 MHz. Instead of the NFC antenna, a coil with similar dimensions to the simulation case resonating at 13.56 MHz is fabricated with a proper matching circuit to 50 Ω and is connected to the first port of the VNA. Similarly, a small coil resonating at 13.56 MHz and matched to 50 Ω is also used instead of the RFID coil and connected to the second port of the VNA. The geometries of these coils are shown in Fig. 6.9 (a). Different methods such as using a magnetic probe, for directly measuring the strength of the magnetic field are presented in [80].
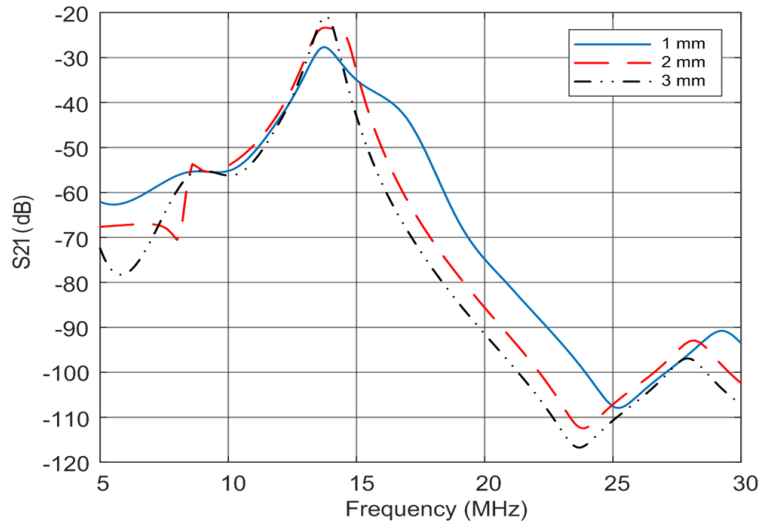
Figure 6.7: The simulation results of the transferred power ratio for different distances between the booster and metal asset.
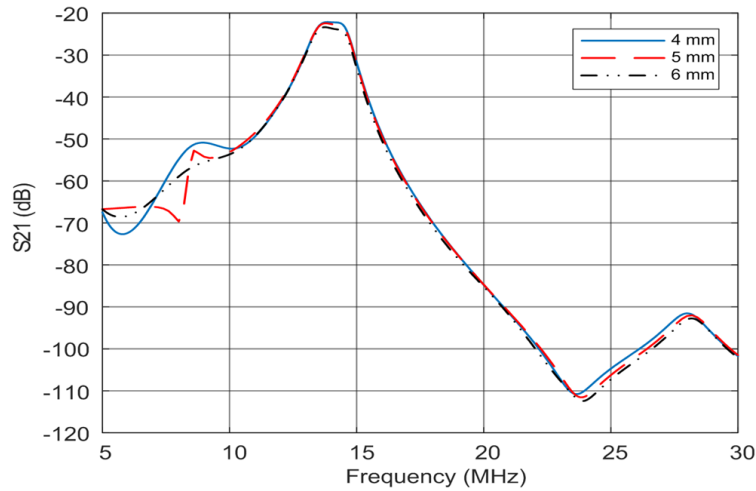
Figure 6.8: The simulation results of the transferred power ratio for different distances between the booster and NFC reader.

This measurement setup is crucial for the performance investigation of the booster because it is not feasible to connect any measurement device to the booster. It is due to the loading effect of the measurement equipment and altering the coupling phenomena. Similarly, The existence of NFC and RFID tag is essential for the proper performance of the booster.
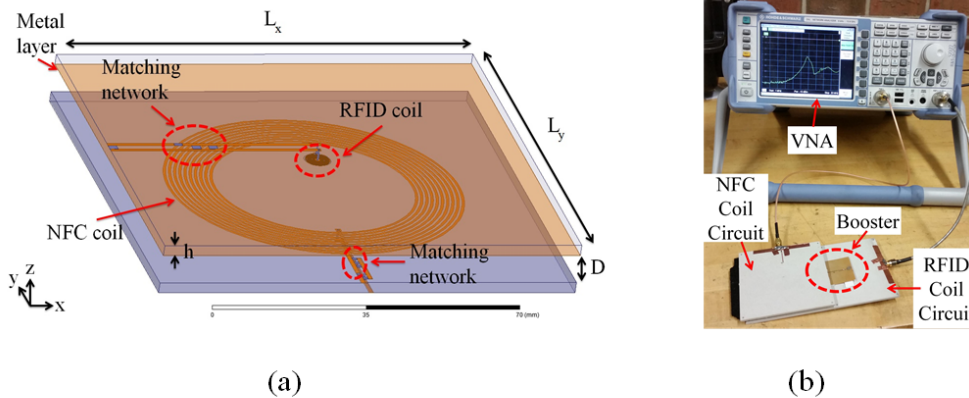
Figure 6.9: (a) The geometry of the measurement coils. (b) The measurement setup.

These coils are designed in a similar way as the booster, and their physical dimensions are summarized in Table 6.1.

These coils are fabricated on 2.54 mm thick RT/duroid 5880 LZ substrate with relative permittivity and loss tangent equal to 1.96 and 0.002, respectively. The matching circuits for these two measurement coils are LC low loss networks matched to 50 Ω at 13.56 MHz. The booster is placed between these two coils at the distances similar to the real scenario (2 mm and 5 mm of the RFID tag and NFC, respectively). The measurement setup used is illustrated in Fig. 6.9 (b). The measurement results of the transferred power for variations of the booster-RFID distance and booster-NFC distance can be seen in Fig. 6.10 (a) and (b), respectively. The curves show 30 dB boosts in the transferred power at 13.56 MHz after inserting the booster.

It should be mentioned, that the approximate amount of transmitted power by the NFC antenna in smartphones is 50 mW (17 dBm) and the wake-up power of the RFID IC is -14 dBm. A simple calculation proves that for waking up the RFID IC using the NFC antenna, there is a margin of -30 dB in the transferred power. Hence, by comparing the measurement results from the VNA, it can be interpreted that the booster should be appropriately functional for waking up the IC because the transferred power level is above the -30 dB line at

90
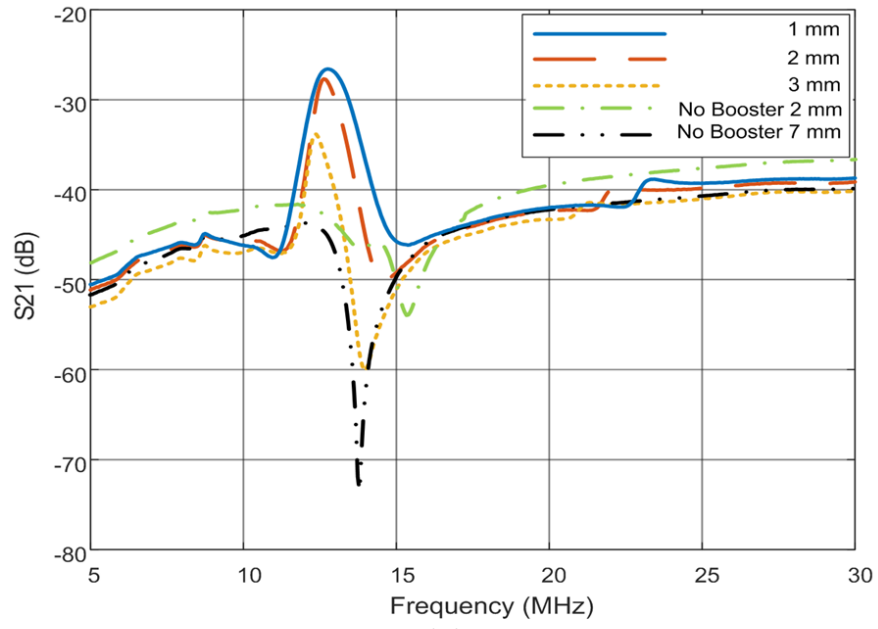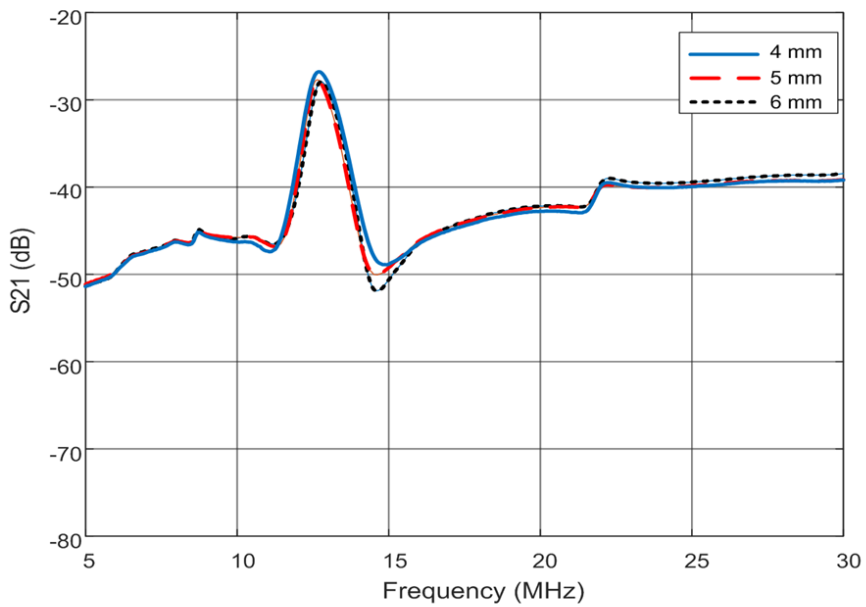
Figure 6.10: The measurement results for (a) different booster RFID gap and (b) booster-NFC gap.

(a)   (b)
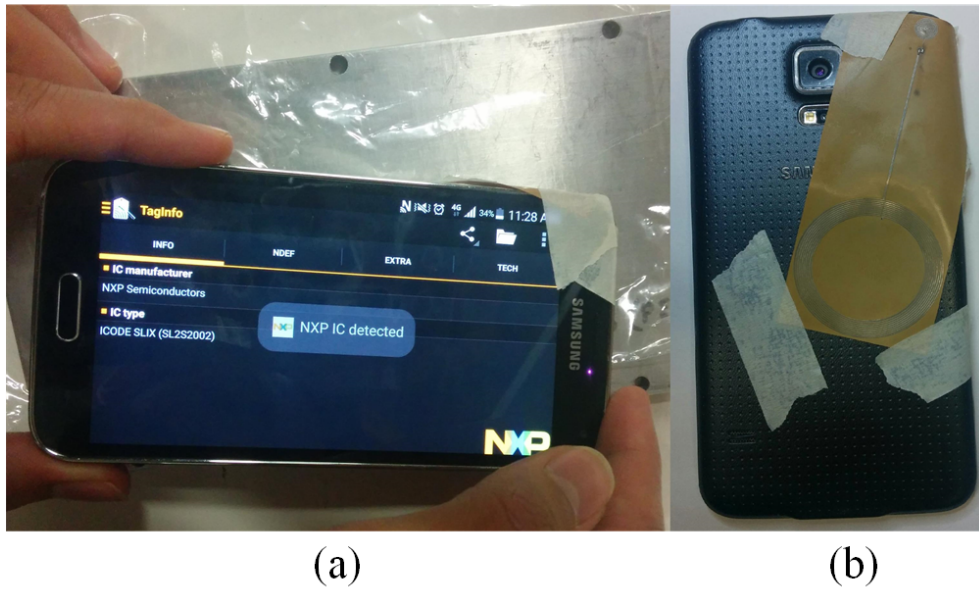
Figure 6.11: (a) The detected DuraPlog 6 implemented in an aluminum sheet by TagInfo app using a Samsung Galaxy S5. (b) The alignment and attachment of booster on a Samsung Galaxy S5.

the desired frequency. The proposed structure is also measured by attaching it to the back of a Samsung Galaxy S5 and S4. For reading HF RFIDs using the NFC of these smartphones, TagInfo app was used. The practical measurement using a real smartphone and HF RFID in a metal asset after inserting the booster was successful. Fig. 6.11 (a) shows that the DuraPlug 6 was implemented in an aluminum sheet read by TagInfo app. The alignment and installation of the booster on a Samsung Galaxy S5 are depicted in Fig. 6.11 (b).

6.3 Inkjet Printed Passive Booster

In this section, an inkjet printed flexible concentric version of the proposed booster is presented. The additive printing technologies provide us with the capability of fast, low cost and environmentally-friendly fabrication as well as the benefit of utilizing unconventional substrates [81]. Inkjet printing is one of the most common methods of droplet-based direct writing techniques. By inkjet printing technique, the pattern can be printed by generating a single drop of ink and placing it on the desired location which is also called drop-on-demand (DoD) [24]. It is tempting to utilize inkjet printing technology as the fabrication process due to the possibility of printing a variety of conductive and dielectric materials on various substrates. The compatibility of RFID fabrication utilizing inkjet printing technology has been investigated in the last decade [81].

The mechanism of magnetic boosting was discussed before. The fabrication and results of the printed booster are presented in this section. The concentric version of the passive booster is also proposed for the application in which the reader and tag can be aligned concentrically. This results in a generally smaller area for the whole circuit since the portion inside the larger coil is empty and can be utilized to place the smaller coil. The outer circumference of the larger coil is shaped like a square in order to increase the self-capacitance, hence shrinking the whole area of the coil. The proposed geometry of the concentric booster and the inkjet printed version are depicted in Fig. 6.12.

The simulation results of the magnetic field for the system before and after the presence of the booster and the 3D sketch of the system are illustrated in Fig. 3.66.

The proposed geometry in Fig. 6.12 (a) is fabricated by Fujifilm Dimatix 2800 inkjet material printer. For the fabrication of the conductive trace, JS-B40G silver nano-particle ink made by NovaCentrix, with 76 nm particle size and 30 wt% silver content, is utilized. The structure is fabricated by printing two layers of silver ink on each side separately and cured at 280° C for an hour. The measured conductivity of the 1 μm-thick silver ink by DC probe is 20 MS/m. The quality of the printed pattern depends on the properties of ink and

93
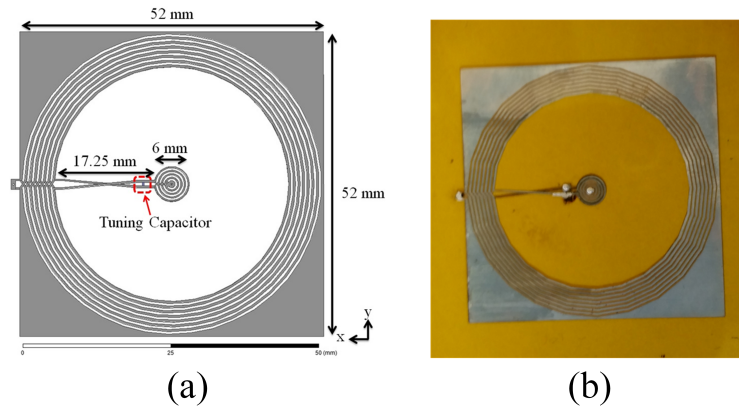
Figure 6.12: Concentric booster (a) proposed geometry, (b) inkjet printed version.
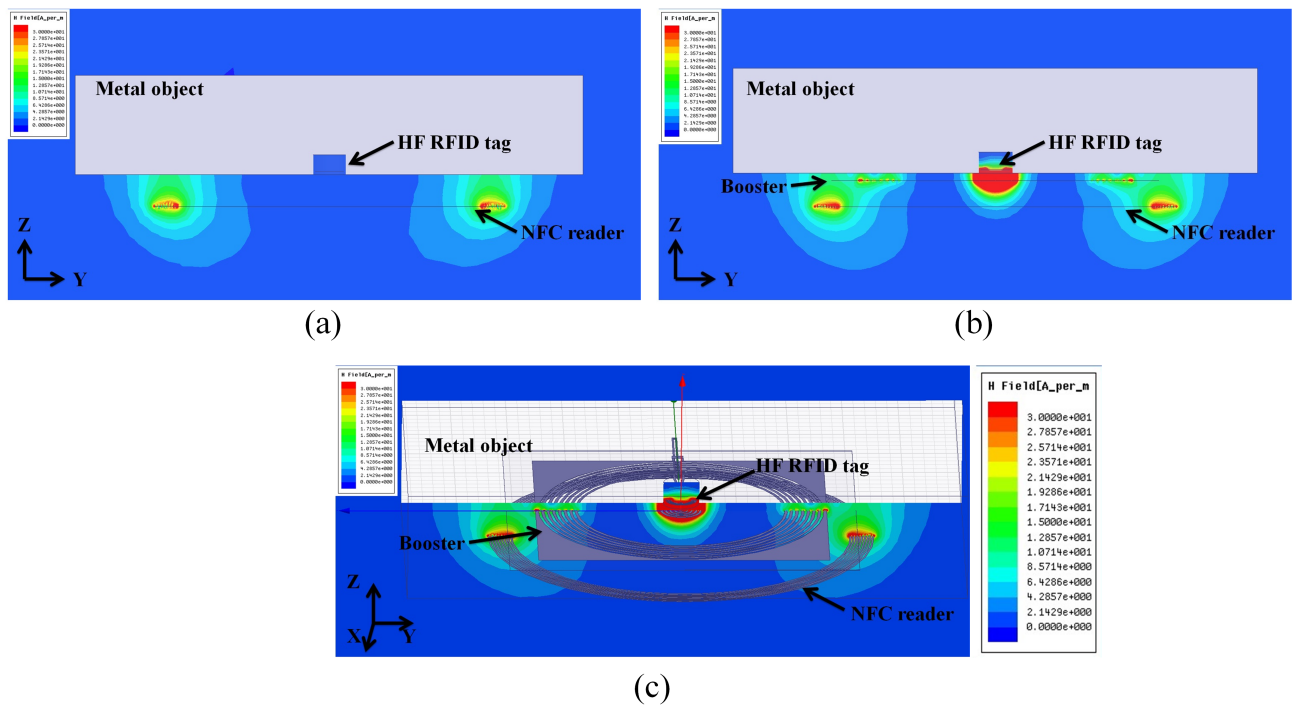
Figure 6.13: NFC system (a) before presence of booster, (b) after presence of booster and (c) the 3D sketch of the system.

substrate such as viscosity, contact angle, temperature, hydrophilicity, and roughness [24].

Dupont Kapton is a proper option for the substrate since it is a mechanically strong
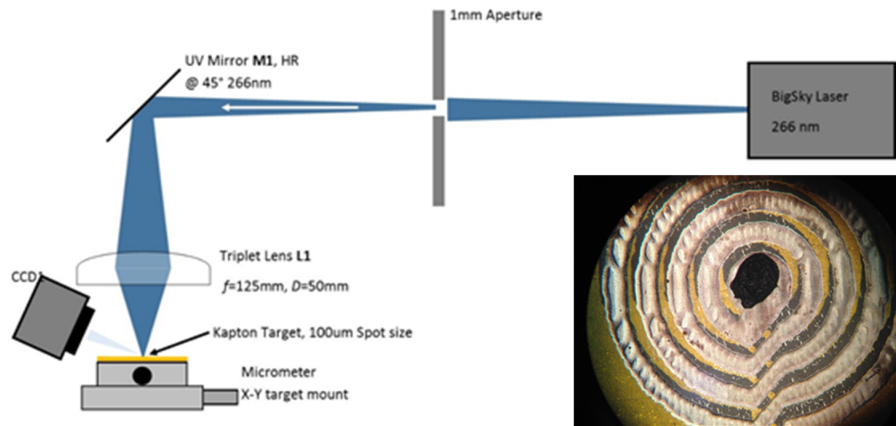
Figure 6.14: The laser beam architecture for implementation of via in circuit.

flexible substrate that can tolerate up to 300° C and is compatible with inkjet printing. In addition, its electrical properties, which are 3.5 and 0.002 for relative permittivity and loss tangent, respectively, are favorable. The required via in the inkjet printed version is fabricated by exposing the circuit to a laser beam. For this purpose the BigSky $Nd:YAG$ laser (1064 nm) was utilized in the proposed setup as depicted in Fig. 6.14. Using two sets of nonlinear KDP lenses, 266 nm wavelength is obtained and used for fabrication of vias. The fabricated hole is 200 μm in diameter at the top and 100 μm at bottom layers. Then, for electrical connection between the top and bottom layers, a small droplet of 1/3 silver conductive epoxy made by MG Chemicals and 2/3 Isopropanol is located on top of the hole. Because of the low viscosity of the mixture and capillarity phenomenon, the epoxy is driven into the hole and flows from the other side, resulting in an electrical connection between top and bottom layers. The top view of the fabricated hole into the circuit by the proposed the mechanism can be seen in Fig. 6.14.

The measurement setup is the same as the one used in Section 6.2 except that the coils are aligned concentrically. The measurement results for cases with and without the booster are presented in Fig. 6.15. It can be seen that the maximum transferred power is increased by more than 15 dB just by applying the booster into the system. The results are not as good
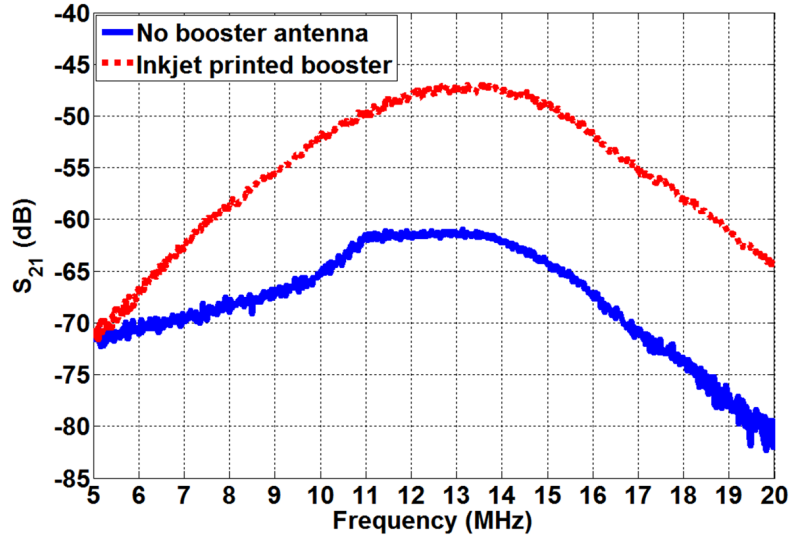
Figure 6.15: The measurement results of the system without and with the inkjet printed booster.

as the first version of the booster since it is printed using ink which has significantly lower conductivity and thickness compared to the PCB version. In addition, the conductivity and electrical connection in the vias are even worse. The total dimensions of the printed version are smaller than the PCB version; therefore, it can be expected that the results are not as good.

A simple passive low-cost circuit for improving the read range of an unknown-impedance NFC-based communication in the proximity of a metal asset is proposed in this Chapter. A full analytical model was driven for the coils in the presence of metal and the results were verified by full-wave simulation and measurements. Without this circuit, it is practically impossible to read small HF RFID tags implemented in a metal asset utilizing an NFC-enabled device such as a smartphone or tablet due to the different coil sizes and induced eddy current. This booster improves the transferred power 30 dB and provides sufficient power to wake the IC up. Then an inkjet-printing concentric version of the system is implemented and investigated. The magnetic coupling is increased by centralizing the radiated magnetic field of the NFC reader in a small region. Having only one discrete electronic component and being

fully inkjet-printed without using ferrite core made this circuit low-cost and appropriate for mass-production. The huge amount of the transferred power boosted by applying this circuit into the system supports the functionality of the idea.

Chapter 7

Conclusion and Future Work

7.1 Summary

In this thesis, two main obstacles in widespread commercial wireless RF sensor nodes have been addressed: the requirement for having a wireless communication system with RF passive sensing capability embedded into the architecture and improving the communication range for the application that the sensor node operates in an adverse or lossy medium. New methods for cost-effective, energy-effective, and practical RF/Microwave sensing are proposed. The sensing is done by placing different MUTS in contact with the antenna, resulting in changes in the frequency response and the input impedance of the antenna. Since the sensor antenna loads the LO of the transmitter, the carrier frequency changes for each sample depending on the relative permittivity of each one. Conventional RF/Microwave systems detect the frequency shift of the system by monitoring the frequency spectrum of the system and post-processing it which is a costly, power-consuming, impractical, complicated, and bulky technique. Using the proposed techniques, the frequency shift can be detected at the transmitter or receiver side without increasing the complexity or power consumption of the system. It is worth mentioning that the system is also capable of transmitting communication data.

In the first method, the frequency shift is recovered at the transmitter side by sampling a small portion of the output power and comparing it to a reference signal using a PFC. The output signal of PFC is the error between the sampled signal and the reference signal and is correlated to the permittivity of MUT. The data then can be further used for re-tuning the system back to the desired operating frequency as well as preparing it for modulation so at the receiver the information about the sample is also provided.

In the second method, the extraction of sensing data is done at the receiver side although the sensing is done at the transmitter. At the receiver, a non-coherent demodulator is used for the demodulation of the pilot data while a zero-crossing detector is utilized to obtain the frequency shift in the carrier due to the samples. In this technique, an OOK modulation is used for the modulation of the pilot to show that the system is capable of sensing as well as communication.

In both methods, a dipole antenna is used as the sensor-communication antenna but with different balun and sensing regions. In the first sensor antenna, a parasitically loaded open loop is used for sensing on which the samples are located and the loading of the antenna alters. Then a 180° power divider is used as a balun to provide the transition between the balance-unbalance signals. A -14 dB power coupler is also used for sampling the carrier frequency while the majority of the signal flows between antenna and LO. Using different permittivities changes the input impedance of the antenna, hence the operating frequency of LO changes since the antenna loads it. Since a parasitic element is used for sensing, the radiation properties of the antenna are not affected, and this is desirable for sensor antennas. The second version of the proposed sensor antenna operates based on directly changing the capacitance of the dipole antenna by placing the samples on the gap between the arms. The equivalent circuit of the dipole and the way samples affect the input impedance are investigated.

The performance of the system are investigated at 915 MHz UHF RFID band and 2.45 GHz GSM band to show the compatibility of the proposed method with conventional systems. It can be deduced from the results that by using an inexpensive, practical, low-cost,

and energy efficient method, the sensing capability is added to modulator/demodulator architecture ; this is desirable for wireless sensor network. It is also worth mentioning that the same antenna for communication is used for sensing while the radiation characteristics of the antenna are kept intact.

As an application at HF band, a passive magnetic power booster is proposed for improving the quality of the communication system for sensing at low frequencies around a metallic object as an example of adverse environment. It is a challenging task since most of the industrial tools and equipment are made of metallic and it is required to observe and monitor certain parameters at their surface. This passive booster is optimized to be used by NFC-enabled smartphones and tablets.

7.2 Future Work

The proposed ideas in this thesis can be implemented or used in the future in the following applications and/or systems:

7.2.1 RFID Sensor Node

This system has the potential to be implemented alongside other RFID subsystems inside an IC for better efficiency and performance. It can also utilize established RFID standards for communication and energy harvesting. Therefore, there is no need for battery or powering-up in the node, resulting in a sustainable, low-maintenance, and long-life span WSN.

7.2.2 Differential Configurations

A differential-balanced VCO sensor system should be designed and implemented for the adaptability and utilization of other modulation schemes such as Quadrature Amplitude Modulation (QAM). Moreover, having a differential balanced system results in better output voltage swing and power. Balanced RF/Microwave sensors can be directly connected to the

differential VCO without any Balun.

7.2.3 Sensor Antenna

It is also possible to use different types of sensor antennas in order to sense and measure other parameters. This system can also be implemented at HF band for biomedical remote sensing in which the proposed booster can provide the required read range for the under-skin implementation of an IC version of the system.

7.3 Contributions

The academic contributions listed here are the outcomes of my research throughout my Ph.D. studies at the University of Alberta including refereed journals, conference papers and patents.

Patent

(P1) "Apparatus and Methods for Radio Frequency Sensing," Hossein Saghlatoon, Rashid Mirzavand, Pedram Mousavi, PCT/CA2018/050688, filed June 8, 2018

Journals

(J1) "Fixed-Frequency Material Sensing Transmitter," Hossein Saghlatoon, Rashid Mirzavand, Pedram Mousavi, IEEE Transactions on Industrial Electronics, Major revision Feb 2019.

(J2) "Radially Inhomogeneous Dielectric Lens for Antenna Gain Enhancement Using 3D Printing," Hossein Saghlatoon, Rashid Mirzavand, Mohammad Mahdi Honari, Pedram Mousavi, IEEE Antennas and Wireless Propagation Letters, prepared to submit.

(J3) "Investigation of the 3D Printing Roughness Effect on the Performance of a Dielectric Rod Antenna", Mohammad Mahdi Honari, Rashid Mirzavand, Hossein Saghlatoon, Pedram Mousavi, IEEE Antennas and Wireless Propagation Letters, Vol.17, No.14, 2018.

(J4) "Sensor Antenna Transmitter System for Material Detection in Wireless-Sensor-Node Applications", Hossein Saghlatoon, Rashid Mirzavand, Mohammad Mahdi Honar, Pedram Mousavi, IEEE Sensors Journal, Vol.18, No.21, 2018.

(J5) "Investigation on Electrical and Mechanical Properties of 3D printed Nylon 6 for RF/Microwave Electronics Applications", Samira Aslanzadeh, Hossein Saghlatoon, Mohammad Mahdi Honari, Rashid Mirzavand, Pedram Mousavi, Elsevier Additive Manufacturing, 2018.

(*J*6) "A Highly Deformable Conducting Traces for Printed Antennas and Interconnects: Silver/Fluoropolymer Composite Amalgamated by Triethanolamine", Amit Kumar, Hossein Saghlatoon, Thanh-Giang La, Mohammad Mahdi Honari, Hemant Charaya, Haitham Abu Damis, Rashid Mirzavand, Pedram Mousavi, Hyun-Joong Chung, Flexible and Printed Electronics, September 2017.

(*J*7) "Two-Layered Substrate Integrated Waveguide Filter for UWB Applications", Mohammad Mahdi Honari, Rashid Mirzavand, Hossein Saghlatoon, Pedram Mousavi, IEEE Microwave and Wireless Components Letters, Vol 27, no 7, 2017.

(*J*8) "Self-Reinforcing Graphene Coatings on 3D Printed Elastomers for Flexible Radio Frequency Antennas and Strain Sensors", Xinda Li, Mohammad Mahdi Honari, Yiyang Fu, Amit Kumar, Hossein Saghlatoon, Pedram Mousavi, Hyun-Joong Chung, Flexible and Printed Electronics, July 2017.

(*J*9) "Investigation on Passive Booster for Improving Magnetic Coupling of Metal Mounted Proximity Range HF RFIDs", Hossein Saghlatoon, Rashid Mirzavand, Mohammad Mahdi Honari, Pedram Mousavi, IEEE Microwave and Wireless Components Letters, Vol 65, no 9, 2017.

(*J*10) "Low-Cost Inkjet Printed Passive Booster for Increasing the Magnetic Coupling in Proximity of Metal Object for NFC Systems", Hossein Saghlatoon, Rashid Mirzavand, Mohammad Mahdi Honari, Pedram Mousavi, IEEE Transactions on Microwave Theory and Techniques, Vol 26, no 12, 2017.

(*J*11) "A Dual-band Low Profile Aperture Antenna with Substrate Integrated Waveguide Grooves", Mohammad Mahdi Honari, Rashid Mirzavand, Hossein Saghlatoon, Pedram Mousavi, IEEE Transactions on Antennas and Propagation, 2016, Vol 64, no 04.

Conferences

(*C*1) "Sensor Antenna for Dielectric Constant Measurement of Materials in Contact with the Structure," Hossein Saghlatoon, Rashid Mirzavand, Mohammad Mahdi Honari, Pedram Mousavi, EuCap 2019, Krakow, Poland

(*C*2) "A Two-Port Microstrip Sensor Antenna for Permitivitty and Loss Tangent Measurements", Mohammad Mahdi Honari, Rashid Mirzavand, Hossein Saghlatoon, Pedram Mousavi, EuCap 2019, Krakow, Poland

(*C*3) "Investigation on the Effect of Roughness of 3D Printed Structure on Performance of Microwave Devices", Hossein Saghlatoon, Rashid Mirzavand, Mohammad Mahdi Honari, Pedram Mousavi, ANTEM 2018, Waterloo, Canada

(*C*4) "An RFID Sensor for Early Expiry Detection of Foods", Mohammad Mahdi Honari, Hossein Saghlatoon, Rashid Mirzavand, Pedram Mousavi, ANTEM 2018, Waterloo, Canada

(*C*5) "Substrate Integrated Waveguide Groove Sensor Antenna for Permittivity Measurements", Hossein Saghlatoon, Mohammad Mahdi Honari, Rashid Mirzavand, Pedram Mousavi, EuCap 2018, London, UK

(*C*6) "A Compact Substrate Integrated Waveguide CavityBacked Antenna with Stable Radiation Patterns forDual-Band Applications", Mohammad Mahdi Honari, Hossein Saghlatoon, Rashid Mirzavand, Pedram Mousavi, EuCap 2018, London, UK

(*C*7) "A lightweight and low-cost 3D printed waveguide for medium power applications', Rashid Mirzavand, Hossein Saghlatoon, Mohammad Mahdi Honari, Pedram Mousavi, ACES 2017, Suzhou, China

(*C*8) "A Novel Investigation on Printed Stretchable WLAN Antennas", Hossein Saghlatoon, Mohammad Mahdi Honari Kalateh, Rashid Mirzavand, Pedram Mousavi, Amit Kumar, Thang-Giang La, Hyun-Joong Chung, APS/URSI 2017, San Diego, USA, July 2017

(C9) "Low-Cost Miniaturized Open-Ended Slot-Based UHF RFID Tag for Harsh Environment", Hossein Saghlatoon, Mohammad Mahdi Honari Kalateh, Rashid Mirzavand, Pedram Mousavi, International Microwave Symposium (IMS 2016), May 2016, San Francisco, USA

(C10) "A Novel Booster Antenna on Flexible Substrates for Metal Proximity NFC Applications", Hossein Saghlatoon, Pedram Mousavi, APS/URSI 2015, Vancouver, Canada, July 2015

Bibliography

[1] K. Kaushik, D. Mishra, S. De, K. R. Chowdhury and W. Heinzelman, "Low-Cost Wake-Up Receiver for RF Energy Harvesting Wireless Sensor Networks," *IEEE Sensors J.*, vol. 16, no. 16, pp. 6270–6278, 2016.

[2] G. Mokhtari, Q. Zhang, C. Hargrave and J. C. Ralston, "Non-Wearable UWB Sensor for Human Identification in Smart Home," *IEEE Sensors J.*, vol. 17, no. 11, pp. 3332–3340, 2017.

[3] B. C. Csaji, Z. Kemeny, G. Pedone, A. Kuti and J. Vancza, "Wireless Multi-Sensor Networks for Smart Cities: A Prototype System With Statistical Data Analysis," *IEEE Sensors J.*, vol. 17, no. 23, pp. 7667–7676, 2017.

[4] M. Li and H-J. Lin, "Design and implementation of smart home control systems based on wireless sensor networks and power line communications," *IEEE Trans. Ind. Electron.*, vol. 62, no. 7, pp. 4430–4442, 2015.

[5] S. Kurt, H.U. Yildiz, M. Yigit, B. Melike and V. C. Gungor, "Packet size optimization in wireless sensor networks for smart grid applications," *IEEE Trans. Ind. Electron.*, vol. 64, no. 3, pp. 2392–2401, 2017.

[6] M. Balato, L. Costanzo and M. Vitelli, "MPPT in Wireless Sensor Nodes Supply Systems Based on Electromagnetic Vibration Harvesters for Freight Wagons Applications," *IEEE Trans. Ind. Electron.*, vol. 64, no. 5, pp. 3576–3586, 2017.

[7] P. Cheong, K-F. Chang, Y-H. Lai, S-K. Ho, I-K. Sou and K-W. Tam, "A ZigBee-based wireless sensor network node for ultraviolet detection of flame," *IEEE Trans. Ind. Electron.*, vol. 58, no. 11, pp. 5271–5277, 2011.

[8] https://www.evelta.com/iot-sensors

[9] http://seminarprojecttopics.blogspot.ca/2012/11/low-power-wirelesssensor-networks.html

[10] A. Rida, L. Yang, R. Vyas and M. M. Tentzeris, "Conductive inkjet printed antennas on flexible low-cost paper-based substrates for RFID and WSN applications," *IEEE Antennas Propag. Magazine*, vol. 51, no. 3, 2009.

[11] J. Wang, "The dielectric properties of soil-water mixtures at microwave frequencies," *Radio. Sci.*, vol. 15, no. 5, pp. 977–985, 1980.

[12] C. A. Umenyiroa, R. Druce, R. D. Curry, P. Norgard, T. McKee, J.J. Bowders and D.A. Bryan, "Dielectric constant of sand using tdr and fdr measurements and prediction models," *IEEE Trans. Plasma. Sci*, vol. 40, no. 10, pp. 2408–2415, 2012.

[13] A. A. Skordos P. I. Karkanas and I. K. Patridge, "A dielectric sensor for measuring flow in resin transfer moulding," *Meas. Sci. Technol.*, vol. 11, no. 1, pp. 1–25, 2000.

[14] C-T. Chiang and Y-C. Huang, "A semicylindrical capacitive sensor with interface circuit used for flow rate measurement," *IEEE Sensors J.*, vol. 6, no. 6, pp. 1564–1570, 2006.

[15] B. Jackson and T. Jayanthy, "A novel method for water impurity concentration using microstrip resonator sensor,' in' *Recent Advances in Space Technology Services and Climate Change*, Nov 2010

[16] G. Akerlof, "Dielectric constants of some organic solvent-water mixtures at various temperatures," *Journal. American Chem. Soc.*, vol. 54, no. 11, pp. 4125–4139, 1932.

[17] A. Vena, L. Sydanheimo, M. M. Tentzeris and L. Ukkonen, "A Fully Inkjet-Printed Wireless and Chipless Sensor for CO2 and Temperature Detection," *IEEE Sensors J.*, vol. 15, no. 1, pp. 89–99, 2015.

[18] R. Mirzavand, M. M. Honari and P. Mousavi, "Direct-Conversion Sensor for Wireless Sensing Networks," *IEEE Trans. Ind. Electron.*, vol. 64, no. 12, pp. 9675–9682, 2017.

[19] Z. Jiang, M. Li and X-C. Zhang, "Dielectric constant measurement of thin films by differential time-domain spectroscopy," *Applied Phys. Lett.*, vol. 76, no. 22, pp. 3221–3223, 2000.

[20] J. Krupka, "Frequency domain complex permittivity measurements at microwave frequencies," *Meas. Sci. Technol.*, vol. 17, no. 6, pp. 55–70, 2006.

[21] B. M. Oliver, "Time domain reflectometry," *J. Hewlett-Packard*, vol. 15, no. 6, pp. 1–7, 1964.

[22] Y. Feldman, I. Ermolina and Y. Hayashi, "Time domain dielectric spectroscopy study of biological systems," *IEEE Trans. Dielectr. Electr. Insul.*, vol. 10, No. 5, pp. 728–753, 2003.

[23] W. S. Zaengl, "Dielectric spectroscopy in time and frequency domain for HV power equipment. I. Theoretical considerations," *IEEE Electr. Insul. Mag.*, vol. 9, No. 5, pp. 5–19, 2003.

[24] H. Saghlatoon, L. Sydänheimo, L. Ukkonen and M. M. Tentzeris, "Optimization of inkjet printing of patch antennas on low-cost fibrous substrates," *IEEE Antennas Wireless Propag. Lett.*, vol. 13, pp. 915–918, 2014.

[25] A. Ebrahimi, W. Withayachumnankul, S. Al-Sarawi, D. Abbott, "High-sensitivity metamaterial-inspired sensor for microfluidic dielectric characterization," *IEEE Sensors J.*, vol. 14, No. 5, pp. 1345–1351, 2014.

[26] O. Huber, T. Faseth, G. Magerl and H. Arthaber, "Dielectric Characterization of RF-Printed Circuit Board Materials by Microstrip Transmission Lines and Conductor-Backed Coplanar Waveguides Up to 110 GHz," *IEEE Trans. Microw. Theory Tech.*, vol. 66, No. 1, pp. 237–244, 2018.

[27] P. M. Narayanan, "Dielectric Microstrip transmission line method for broadband permittivity measurement of dielectric substrates," *IEEE Trans. Microw. Theory Tech.*, vol. 62, No. 11, pp. 2784–2790, 2014.

[28] D. C. Thompson, O. Tantot, H. Jallageas, G. E. Ponchak, M. M. Tentzeris and J. Papapolymerou, "Characterization of liquid crystal polymer (LCP) material and transmission lines on LCP substrates from 30 60 57 to 110 GHz," *IEEE Trans. Microw. Theory Tech.*, vol. 52, No. 4, pp. 1343–1352, 2004.

[29] S. Panda, N. K. Tiwari, and M. J. Akhtar, "Computationally Intelligent Sensor System for Microwave Characterization of Dielectric Sheets," *IEEE Sensors Journal,* vol. 16, no. 20, pp. 7483-7493, Oct.15, 2016.

[30] I. Piekarz, J. Sorocki, K. Wincza, and S. Gruszczynski, "Microwave Sensors for Dielectric Sample Measurement Based on Coupled-Line Section," *IEEE Trans. Microw. Theory Techn.,* vol. 65, no. 5, pp. 1615-1631, May 2017.

[31] R. Mirzavand, M. M. Honari and P. Mousavi, "High-Resolution Balanced Microwave Material Sensor With Extended Dielectric Range," *IEEE Trans. Industrial Electronics,* vol. 64, no. 2, pp. 1552-1560, Feb. 2017.

[32] R. Mirzavand, M. M. Honari and P. Mousavi, "High-Resolution Dielectric Sensor Based on Injection-Locked Oscillators," *IEEE Sensors Journal,* vol. 18, no. 1, pp. 141-148, Jan. 2018.

[33] N. K. Tiwari, S. P. Singh and M. J. Akhtar, "Novel Microstrip-Based Simplified Approach for Fast Determination of Substrate Permittivity," *IEEE Transactions on Components, Packaging and Manufacturing Technology,* vol. PP, no. 99, pp. 1-10.

[34] W. Su and M. M. Tentzeris, "Smart Test Strips: Next-Generation Inkjet-Printed Wireless Comprehensive Liquid Sensing Platforms," *IEEE Trans. Ind. Electron.*, vol. 64, no. 9, pp. 7359–7367, 2017.

[35] X. Li, M. M. Honari, Y. Fu, A. Kumar, H. Saghlatoon, P. Mousavi and H-J. Chung, "Self-reinforcing graphene coatings on 3D printed elastomers for flexible radio frequency antennas and strain sensors," *Flexible and Printed Electronics*, vol. 2, No. 3, pp. 035001, 2017.

[36] A. Zhao, J. Zhang and G. Y. Tian, "Miniaturization of UHF RFID tag antenna sensors for corrosion characterizations, " *IEEE Sensors J.*, vol. 17, No. 23, pp. 7908–7916, 2017.

[37] A. Alomainy, Y. Hao and F. Pasveer, "Numerical and experimental evaluation of a compact sensor antenna for healthcare devices, " *IEEE Trans. Biomed. Circuits Syst.*, vol. 1, No. 4, pp. 242–249, 2007.

[38] W-J. Liao, T-W. Lien, B-R. Hsiao, H-S. Wang, C-F. Yang, J-H. Tarng, C-C. Nien and T-C. Chiu, "Sensor integrated antenna design for applications in cold chain logistic services, " *IEEE Trans. Antennas Propag.*, vol. 63, No. 2, pp. 727–735, 2015.

[39] Y. Seo, M. U. Memon and S. Lim, "Microfluidic Eighth-Mode Substrate-Integrated-Waveguide Antenna for Compact Ethanol Chemical Sensor Application, " *IEEE Trans. Antennas Propag.*, vol. 64, No. 7, pp. 3218–3222, 2016.

[40] C. Cho, X. Yi, D. Li, Y. Wang and M. M. Tentzeris, "Passive wireless frequency doubling antenna sensor for strain and crack sensing, " *IEEE Sensors J.*, vol. 16, No. 14, pp. 5725–5733, 2016.

[41] A. Vena, E. Perret, and S. Tedjini, "Chipless RFID tag using hybrid coding technique, " *IEEE Trans. Microw. Theory Tech.*, vol. 59, No. 12, pp. 3356–3364, 2011.

[42] M. Adhikary, A. Biswas, and M. J. Akhtar, "Active Integrated Antenna Based Permittivity Sensing Tag," *IEEE Sensors Letters,* vol. 1, no. 6, pp. 1-4, Dec. 2017.

[43] D. K. Cheng , "Field and wave electromagnetics," *Pearson Education India*, 2nd Edition, 1989.

[44] G. A. Rinard, R. W. Quine, S. S. Eaton, and G. R. Eaton, "Microwave coupling structures for spectroscopy," *Journals Mag. Res.*, Vol. 105, No. 2, pp. 137–144, 1993.

[45] D. Isakov, C. J. Stevens, F. Castles, and P. S. Grant, "A split ring resonator dielectric probe for near-field dielectric imaging," *Scientific Reports*, Vol. 7, No. 1, pp. 2038–2046, 2017.

[46] C. L. Yang, C. S. Lee, K. W. Chen, and K. Z. Chen, "Noncontact measurement of complex permittivity and thickness by using planar resonators," *IEEE Trans. Microw. Theory Techn.,*, Vol. 64, No. 1, pp. 247–257, 2016.

[47] R. N. Simons, "Coplanar waveguide circuits, components, and systems, " *John Wiley and Sons Inc.*, 2001.

[48] D. M. Pozar, "Microwave Engineering, " *John Wiley and Sons Inc.*, Ed. 3, 2005.

[49] A. Grebennikov, "RF and microwave transistor oscillator design, " *John Wiley and Sons Inc.*, Ed. 1, 2007.

[50] J. Obregon, and A. P. S. Khanna, "Exact derivation of the nonlinear negative-resistance oscillator pulling figure, " *IEEE Trans. Microw. Theory Techn.*, Vol. 30, No. 7, pp. 1109–1111, 1982.

[51] G. S. Hobson,, "Measurement of external Q factor of microwave oscillators using frequency pulling or frequency locking, " *IEEE Electron. Lett.*, Vol. 9, No. 10, pp. 191–193, 1973.

[52] Y. Cheng and Y. Shu, "A new analytical calculation of the mutual inductance of the coaxial spiral rectangular coils," *IEEE Trans. Magn.*, vol. 50, No. 4, pp. 1–6, 2014.

[53] A. Russell, "The magnetic field and inductance coefficients of circular, cylindrical, and helical currents," *Proc. of the Physical Society of London*, vol. 20, No. 1, pp. 476–506, 1906.

[54] R. M. Duarte, G. K. Felic, "Analysis of the coupling coefficient in inductive energy transfer systems," *Hindawi Active and passive Electronic components*, 2014.

[55] M. Q. Nguyen, Z. Hughes, P. Woods, Y.-S. Seo, S. Rao, and J.-C. Chiao, "Field distribution models of spiral coil for misalignment analysis in wireless power transfer systems," *IEEE Trans. Microw. Theory Tech.*, vol. 62, No. 4, pp. 920–930, 2014.

[56] M. Hamid and R. Hamid, "Equivalent circuit of dipole antenna of arbitrary length, " *IEEE Trans. Antennas Propag.*, vol. 45, No. 11, pp. 1695–1696, 1997.

[57] https://www.rogerscorp.com/index.aspx

[58] H. Saghlatoon, R. Mirzavand, M. M. Honari, and P. Mousavi, "Sensor Antenna Transmitter System for Material Detection in Wireless-Sensor-Node Applications," *IEEE Sensors Journal,* vol. 18, no. 21, pp. 8812–8819, 2018.

[59] P. M. Narayanan, "Microstrip transmission line method for broadband permittivity measurement of dielectric substrates," *IEEE Trans. Microw. Theory Techn.,* vol. 62, no. 11, pp. 2784–2790, Nov. 2014.

[60] H. Lobato-Morales and C. C. Humberto, "Wireless sensing of complex dielectric permittivity of liquids based on the RFID," *IEEE Trans. Microw. Theory Techn.,* vol. 62, no. 9, pp. 2160–2167, Sep. 2014.

[61] H. w. Ott, "Electromagnetic compatibility engineering, " *John Wiley & Sons*, 2011.

[62] M. D. A. Mohamed, and S. Hranilovic, "Information rates of optical impulse modulation over indoor diffuse wireless channels, " *IEEE 24th Biennial Symp. Commun.*, pp. 196–199, 2008.

[63] K. F. Warnick, R. B. Gottula, S. Shrestha and J. Smith, "Optimizing power transfer efficiency and bandwidth for near field communication systems," *IEEE Trans. Antennas Propag.*, vol. 61, No. 2, pp. 927–933, 2013.

[64] H. A. Al-Ofeishat, Mohammad A. A. Al Rababah, "Near field communication (NFC)," *International Journal of Computer Science and Network Security (IJCSNS)*, vol. 12, No. 2, pp. 93–99, 2012.

[65] A. Henning, "RF energy transmission for sensor transponders deeply implanted in human bodies," *IEEE 38th European Microwave Conference, 2008*, pp. 424–427, 2018.

[66] J. Heidrich, D. Brenk, J. Essel, M. Heinrich, G. Hofer, G. Holweg, S. Schwarzer, J. Meyer, R. Herschmann, B. Geck, and R. Weigel, "Multifunctional reference cells for multistandard RFID transponders," *IEEE Trans. Microw. Theory Tech.*, vol. 59, No. 3, pp. 772–790, 2011.

[67] A. Sharma, I. J. Garcia Zuazola, A. Gupta, A. Perallos, and J. C. Batchelor,"Non-uniformly distributed-turns coil antenna for enhanced H-field in HF-RFID," *IEEE Trans. Antenna Propag.*, vol. 61, No. 10, pp. 4900–4907, 2013.

[68] A. Shameli, A. Safarian, A. Rofougaran, M. Rofougaran, J. Castaneda and F. De Flaviis,"A UHF near-field RFID system with fully integrated transponder," *IEEE Trans. Microw. Theory Tech.*, vol. 56, No. 5, pp. 1267–1277, 2008.

[69] H. Knospe, H. Pohl, "A UHF near-field RFID system with fully integrated transponder,"*Elsevier Information security technical report*, vol. 9, No. 4, pp. 39–50, 2004.

[70] K. Xiao, L. Luo,"A novel mobile device NFC stack architecture,"*IEEE 11th Int. Conf. on Dependable, Autonomic and Secure Computing (DASC)*, pp. 169–173, 2013.

[71] H. Saghlatoon, P. Mousavi, "A novel booster antenna on flexible substrates for metal proximity NFC applications, "RFID security,"*IEEE Antennas and Propagation Society Int. Symp. (APSURSI)*, pp. 1768–1769, 2015.

[72] C. A. Balanis,"Antenna theory: analysis and design,"*John Wiley & Sons*, Vol. 1, 2005.

[73] H. Greenhouse, "Design of planar rectangular microelectronic inductor,"*IEEE Trans. parts hybrids packag.*, vol. 10, No. 2, pp. 101–109, 1974.

[74] G. Monti, P. Arcuti and L. Tarricone, "Resonant inductive link for remote powering of pacemakers,"*IEEE Trans. Microw. Theory Tech.*, vol. 63, No. 11, pp. 3814–3822, 2015.

[75] R. Lodato, V. Lopresti, R. Pinto, and G. Marrocco, "Numerical and experimental characterization of through-the-body UHF-RFID links for passive tags implanted into human limbs,"*IEEE Trans. Antenna Propag.*, vol. 62, No. 10, pp. 5298–5306, 2014.

[76] W. Pachler, W. Bosch, G. Holweg, G. Hofer, "A novel booster antenna design coupled to a one square millimeter coil-on-chip RFID tag enabling new medical applications,"*IEEE 38th European Microwave Conf.*, pp. 1003–1006, 2013.

[77] A. Vena, E. Perret, S. Tedjini, G. Eymin-Petot-Tourtollet, A. Delattre, F. Garet, and Y. Boutant, "Design of chipless RFID tags printed on paper by flexography,"*IEEE Trans. Antenna Propag.*, vol. 61, No. 12, pp. 5868–5877, 2013.

[78] Y. Lee, "Antenna circuit design,"*Application manual of Microchips Technology*, 1999.

[79] S. M. Yim and T. Chen, "The effects of a ground shield on the characteristics and performance of spiral inductors," *IEEE Journal Solid-State Circuits*, vol. 37, No. 2, pp. 237–244, 2002.

[80] P. Jankowski-Mihulowicz, W. Kalita, M. Skoczylas, M. Weglarski, "Modelling and design of HF RFID passive transponders with additional energy harvester," *Hindawi International Journal of Antennas and Propagation*, 2013.

[81] L. Yang, A. Rida, R. Vyas and M. M. Tentzeris, "RFID Tag and RF structures on paper substrates using inkjet-printing technology," *IEEE Trans. Microwave Theory Tech.*, vol. 55, no. 12, pp. 2894–2901, 2007.